MICROSTRUCTURAL MECHANICS OF DUCTILE FRACTURE

A Dissertation

by

YU LIU

Submitted to the Office of Graduate and Professional Studies of
Texas A&M University
in partial fulfillment of the requirements for the degree of

DOCTOR OF PHILOSOPHY

Chair of Committee,	Ankit Srivastava
Co-Chair of Committee,	Alan Needleman
Committee Members,	Matt Pharr
	Justin Wilkerson
Head of Department,	Ibrahim Karaman

August 2020

Major Subject: Materials Science and Engineering

ABSTRACT

Ductile fracture involving nucleation, growth and coalescence of microscale voids limits the manufacturability and mechanical performance of a variety of structural materials. This phenomenon is affected by length-scales arising from the material microstructure, the geometry of deformation and the loading condition. These length-scales in turn interact and evolve during the deformation process, resulting in often unknown and counterintuitive subsequent fracture processes. The aim of this dissertation is to understand how the nucleation and growth of macroscopic cracks in ductile materials depend on these evolving length-scales. Such an understanding enables microstructure informed prediction of ductile fracture and design of fracture resistant material microstructures. The microstructure of a variety of structural metals and alloys can be idealized as ductile matrix with randomly distributed inclusions. The size, spacing and volume fraction of these inclusions introduce microstructure-based length-scales. To investigate the micromechanism(s) of inclusion driven ductile fracture and its implications on fracture toughness of the material, a series of microstructure-based finite element calculations are carried out. Several features of crack growth behavior and dependence of fracture toughness on microstructural and material parameters observed in experiments, naturally emerge in these calculations. The results of these calculations also provide guidelines for microstructural engineering to increase fracture toughness. For example, the results show that for a material with small inclusions, increasing the mean inclusion spacing has a greater effect on fracture toughness than for a material with large inclusions. The pressing need of our time to decrease anthropogenic emissions of greenhouse gasses requires the use of high strength, fracture resistant structural materials such as advanced dual-phase steels to reduce vehicle weight and emissions. However, as the strength of dual-phase steels increases, the steel becomes more prone to ductile fracture under bending dominated manufacturing processes. Thus, the effect of length-scales induced by bending, intended dual-phase (ferrite and martensite) microstructure, and size and location of unintended inclusions on the bendability of dual-phase steels are quantified through microstructure-based finite element calculations. Here as well, several features of

ductile fracture of dual-phase steels under bending observed in experiments, naturally emerge in these calculations. The results of these calculations show that efforts to improve the bendability of advanced dual-phase steels must focus on improving the properties of the softer ferrite phase. Furthermore, supervised machine learning is utilized to understand the effects of uncertainty associated with both, the intended and the unintended microstructural features, on the bendability of the dual-phase steels. Another set of calculations aim at investigating the potential of low-density micro-architectured metallic materials to outperform the high fracture toughness of natural materials with density less than water. The results show that it is possible to design micro-architectured metallic materials that possess an exceptional combination of high strength and fracture toughness at low densities that no other existing lightweight materials can offer.

DEDICATION

To my parents and my family.

ACKNOWLEDGMENTS

The journey towards my Ph.D. would not have completed without the help and wisdom of many people. First, I want to express my deep gratitude to my advisor, Dr. Ankit Srivastava, who took me as his first Ph.D. student. This dissertation would not have been possible without his encouragement, inspiration, and guidance. I also want to thank Dr. Alan Needleman for his encouragement. I still remember the first phone call between Dr. Needleman, Dr. Srivastava and myself discussing a possible research project. In addition, I would like to thank Dr. Matt Pharr and Dr. Justin Wilkerson for serving on my Ph.D. committee and for providing valuable feedback.

I would like to acknowledge Dr. Dongwei Fan, Dr. Shrikant Bhat, Dr. Pallava Kaushik, Dr. Gang Huang and Dr. Narayan Pottore of ArcelorMittal Global R&D for all the support and for providing enlightening insights into metallurgical and technical issues related to steels. A special thanks to Dr. Fan for the many fruitful discussions. Dr. Fan's kindness and encouragements made this journey quite memorable.

I would also like to thank Dr. Vikram Deshpande, Dr. Norman Fleck and Dr. Luc St-Pierre of University of Cambridge, UK, and Dr. Shmuel Osovski of Technion-Israel Institute of Technology, Israel, for their invaluable help and support while carrying out some part of the work reported in this dissertation.

Furthermore, I would like to acknowledge all the faculty and staff members in the Department of Materials Science and Engineering. I would specifically like to thank Dr. Raymundo Arróyave for the amazing and inspiring lectures in his materials design studio class.

I feel very lucky to work in such an energetic research group with wonderful colleagues: Xinzhu Zheng, Lara Draelos, Abhilash Molkeri, Hemant Rathod, Edwin Chiu, Zhiqiang Zhan, Laura Moody, Zahra Ghasemi and Umair Bin Asim. In particular, Xinzhu, thank you for spending the entire journey with me.

I am grateful to all my friends for supporting me during my Ph.D. A sincere thanks to Tianyang for making authentic Chinese food for me whenever I was homesick and I would also like to thank

Yefan for encouraging me during the frustrating moments. I am not able to list all the names, but you know who you are.

Most importantly, Yuhao, thank you for being my driver, home chef and taking care of everything in my life. Finally, none of this would have been possible without the support from my parents, Yongxiang Liu and Ying Shen. Thank you, mom and dad!

CONTRIBUTORS AND FUNDING SOURCES

Contributors

This work was supported by a dissertation committee consisting of Dr. Ankit Srivastava and Dr. Alan Needleman of the Department of Materials Science and Engineering, Dr. Matt Pharr and Dr. Justin Wilkerson of the Department of Mechanical Engineering.

The experimental results presented in Chapter 5 was provided by Dr. Dongwei Fan of Arcelor-Mittal Global R&D, East Chicago, IN, USA, and those presented in Chapter 6 was provided by Dr. Luc St-Pierre, Dr. Norman Fleck, and Dr. Vikram Deshpande of University of Cambridge, Cambridge, UK.

All other work conducted for the dissertation was completed by the student independently.

Funding Sources

Graduate study was supported by ArcelorMittal Global R&D, East Chicago, IN, USA, and U.S. National Science Foundation grant CMMI - 1663130.

TABLE OF CONTENTS

Page

LIST OF FIGURES

FIGURE Page

LIST OF TABLES

TABLE Page

1. INTRODUCTION

Ductile fracture of metallic materials limits the performance, safety, reliability and manufacturability of various engineering products, components and structures. An engineering product, for example, a car, exhibits different structure at different length-scales; and the advanced materials used in structural elements of a car also exhibit structure on more than one length-scale, Fig. 1.1. The interlacing of structures at various length-scales results in stress/strain gradients that greatly affect the process of ductile fracture. Also, these structures at various length-scales tend to evolve with progressive deformation. For example, the deformation fields induced by structural geometry or boundary conditions can produce substantial microstructural modifications resulting in often unknown and counterintuitive subsequent fracture processes, Fig. 1.2. Modeling fracture and designing fracture resistant material microstructures thus requires bridging the field of mechanics of materials and materials science to understand how the nucleation and growth of macroscopic cracks depend on the interlacing of structures and their evolution at various length-scales. The ability to model nucleation and growth of macroscopic cracks will also provide the basis for assessing the reliability of components as well as the product quality in a variety of manufacturing processes.

Structural materials are one of the most technologically important materials, enabling technological breakthroughs in a variety of fields, such as energy, transportation, and infrastructure. There is also a growing demand to design and discover more fracture resistant, high strength, structural materials. This is driven by the technological need of lightweight structures for weight-critical products, such as aircrafts and long-haul trucks, and to decrease emissions from automobiles [15–18]. Structural materials with high density-normalized strength – e.g. Al-Li alloys, β-Ti alloys, Mg alloys, and Advanced High Strength Steels – are some of the most attractive candidate materials for lightweight structures [19–26]. However, all of these materials suffer from poor room temperature fracture resistance, which limits the performance, reliability and manufacturability of their components [27–31]. The past few decades have seen rapid advances in material

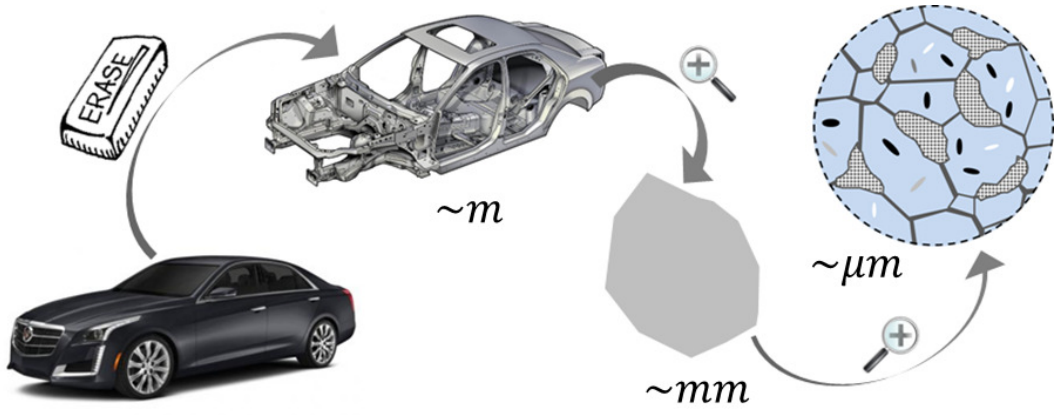

Figure 1.1: Schematic showing a car, body in white (at a length-scale of meters), generic complex heterogeneous metallic material used in the structural components (at a length-scale of millimeters) and the microstructure of the same generic material (at a length-scale of microns).

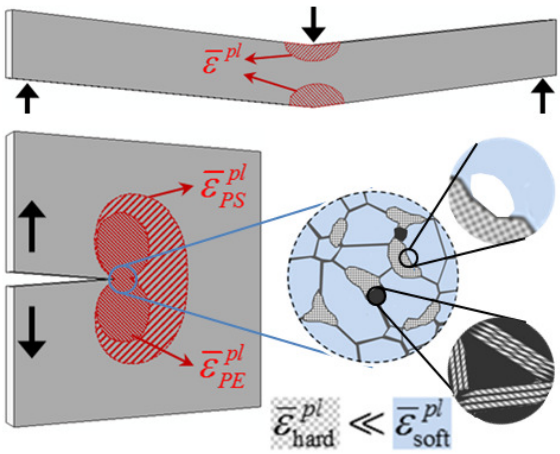

Figure 1.2: Schematic of plastic strain, $\bar{\varepsilon}^{pl}$, gradient arising from: geometry of deformation (3-point bending), local boundary conditions (notched sheet), and evolving multiphase microstructure, e.g. void nucleation and deformation-induced phase transformation.

design methodologies to achieve a targeted performance metric [32–46]. But there are relatively fewer efforts aimed at designing high strength, fracture resistant materials [47–52]. This is largely due to the complex deformation mechanisms and microstructures of advanced structural materials. Understanding fracture in these advanced materials remains an outstanding grand challenge.

Classical fracture mechanics has been an enormously successful engineering theory. However,

several significant issues remain that fall outside its scope, examples of which include: crack nucleation, and circumstances where the singular fields do not encompass the fracture process zone. Furthermore, in ductile multiphase materials, for example, advanced high strength steels, a loss of stress carrying capacity in the reinforcing phase due to void nucleation or deformation-induced phase transformation, Fig. 1.2, greatly affect the strain hardening response of the material and leads to a breakdown in scale separation [53], making it very challenging to mathematically represent the multiphase material as an "effective homogenized media" [54, 55]. These are just two example of additional mechanics related challenges that are posed by advanced structural materials. Understanding crack nucleation and crack growth resistance, in these advanced structural materials pose exciting Mechanics and Materials Science related issues. Following this, the main aim of this dissertation is to transform the field of classical fracture mechanics from the notion of structure $\rightarrow$ fracture to structure $\rightarrow$ microstructure $\rightarrow$ fracture, and provide a basis for designing more fracture resistant material microstructures.

Ductile fracture of metals and alloys containing heterogeneities such as particulates and precipitates, generally initiates at the heterogeneities. Subsequently, the damage propagates into the matrix by mechanisms such as void growth leading to void coalescence and nucleation of a macroscopic cracks. Experimental studies on ductile fracture have shown strong connections between the microstructural features, such as shape, size or spatial distribution of second phase particles, and damage nucleation and growth [56–60]. Computational studies have also been conducted to study elastic-plastic deformation and ductile fracture of heterogeneous materials [48, 61–79]. The computational studies can be divided into two categories: phenomenological and microstructure-based. In phenomenological fracture models, macroscopic experimental data are obtained and a damage evolution criteria is directly fit to the data. On the other hand, microstructure-based fracture modeling provides a direct microstructure-fracture connection. However, these studies have been largely limited to 2D or 3D representative volume elements of the microstructures under idealized periodic boundary conditions. There is a need to model ductile fracture in heterogeneous materials under more realistic boundary and loading conditions in order to better understand the interaction

of length-scales originating from the geometry/boundary conditions and material microstructure.

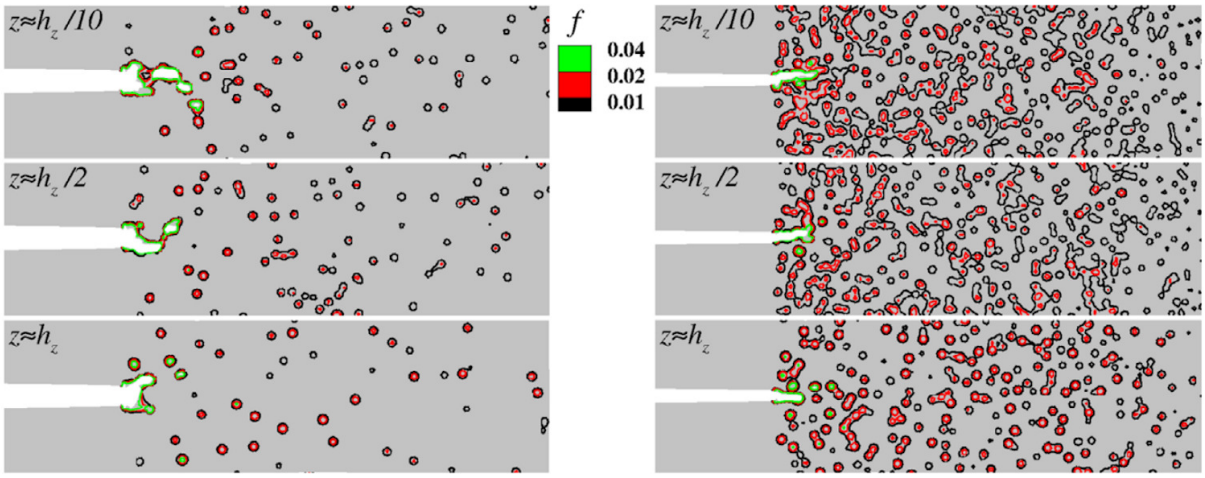

(a)

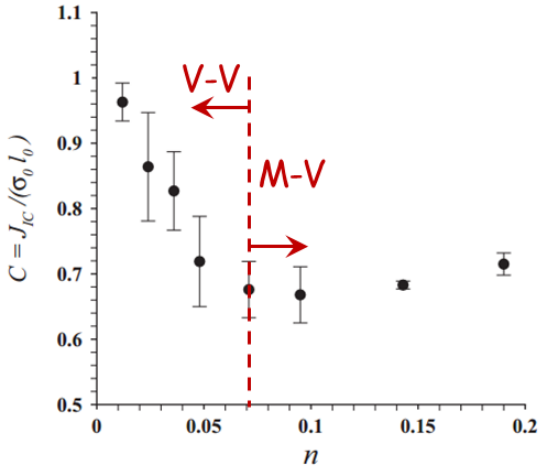

(b)

Figure 1.3: 3D calculations of ductile fracture under mode I plane strain, small scale yielding conditions for a progressively cavitating solid with discretely modeled void nucleating second phase particles or inclusions, reprinted from [1]. (a) Contours of void volume fraction f on three parallel planes through the thickness for an inclusion volume fraction n=0.024 and an inclusion volume fraction n=0.143. (b) Variation of the parameter $C = J_{IC}/(\sigma_0 l_0)$ (fracture toughness normalized with initial yield strength and mean inclusion spacing) with inclusion volume fraction n.

The microstructure of a variety of structural metals and alloys can be idealized as ductile matrix

with randomly distributed inclusions. The size, spacing and volume fraction of these inclusions introduce microstructure-based length-scales. Several attempts have been made in the past to correlate material microstructural parameters to materials fracture toughness for such structural materials. For example, in Fig. 1.3 [1], three dimensional calculations of ductile fracture under mode I plane strain, small scale yielding conditions for solids containing a distribution of inclusions were carried out. It was shown that the fracture toughness normalized by the mean inclusion spacing depends on the inclusion volume fraction for small inclusion volume fractions whereas for larger inclusion volume fractions it does not depend on the inclusion volume fraction. This raises several fundamental questions associated with inclusion driven ductile fracture: How does the interlacing of microstructural length-scales affect the micromechanisms of ductile crack advance and what is the micromechanism of ductile crack advance? In the present work, three dimensional, finite element, finite deformation, small scale yielding calculations of mode I crack growth are carried out for ductile material matrix consisting of two populations of void nucleating particles using an elasto-viscoplastic constitutive framework for progressively cavitating solid. The matrix material is modeled as an isotropic hardening elasto-viscoplastic solid together with two population of void nucleating particles. Larger particles or inclusions that result in void nucleation at an early stage are modeled discretely while smaller particles that require large strains to nucleate voids are homogeneously distributed. The size, spacing and volume fraction of inclusions introduce microstructure-based characteristic length-scales into the formulation. The calculations are carried out for three inclusion radii, and for a fixed inclusion radius, for six inclusion volume fractions. The results presented in the study provide guidelines for microstructural engineering to increase ductile fracture toughness, for example, the results show that for a material with small inclusions, increasing the mean inclusion spacing has a greater effect on fracture toughness than for a material with large inclusions.

The pressing need of our time to decrease anthropogenic emissions of greenhouse gasses requires use of high strength, fracture resistant structural materials such as advanced dual-phase (DP) steels to reduce vehicle weight and emissions. However, as the strength of dual-phase steels in-

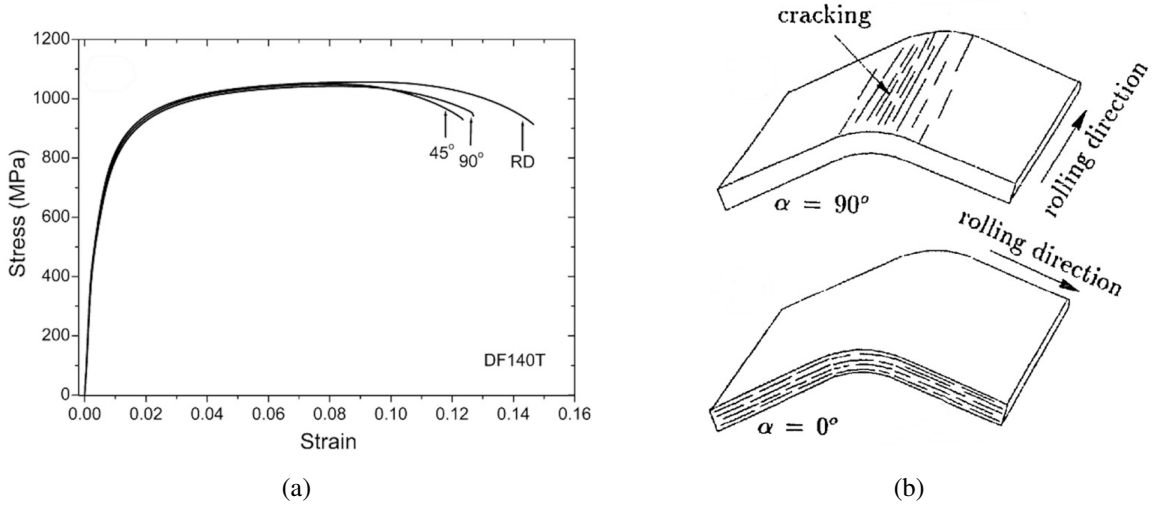

(a) (b)

Figure 1.4: (a) Uniaxial tensile stress-strain curves for a dual-phase steel, DF140T, with loading axis aligned parallel, perpendicular and at 45° to the rolling direction, reprinted from [2]. (b) Effect of anisotropy on bendability: sheet with bending axis parallel to the rolling direction exhibit poor bendability, and sheet with bending axis perpendicular to the rolling direction exhibit good bendability, reprinted from [3].

creases, the steel becomes more prone to ductile fracture under bending dominated manufacturing processes. In addition, DP steel sheets exhibit contrasting deformation and fracture anisotropy along the rolling direction (RD) and the transverse direction (TD) of the sheet under uniaxial tensile loading versus bending. Under uniaxial tension, DP steel sheets exhibit very similar or greater ductility with loading axis aligned parallel to the rolling direction than perpendicular to the rolling direction [2, 80]. But under bending, sheet with bending axis parallel to the rolling direction exhibit poor bendability [3] as shown in Fig. 1.4. Thus, here in the study, the effect of length-scales induced by the geometry of deformation, in particular bending, and the material microstructure on ductile fracture of DP advanced high strength steel (AHSS) sheets have been explored. To this end, microstructure-based finite element calculations of crack nucleation and early stage crack growth in DP steel sheets subjected to 90° V-bending have been carried out. In the calculations, the microstructural features, ferrite and martensite phases, of the DP steel are discretely modeled in a thin slice of bend specimen normal to the bend axis using a constitutive relation for progressively

cavitating elastic-viscoplastic solid. The calculations are carried out for several microstructures taken from both the RD and TD cross-section of a DP steel. Parametric studies are also carried out to explore the effect of material parameters that dictate the propensity of void nucleation, energy dissipated in the growth of nucleated voids prior to crack nucleation, and initial porosity on ductile fracture of DP steel sheets under bending. In-line with the experimental observations for a commercially produced DP steel, DP1000, the calculations predict that despite similar strength and strain hardenability, volume fraction of the phases and fracture response under uniaxial tension along RD and TD, the bendability of RD specimens are less than the bendability of TD specimens. The results of these calculations also show that efforts to improve the bendability of advanced dual-phase steels must focus on improving the properties of the ferrite phase.

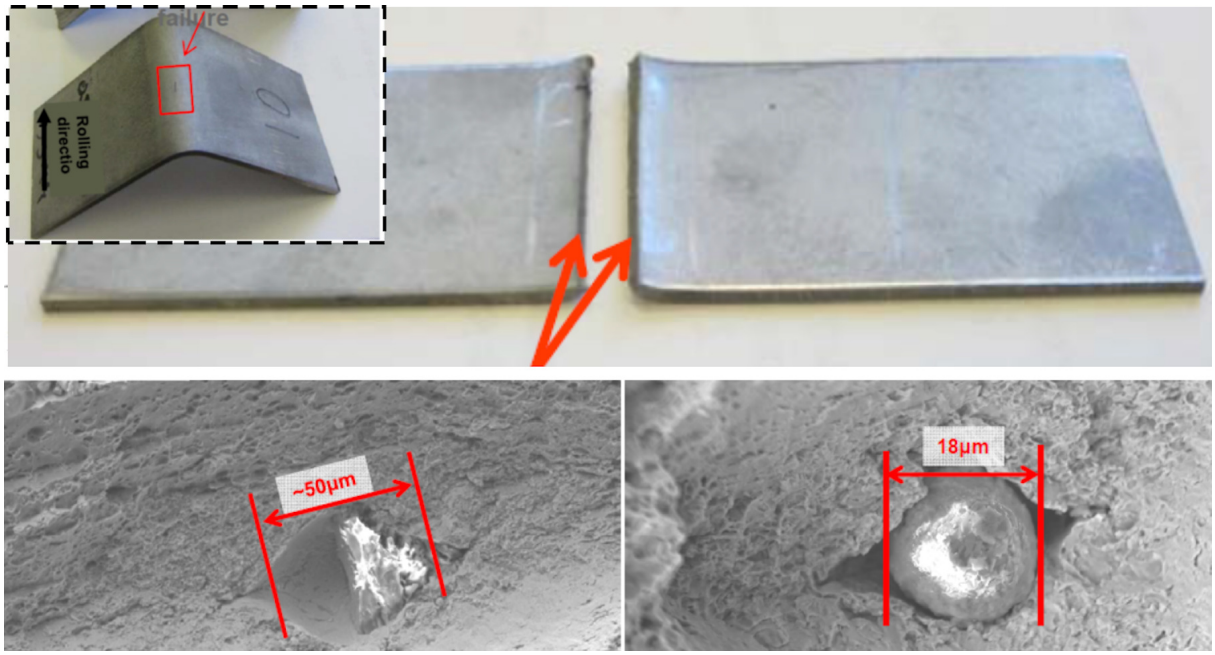

Figure 1.5: 90° V-bend testing of a commercially produced advanced DP steel, DP1000. Cracks and/or microcracks formed along the bend axis post bending indicating poor bendability performance of this steel. Bending cracks are associated with the presence of subsurface inclusions, reprinted from [4].

Another source that affects the bendability of commercially produced advanced DP steels is

the presence of inclusions. The experimental observations suggest that the bendability of DP steel sheets strongly depend on the size, location and type of non-metallic inclusions. For example, as shown in Fig. 1.5, cracks and microcracks were observed along the bend axis post 90° V-bending of a commercially produced DP steel, DP1000, with strength $\approx 1GPa$, and the root cause of poor bendability was identified as the presence of non-metallic inclusions. Furthermore, the experimental observations also suggest that unlike single-phase materials, inclusions in DP steels exhibit a discrete size effect. Here, building on the previous work, the microstructure-based finite element modeling are carried out to understand the interplay of the length scales induced by bending, intended microstructural features (ferrite-martensite), and size, shape, location and properties of unintended microstructural features (inclusions) on crack nucleation and early stage crack growth in advanced DP steel sheets. In line with the experimental observations, strong inclusion size effects on the bendability of the DP steel sheets compared to single-phase material naturally emerges in the calculations. Furthermore, supervised machine learning is utilized to quantify the effect of the multivariable input space associated with the inclusion and DP microstructure on the bendability of the steel. The results of supervised machine learning are then used to identify the contributions of individual features and isolate critical features that control the bendability of advanced high strength dual-phase steels.

To expand the current materials space, besides designing the microstructure of materials, the topological design of the structure of materials is another consideration. There are only few natural materials such as wood and bamboo that provide high fracture toughness at a density below that of water as is shown in Fig. 1.6. The potential of micro-architectured and lattice materials to combine high stiffness and strength at low densities is well documented, see highlights in Fig. 1.6(a). However, less is known about their capacity to have a high fracture toughness. One experimental work [9], reported the potential of Ti snap-fit octet truss with high fracture toughness and rather low density but still greater than most natural materials. Following this, the potential of micro-architectured materials to outperform natural materials is investigated. In addition, the question arises as to the extent to which the standard test procedure that was initially established

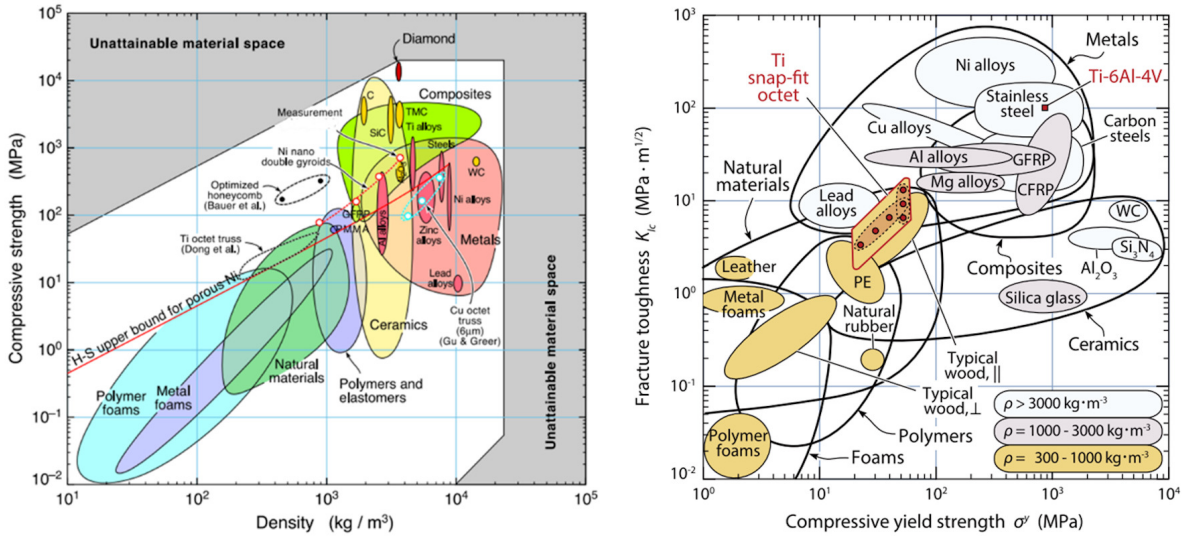

(a) (b)

Figure 1.6: (a) Strength versus density Ashby chart. The measured properties of macro Ti octet truss lattices [5], Cu micro octet truss lattices [6], Ni nano double gyroids [7], and micro ceramic honeycombs [8] are highlighted. (b) Material property map of the fracture toughness, K_{IC}, and compressive yield strength, σ_y, space. Ti snap-fit octet truss data are highlighted with red circles, reprinted from [9].

for specimens of bulk materials is applicable to micro-architectured and lattice materials. In the present work, the micro-architectured materials are manufactured by drilling hexagonal array of holes in plates of an aluminum alloy, and the fracture toughness is evaluated using three-point bending tests of single-edge notch specimens. The results show that the fracture toughness of micro-architectured materials increase with increasing relative density and remarkably, a lattice can be 50% lighter than the parent material but maintain the same fracture toughness. The experiments are complemented by finite element calculations of ductile fracture. In the calculations, the fracture toughness of single-edge notch specimens subjected to three-point bending are evaluated using both, a procedure similar to the experiments and direct computation of J-integral. The fracture toughness calculated using both the methods are found to be consistent with the experimental results. In addition, the calculations are also carried out for single-edge notch specimens subjected to tensile loading that show the same scaling between fracture toughness and relative density of

micro-architectured materials. The results show that it is possible to design micro-architectured materials that possess an exceptional combination of high strength and fracture toughness at low densities that no fully-dense material can offer.

In summary, in my PhD work, I have focused on correlating the length-scales induced by the geometry of deformation, loading conditions and microstructure of the materials to ductile fracture through large-scale microstructure-based finite element calculations. The overarching goal is to transform the field of classical fracture mechanics from the notion of structure $\rightarrow$ fracture to structure $\rightarrow$ microstructure $\rightarrow$ fracture and enable the design and discover of more fracture resistant, high strength, structural materials. The ability to predict microstructure-based nucleation and growth of macroscopic cracks also provides the basis for assessing the reliability of components as well as product quality in a variety of manufacturing processes.

2. MODELING DUCTILE FRACTURE

2.1 Introduction

At room temperature, ductile fracture of structural metals and alloys in general involves void nucleation, growth and coalescence as shown in Fig. 2.1. In these materials void nucleation occurs by debonding of particles from the matrix or interfaces, or cracking of brittle particles. These nucleated voids or any pre-existing voids then grow by plastic deformation in the matrix. Finally, the growing voids coalesce either by impingement or through void sheet.

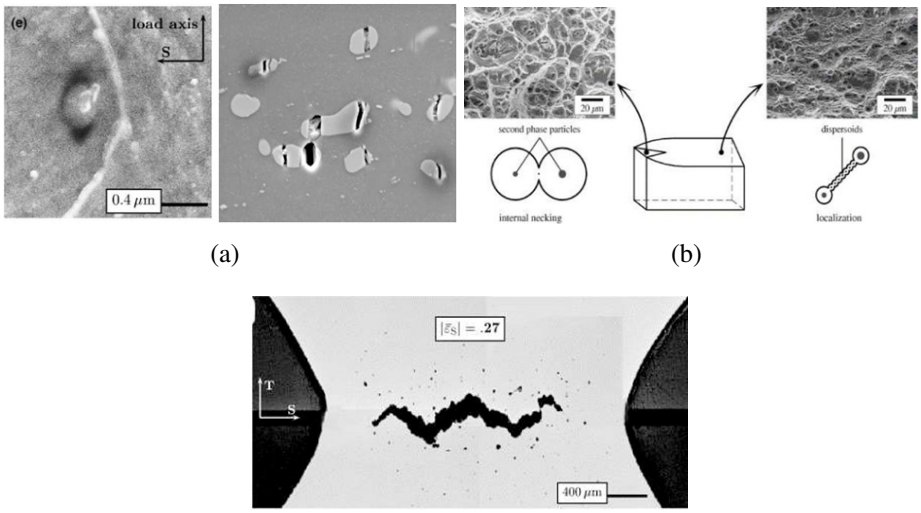

Figure 2.1: Ductile fracture process. (a) Void nucleation at inclusions, reprinted from [10]. (b) Fracture surfaces showing ductile fracture post void coalescence either due to internal necking between growing voids or localization between growing voids, reprinted from [11]. (c) Formation of macroscopic crack in a specimen leading to final fracture, reprinted from [10].

Characterization of fracture following classical fracture mechanics involves fracture tests of specimens with pre-existing cracks and estimation of crack growth resistance. The classical fracture mechanics has been an enormously successful engineering theory. However, several signif-

icant issues remain that fall outside its scope, examples of which include: crack nucleation, and circumstances where the singular fields do not encompass the fracture process zone. Predicting fracture response of a material through micromechanical simulations not only provides a direct connection between material microstructure, properties and fracture response, but also enables prediction of crack nucleation, fracture characterization under circumstances where classical fracture mechanics losses validity as well as it can serve as a basis for designing fracture resistant materials. Thus, micromechanical numerical simulation of ductile fracture involving void nucleation, growth and coalescence is of great interest for a variety of applications. The first micromechanical model of ductile fracture due to void growth and coalescence was developed by McClintock [81] and Rice and Tracey [82] that described the growth of isolated voids in a rigid perfectly plastic matrix. Both studies outlined the combined role of stress triaxiality and plastic strain on ductile void growth. Later, Gurson [83] carried out an upper bound analysis of a finite sphere containing a spherical void in a rigid perfectly plastic matrix. The Gurson model was further improved by Tvergaard and Needleman [84] to better account for void interactions and coalescence. The Gurson-Tvergaard-Needleman constitutive framework has several limitations such as the evolution of void shape is ignored, porosity induced softening is the only damage mechanism and it does not inherently contain a material length-scale. Some work have been done to improve The Gurson-Tvergaard-Needleman model for example, Gologanu and coworkers [85, 86] have developed models to account for initial void shapes and void shape evolution. Nonetheless, the Gurson-Tvergaard-Needleman model is simple and robust and provides reasonable predictions of ductile fracture at sufficiently high stress triaxialities. Also, the absence of a material length-scale in the Gurson-Tvergaard-Needleman model can be accounted for, by discretely modeling the material microstructure as is done in this dissertation.

2.2 Numerical Method

The finite element calculations in this dissertation are based on the dynamic principle of virtual work written in tensor notation as

$$\int_V \tau^{ij}\delta E_{ij}dV = \int_S T^i \delta u_i dS - \int_V \rho \frac{\partial^2 u^i}{\partial t^2}\delta u_i dV \tag{2.1}$$

where, τ^{ij} are the contravariant components of the Kirchhoff stress in the deformed convected coordinate net (τ^{ij} = $J\sigma^{ij}$,with σ^{ij} being the contravariant components of the Cauchy stress and J being the ratio of the current to reference volume), E_{ij} is the Lagrangian strain tensor, ρ is the mass density, V and S are the volume and surface of the body in the referencecon figuration.

The constitutive framework used here is the modified Gurson elastic-viscoplastic constitutive relation for a progressively cavitating solid [83, 84, 87] with the flow potential having the form

$$\phi = \frac{\sigma_e^2}{\bar{\sigma}^2} + 2q_1 f^* \cosh\left(\frac{3q_2\sigma_h}{2\bar{\sigma}}\right) - 1 - (q_1 f^*)^2 \tag{2.2}$$

where q_1, q_2 are parameters introduced in [88, 89], f^* is the effective void volume fraction, $\bar{\sigma}$ is the matrix flow strength, and

$$\sigma_e{}^2 = \frac{3}{2}\boldsymbol{\sigma}' : \boldsymbol{\sigma}' \quad , \quad \sigma_h = \frac{1}{3}\boldsymbol{\sigma} : \mathbf{I} \quad , \quad \boldsymbol{\sigma}' = \boldsymbol{\sigma} - \sigma_h \mathbf{I} \tag{2.3}$$

For $f^* = 0$, the flow potential in Eq. (2.2) reduces to the Mises flow potential. The function f^*, introduced in [84], is given by

$$f^* = \begin{cases} f, & f < f_c \\ f_c + (1/q_1 - f_c)(f - f_c)/(f_f - f_c), & f \geq f_c \end{cases} \tag{2.4}$$

where f_c is the critical void volume fraction to void coalescence and f_f is the void volume fraction at failure. When the value of the void volume fraction, f, at an integration point reaches $0.9f_f$, the value of f is kept fixed so that the material deforms with a very low flow strength. The

entire element is taken to vanish following the technique proposed in [90] when three of the eight integration points in the element have reached this stage as in [1, 29, 47, 91].

The rate of deformation tensor is taken as the sum of an elastic part, $\mathbf{d}^e = \mathbf{L}^{-1} : \hat{\boldsymbol{\sigma}}$, and a viscoplastic part, $\mathbf{d}^p$, so that

$$\mathbf{d} = \mathbf{L}^{-1} : \hat{\boldsymbol{\sigma}} + \mathbf{d}^p \tag{2.5}$$

Here, $\hat{\boldsymbol{\sigma}}$ is the Jaumann rate of Cauchy stress and $\mathbf{L}$ is the tensor of isotropic elastic moduli characterized by Young's modulus, E, and Poisson's ration, ν. The plastic part of the strain rate, $\mathbf{d}^p$, is given by [92]

$$\mathbf{d}^p = \left[\frac{(1-f)\bar{\sigma}\dot{\bar{\varepsilon}}}{\boldsymbol{\sigma} : \frac{\partial \phi}{\partial \boldsymbol{\sigma}}}\right] \frac{\partial \phi}{\partial \boldsymbol{\sigma}} \tag{2.6}$$

The matrix plastic strain rate, $\dot{\bar{\varepsilon}}$, is given by

$$\dot{\bar{\varepsilon}} = \dot{\varepsilon}_0 \left[\frac{\bar{\sigma}}{g(\bar{\varepsilon})}\right]^{1/m} \quad , \quad g(\bar{\varepsilon}) = \sigma_0 \left[1 + \bar{\varepsilon}/\varepsilon_0\right]^N \tag{2.7}$$

with $\bar{\varepsilon} = \int \dot{\bar{\varepsilon}} dt$. In Eq. (2.7), $\dot{\varepsilon}_0$ is the reference strain rate, m is the strain rate sensitivity exponent, σ_0 is the reference flow strength, ε_0 is a reference strain and N is the strain hardening exponent.

The evolution of the void volume fraction is governed by

$$\dot{f} = (1-f)\mathbf{d}^p : \mathbf{I} + \dot{f}_{nucl} \tag{2.8}$$

where the first term on the right hand side of Eq. (2.8) accounts for void growth and the second term accounts for void nucleation. The value of f in the undeformed material i.e. value of f at time, $t = 0$, represents the initial void volume fraction, f_0. The void nucleation rate, $\dot{f}_{nucl}$, is related to the accumulated plastic strain, $\bar{\varepsilon}$, and plastic strain rate, $\dot{\bar{\varepsilon}}$, by [87]

$$\dot{f}_{nucl} = \frac{f_N^{\varepsilon}}{s_N^{\varepsilon}\sqrt{2\pi}} \exp\left[-\frac{1}{2}\left(\frac{\bar{\varepsilon} - \varepsilon_N}{s_N^{\varepsilon}}\right)^2\right] \dot{\bar{\varepsilon}} \tag{2.9}$$

with f_N^{ε}, ε_N, and s_N^{ε} being the constitutive parameters. The Eq. (2.9) is based on the hypothesis that there is a mean equivalent plastic strain, ε_N, for void nucleation and that this nucleation strain is distributed in a normal fashion about the mean with standard deviation, s_N^{ε}. The parameter f_N^{ε} determines the maximum void volume fraction nucleated at a material (Gaussian) integration point. For stress controlled nucleation

$$\dot{f}_{nucl} = \frac{f_N^{\sigma}}{s_N^{\sigma}\sqrt{2\pi}} \exp\left[-\frac{1}{2}\left(\frac{\bar{\sigma} + \sigma_h - \sigma_N}{s_N^{\sigma}}\right)^2\right] [\dot{\bar{\sigma}} + \dot{\sigma}_h] \tag{2.10}$$

with f_N^{σ}, σ_N, and s_N^{σ} being the constitutive parameters. If $(\bar{\sigma} + \sigma_h) \geq (\bar{\sigma} + \sigma_h)_{max}$, where the maximum is taken over the previous mechanical history, and $\partial(\bar{\sigma} + \sigma_h)/\partial t > 0$.

Eight point Gaussian integration is used in each twenty-node element for integrating the internal force contributions and twenty-seven point Gaussian integration is used for the element mass matrix. Lumped masses are used so that the mass matrix is diagonal. The discretized equations are integrated using the explicit Newmark β-method with $\beta = 0$ [93]. The constitutive updating is based on the rate tangent modulus method proposed in [94], while material failure is implemented via the element vanish technique proposed in [90].

3. MICROMECHANISM AND IMPLICATIONS OF INCLUSION DRIVEN DUCTILE FRACTURE*

3.1 Background

The objective of this work is to correlate the macroscopic fracture toughness of heterogeneous ductile materials with the fracture mechanisms operating at the microscale. The focus is confined to ductile structural materials undergoing fracture due to nucleation, growth and coalescence of microscale voids [95–99]. The microstructure of such materials can be idealized as a ductile material matrix with randomly distributed inclusions or second phase particles, as is encountered in a variety of ferrous and aluminum alloys. The second phase particles in such materials are either added intentionally to the material's microstructure, for precipitation-hardening or dispersion-strengthening [100], or their formation is an unavoidable consequence of processing [101].

There is an important difference between the characterization of fracture in a deformation field that is more or less uniform and the characterization of fracture in a deformation field that is heterogeneous [1, 12, 102–107]. In the former, an unstructured continuum description of ductile fracture, in principle, can be based on material parameters such as strength and strain hardening exponent. On the other hand, in the latter, the macroscopic fracture toughness must involve characteristic length-scales associated with the material microstructure. This expected dependence of fracture toughness on material length-scales is consistent with the experimental results of ductile fracture due to nucleation, growth and coalescence of microscale voids in ductile structural materials [108–122].

Several attempts have been made in the past to correlate material microstructural parameters such as volume fraction, size and spacing of the inclusions/voids with the macroscopic fracture toughness of the material. The mode I plane strain fracture toughness, K_{IC}, of several ductile materials has been shown to follow $K_{IC} = EN(2\pi L)^{\frac{1}{2}}$ [109] or $K_{IC} \approx \sqrt{2\sigma_0 E\lambda}$ [123], where

*Reprinted with permission from "On the micromechanism of inclusion driven ductile fracture and its implications on fracture toughness" by **Liu, Y.**, Zheng, X., Osovski, S. and Srivastava, A., 2019. *Journal of the Mechanics and Physics of Solids*, 130, pp.21-34, Copyright 2019 by Elsevier.

E is Young's modulus, N is the work hardening coefficient, σ_0 is the flow strength, L is the size of the process zone and λ is the spacing of the nearest void/inclusion from the initial crack tip. Often the process zone size has been hypothesized to correlate with the microstructural length-scale set by the pre-existing inclusions in the material [110, 111, 113]. These suggest that the fracture toughness of the material predominantly depends on a single length-scale introduced by the mean (or extreme) spacing of the inclusions/voids. On the other hand, the fracture toughness of the material has been suggested to depend not only on the mean spacing but also on the size of the inclusions/voids. For example, the material's fracture toughness defined in terms of J_{IC} has been suggested to correlate with two microstructural length-scales as, $J_{IC} \propto \sigma_0 \left(2/{N_i}^{1/3}\right) \ln\left(r_c/r_0\right)$, where N_i is the number of inclusions per unit volume ($1/{N_i}^{1/3}$ is the mean inclusion spacing, l_0), r_0 is the initial size of the inclusions and r_c is the radius of the cavities at failure nucleated from these inclusions [124]. [117] carried out an experimental study to distinguish the influence of overall volume fraction, spacing and size of pre-existing voids/holes on material's ductility. Their experimental observation suggests that the spacing and size of the pre-existing voids has a larger effect on ductility compared to their volume fraction. The dominant effect of the spacing and/or size of the pre-existing inclusions/voids over their volume fraction on macroscopic fracture toughness has also been suggested by [120, 125, 126].

The extent to which fracture toughness of a ductile material depends on the overall microstructural parameter i.e. volume fraction, or spacing and size of pre-existing voids has been associated with the micromechanisms of ductile crack advance. In general, two micromechanisms of ductile crack advance in a ductile material with preexisting distribution of voids have been proposed: crack advance by a void-by-void micromechanism and crack advance by multiple-void interaction [127–133]. It has been suggested that for void-by-void micromechanism, $J_{IC}/(\sigma_0 l_0)$ or δ_c/l_0 (δ_c being the critical crack-tip opening displacement) depends on the initial void volume fraction whereas for multiple-void interaction micromechanism, $J_{IC}/(\sigma_0 l_0)$ or δ_c/l_0 does not depend on the initial void volume fraction. At the microscale, crack advance by the void-by-void micromechanism involves coalescence of the crack tip with the closest void [102,104], whereas crack advance

by multiple-void interaction involves simultaneous interaction of multiple voids ahead of the crack tip [127]. The transition from the crack advance by the void-by-void micromechanism to multiple-void interaction has been shown to depend on the initial void volume fraction [127, 128], wherein void-by-void micromechanism is operative at low initial void volume fraction and multiple-void interaction micromechanism is operative at high initial void volume fraction. However, [130], suggested that other factors such as initial distribution of the voids can also affect the transition from void-by-void to multiple-void interaction micromechanism of ductile crack advance.

There is a distinct advantage of modeling discrete voids in a ductile matrix in the finite element calculations, e.g. [127,130], as this approach directly models the void growth behavior in the vicinity of a crack tip. However, it doesn't not naturally account for ductile crack advance. In addition, the class of ductile structural materials considered here, often contains a three-dimensional distribution of two populations of void nucleating particles: larger particles or inclusions (e.g. MnS inclusions in steels) that nucleate voids at relatively small strains and smaller particles (e.g. carbides in steels) that nucleate voids at larger strains. The voids nucleate either by debonding or cracking of the particles [134–136]. Furthermore, the three-dimensional distribution of inclusions in a ductile matrix can promote crack meandering [1, 105, 107] and microcracking [1, 137] ahead of the initial crack tip well before the overall crack growth. Nevertheless, in [1] it was shown that for a fixed initial inclusion size, $J_{IC}/(\sigma_0 l_0)$ depends on the inclusion volume fraction for small inclusion volume fractions whereas for larger inclusion volume fractions $J_{IC}/(\sigma_0 l_0)$ does not depend on the inclusion volume fraction. This raises several fundamental questions associated with inclusion driven ductile fracture: (i) Is the dependence of $J_{IC}/(\sigma_0 l_0)$ on inclusion volume fractions is due to the transition from void-by-void to multiple-void interaction micromechanism of ductile crack advance as has been suggested for ductile materials with pre-existing voids? (ii) How does the interlacing of two microstructural length-scales, inclusion spacing and size, affect the micromechanisms of ductile crack advance? (iii) How does the matrix material properties such as, strain hardening exponent, susceptibility to secondary void nucleation and energy dissipated in the growth of the nucleated voids prior to crack advance affect the micromechanisms of ductile crack

advance?

To this end, finite element, finite deformation calculations are carried out using a constitutive framework for progressively cavitating ductile solid. The matrix material is modeled as an isotropic hardening elasto-viscoplastic solid together with two population of void nucleating particles. Larger particles or inclusions that result in void nucleation at an early stage are modeled discretely while smaller particles that require large strains to nucleate voids are homogeneously distributed. The size, spacing and volume fraction of inclusions introduce microstructure-based characteristic length-scales into the formulation. The calculations are carried out for small scale yielding conditions under remote Mode I loading. In the calculations, ductile crack growth are computed to the sufficient extent to be able to characterize the fracture toughness of the material in terms of J_{IC} using a procedure mimicking the [14]. The extent to which the microstructural parameters such as volume fraction, size and spacing of the inclusions, and the properties of the matrix material affect the micromechanisms of ductile crack advance and hence the macroscopic fracture toughness of the material is discussed. The results presented also provide guidelines for microstructural engineering to increase fracture toughness.

3.2 Problem formulation

A mode I small scale yielding boundary value problem is analyzed for a slice of material with an initial through thickness crack, as shown in Fig. 3.1. The slice of material analyzed has the dimensions $h_x \times h_y \times h_z$, where, $h_x = h_y = 0.4$m and $h_z/h_x = 0.0125$. The finite element mesh consists of $428,256$ twenty node brick elements giving $1,868,230$ nodes and $5,604,690$ degrees of freedom. Ten uniformly spaced elements are used through the thickness h_z. A uniform 208×64 in-plane ($x-y$ plane) mesh is used in a 0.02m $\times$ 0.006m region immediately in front of the initial crack front with in-plane elements of dimension 9.62×10^{-5}m by 9.38×10^{-5}m. The element dimension $e_x = 9.62 \times 10^{-5}$m serves as a normalization length. The initial crack front with an initial opening $b_0 = 1.95e_x$ lies along $(0, 0, z)$ and the crack faces remain traction free. In the $x-y$ plane, velocity boundary conditions corresponding to linear isotropic mode I crack tip field are prescribed,

$$\dot{u}_x\left(R,\theta,z,t\right)=\frac{2\left(1+\nu\right)\dot{K}_I}{E}\sqrt{\frac{R}{2\pi}}\cos\frac{\theta}{2}\left(1-2\nu+\sin^2\frac{\theta}{2}\right) \tag{3.1}$$

$$\dot{u}_y\left(R,\theta,z,t\right)=\frac{2\left(1+\nu\right)\dot{K}_I}{E}\sqrt{\frac{R}{2\pi}}\sin\frac{\theta}{2}\left(2-2\nu-\cos^2\frac{\theta}{2}\right) \tag{3.2}$$

Here, $R^2=x^2+y^2$ and $\theta=\tan^{-1}\left(y/x\right)$ for points on the boundary of the region analyzed, $\dot{K}_I$ is the prescribed rate of increase of the mode I stress intensity factor. Also, symmetry boundary conditions are imposed on $z=0$, h_z planes. The value of $\dot{K}_I/\left(\dot{\epsilon}_0\sigma_0\sqrt{e_x}\right)=1359.4$ is prescribed for it to be same as in [1,47]. The finite element calculations are based on the dynamic principle of virtual work using a finite deformation Lagrangian convected coordinate formulation. The calculations are based on the dynamic principle of virtual work for numerical convenience, hence to minimize the wave effects, initial velocity fields at $t=0$ consistent with Eqs. (3.1) and (3.2) are prescribed throughout the region analyzed.

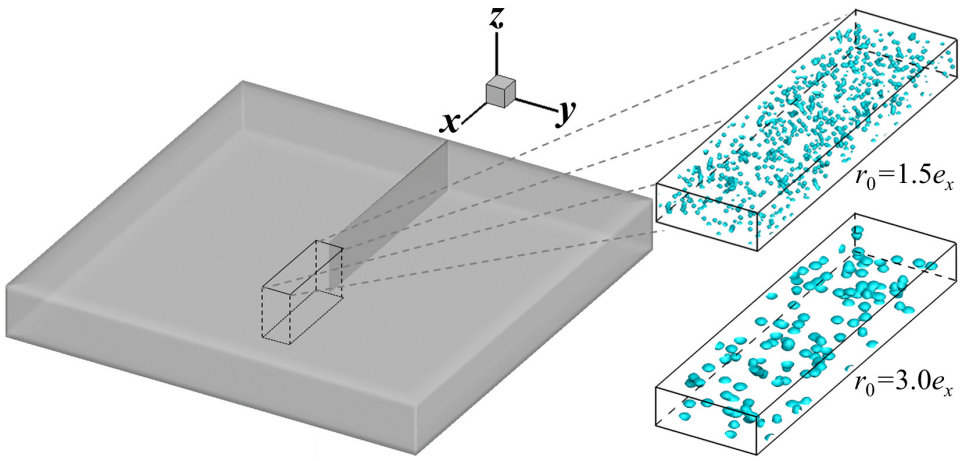

Figure 3.1: Sketch of the initially cracked block of material analyzed together with the magnified view of the three-dimensional random distributions of inclusions in front the initial crack. For the two distributions shown: (top right) radius of the inclusions, $r_0=1.5e_x$ and volume fraction, $n=0.024$; and (bottom right) radius of the inclusions, $r_0=3.0e_x$ and volume fraction, $n=0.024$. The parameter e_x is the normalization length parameter.

3.2.1 Microstructure generation

In the calculations the material microstructure is characterized by two populations of void nucleating particles: (i) uniformly distributed small particles that are modeled by plastic strain controlled void nucleation; and (ii) large particles or inclusions that are modeled as stress controlled nucleation sites. In each case, void nucleation is assumed to be described by a normal distribution following [87].

For plastic strain nucleation, follows the Eq. (2.9) with $f_N^{\varepsilon} = 0.04$, $\epsilon_N = 0.3$ and $s_N^{\varepsilon} = 0.1$. Parametric studies are also carried out to explore the effect of the mean equivalent plastic strain to void nucleation in the matrix material, ϵ_N, on the fracture toughness for fixed microstructures.

The stress controlled nucleation follows the Eq. (2.10). To generate the random distribution of inclusions (modeled discretely as stress controlled nucleation sites, Eq. (2.10)) within the uniform mesh region of volume, $V_u = 200e_x \times 60e_x \times 50e_x$, in front of the initial crack front, firstly, randomly generate predetermined number of inclusion, N_{incl}, centers (x_0, y_0, z_0) with the restriction that the center to center distance of two neighboring inclusions is at least twice the radius, r_0. The value of f_N^{σ} in Eq. (2.10) at a material (Gaussian) point (x, y, z) in the initial undeformed configuration, is then assigned as,

$$f_N^{\sigma} = \begin{cases} \bar{f}_N \quad \text{for } \sqrt{(x-x_0)^2 + (y-y_0)^2 + (z-z_0)^2} \leq r_0 \\ \\ 0 \quad \text{for } \sqrt{(x-x_0)^2 + (y-y_0)^2 + (z-z_0)^2} > r_0 \end{cases} \tag{3.3}$$

The values $\bar{f}_N = 0.04$, $s_N^{\sigma}/\sigma_0 = 0.2$ and $\sigma_N/\sigma_0 = 1.5$ are used in the calculations. The inclusion volume fraction n, and the mean inclusion spacing l_0 are estimated as, $n = (N_{incl} \times 4\pi r_0^3/3)/V_u$ and $l_0 = (V_u/N_{incl})^{1/3}$, respectively. The inclusions introduce microstructure-based characteristic length-scales into the formulation, one associated with their spacing and the other with their size. Two random distributions of inclusions with $n = 0.024$, and $r_0 = 1.5e_x$ and $3.0e_x$ in the volume V_u, ahead of the initial crack front are shown in Fig. 3.1.

3.2.2 Constitutive parameters

The constitutive framework described in Section 2.2 contains several constitutive (material) parameters. The constitutive framework employed in this work includes many of the hardening and softening mechanisms shown by ductile metallic materials. The values of the constitutive and material parameters used here follows the work of [1]. Most material parameters, such as elastic constants and reference yield stress, are representative of aluminum alloys. The initial density, however, is taken to be greater than that for aluminum to increase the stable time increment in the dynamic calculations.

3.3 Results and Discussion

The calculations are carried out for three radii, $r_0 = 1.5e_x$, $3.0e_x$ and $4.5e_x$ (where e_x is the normalization length parameter) of inclusions, and for a fixed r_0 the calculations are carried out for six inclusion volume fractions, $n = 0.012$, 0.024, 0.048, 0.071, 0.095 and 0.19. In addition, for a fixed r_0 and n, the calculations are carried out for five random distributions of inclusion centers i.e. five realizations of the same overall microstructure. Parametric studies are also carried out to explore the effect of the matrix material properties on the micromechanisms of ductile crack advance and fracture toughness of the material.

3.3.1 Crack growth resistance

Crack growth resistance ($J - R$) curves, plots of J versus Δa, are extracted from all the calculations following the procedure adopted in [1, 29, 47, 91]. The value of J is calculated from the applied value of K_I using the relation [138],

$$J = K_I^2 \frac{(1 - \nu^2)}{E} \tag{3.4}$$

and the crack growth extension, Δa, is obtained by averaging the maximum projected length of the $f = 0.1$ contours through the thickness of the block of the material analyzed, Fig. 3.1.

The normalized $J - R$ curves for two inclusion radii, $r_0 = 1.5e_x$ and $4.5e_x$ and for each r_0, two

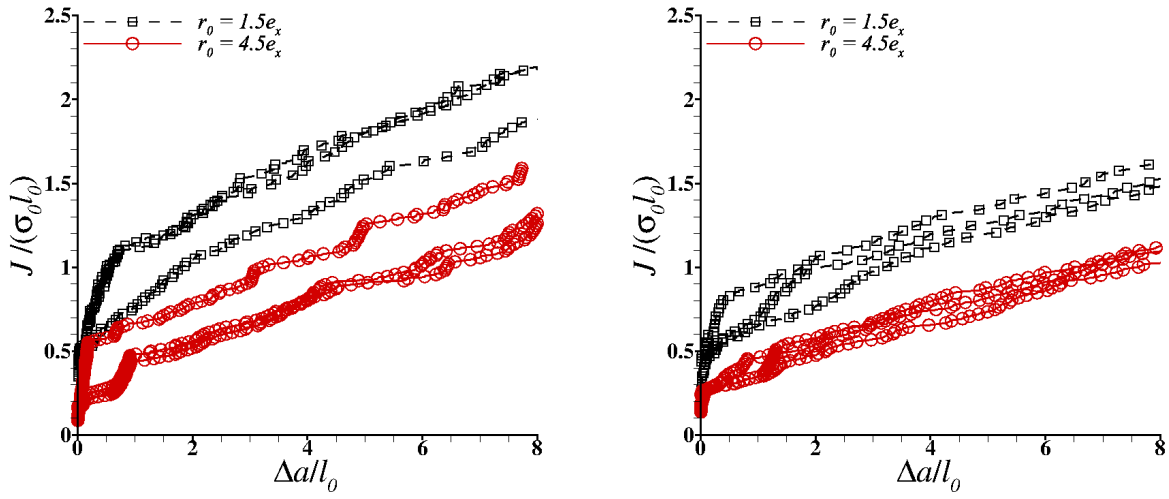

Figure 3.2: Applied normalized J, $J/(\sigma_0 l_0)$, versus normalized crack extension, $\Delta a/l_0$, curves for two inclusion radii, $r_0 = 1.5e_x$ and $4.5e_x$ with overall inclusion volume fractions, (a) $n = 0.024$ and (b) $n = 0.095$. For a fixed r_0 and n, results are shown for three random distributions of the inclusions.

inclusion volume fractions, $n = 0.024$ and 0.095 are shown in Fig. 3.2. For a fixed r_0 and n, the crack growth resistance curves are shown for three realizations of the same overall microstructure. In Fig. 3.2, the value of J is normalized by $\sigma_0 l_0$, while Δa is normalized by l_0. As seen in Fig. 3.2, for a fixed inclusion volume fraction, the level of the normalized $J - R$ curve is greater for the smaller inclusion radius, and for a fixed inclusion radius, the level of the normalized $J - R$ curve is greater for the smaller inclusion volume fraction. The variation in the $J - R$ curves between different realizations of the microstructure with a fixed r_0 and n, mainly stems from the initial stage of crack growth. The initiation of crack growth depends on the interaction of the initial crack front with the nearest inclusions. Thus, for smaller inclusion volume fraction, Fig. 3.2a, the variation among the various realizations is greater than the larger inclusion volume fraction, Fig. 3.2b.

The fracture initiation toughness, J_{IC}, is computed based on a procedure mimicking the [14], where a power law of the form $J = A(\Delta a)^B$ is fit to the portion of the $J - R$ curve in between two exclusion lines, $J = 2\sigma_0(\Delta a - 1.5e_x)$ and $J = 2\sigma_0(\Delta a - 5e_x)$. The value of J_{IC} is then

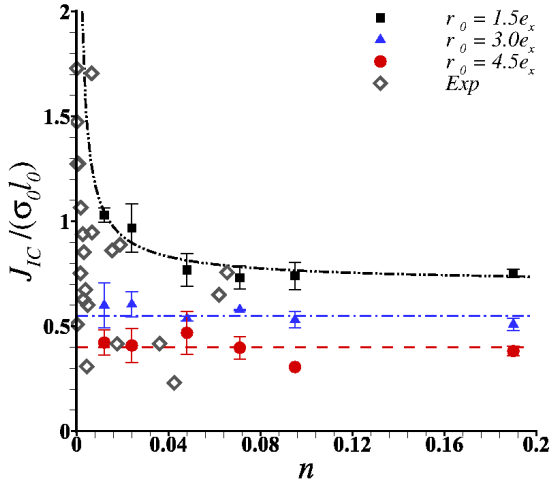

Figure 3.3: Variation of normalized fracture toughness, J_{IC}, $J_{IC}/\left(\sigma_0 l_0\right)$, with inclusion volume fraction, n, for three inclusion radii, $r_0 = 1.5e_x$, $3.0e_x$ and $4.5e_x$. The lines are the fitted curves and the data labeled, Exp, are the experimental results summarized by [12]. In the experiments, the crack-tip opening displacement at initiation of crack growth, δ_c, were measured that are converted to J_{IC}, following the relation, $J_{IC} = m\sigma_0\delta_c$ [13], where $m = 1$.

defined as the intersection of the curve $J = A(\Delta a)^B$ and the line $J = 2\sigma_0(\Delta a - 2e_x)$. The variation of normalized fracture toughness, $J_{IC}/(\sigma_0 l_0)$, with inclusion volume fraction, n, for three inclusion radii are shown in Fig. 3.3. The error bars in Fig. 3.3 show the standard errors (standard deviation divided by the square root of the number of realizations) for realizations of inclusion distributions having the same value of r_0 and n. The dash-dot lines in Fig. 3.3 for $r_0 = 1.5e_x$ show a fit to $J_{IC}/(\sigma_0 l_0) = C_1 n^{C_2} + C_3 r_0 + C_4$, and for $r_0 = 3.0e_x$ and $4.5e_x$ show a fit to $J_{IC}/(\sigma_0 l_0) = C_3 r_0 + C_4$, where $C_1 = 0.01$, $C_2 = -0.8$, $C_3 = -0.1e_x$ and $C_4 = 0.85$. The results presented in Fig. 3.3 show that for a fixed set of material parameters, for the smallest inclusion radius considered here, $r_0 = 1.5e_x$, the value of $J_{IC}/(\sigma_0 l_0)$ decreases rapidly with increasing n for $n \leq 0.071$ and then tends to saturate. But for the two larger inclusion radii, $r_0 = 3.0e_x$ and $4.5e_x$, the value of $J_{IC}/(\sigma_0 l_0)$ is rather independent of n, for the range of n considered.

In all the previous works, on the interaction of: (i) explicitly modeled two-dimensional distribution of (cylindrical plane-strain) voids or three-dimensional distribution of (spherical) voids

with a blunting crack tip [12,102,104,128,139,140], or (ii) explicitly modeled two-dimensional or three-dimensional distribution of (void nucleating) inclusions with a growing crack tip [1,105], the focus was confined on correlating macroscopic fracture initiation toughness defined using δ_c/l_0 or $J_{IC}/(\sigma_0 l_0)$ with the microstructural parameter defined either using the ratio of mean void/inclusion spacing and size, $l_0/2r_0$ or void/inclusion volume fraction, n (where $n \propto (r_0/l_0)^3$). These calculations predict that for a fixed set of material parameters, the value of δ_c/l_0 or $J_{IC}/(\sigma_0 l_0)$ is uniquely related to $l_0/2r_0$ or n, and the value of δ_c/l_0 or $J_{IC}/(\sigma_0 l_0)$ initially increases rapidly with increasing $l_0/2r_0$ (decreasing n) and then tends to saturate. These calculations did not predict the variation in the values of $J_{IC}/(\sigma_0 l_0)$ for a fixed n. In Fig. 3.3, show that for high inclusion volume fraction $J_{IC}/(\sigma_0 l_0)$ depends on the inclusion size whereas for low inclusion volume fraction $J_{IC}/(\sigma_0 l_0)$ depends on both the inclusion size and the inclusion volume fraction. The normalized experimental results plotted in Fig. 3.3 follows the same trend even though the experimental results are for a wide variety of engineering metals and alloys. The experimental results shown in Fig. 3.3 were summarized by [12], further details of the experimental results can be found in the references given in [12]. These experimental results were also used for comparison purposes in [104,105,127,139].

3.3.2 Micromechanism of ductile crack advance

Whether or not $J_{IC}/(\sigma_0 l_0)$ or δ_c/l_0, depends on the overall microstructural parameter i.e. volume fraction of the initial voids or the inclusions, n, has been associated with the void-by-void or multiple-void interaction micromechanism of ductile crack advance, respectively [1,127,128]. Following this, from the variation of $J_{IC}/(\sigma_0 l_0)$ with n in Fig. 3.3, for $r_0 = 1.5e_x$ and $n \leq 0.071$ the ductile crack advance can be associated with void-by-void micromechanism whereas for all other cases ductile crack advance can be associated with multiple-void interaction micromechanism. [127] carried out simple but detailed analyses of growth of a row of explicitly modeled two-dimensional (cylindrical plane-strain) voids ahead of a blunting crack tip and showed that for low initial void volume fraction, voids grow one-by-one (starting from the void closest to the crack tip), whereas for high initial void volume fraction, many-voids ahead of the crack tip grow simultaneously. However, unlike the scenario modeled in [127], the material microstructure modeled

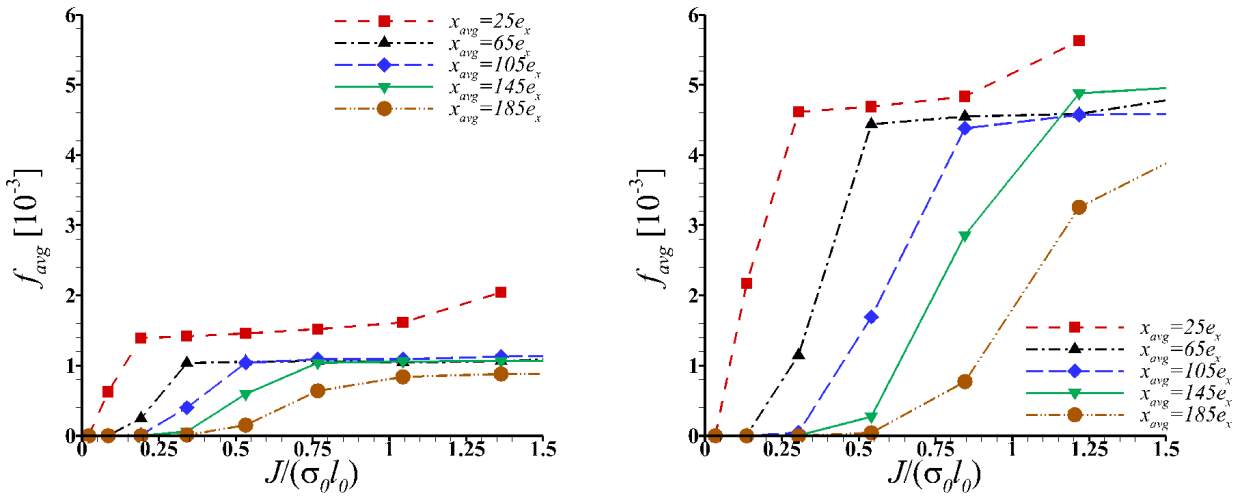

Figure 3.4: Evolution of average porosity, f_{avg}, in the bins located at distances x_{avg} directly ahead of the initial crack tip with applied normalized J, $J/\left(\sigma_0 l_0\right)$, for random distributions of inclusions of radius $r_0 = 1.5e_x$ and overall inclusion volume fractions, (a) $n = 0.024$ and (b) $n = 0.095$.

here has randomly distributed inclusions in a ductile material matrix. This prohibits the capability from applying the similar analysis as in [127] to identify or distinguish between the void-by-void and multiple-void interaction micromechanisms of ductile crack advance. Thus, analyzing the evolution of average porosity with the applied J in thin slices of the inclusion containing material volume ahead of the initial crack tip.

To this end, the uniform mesh region that contains three dimensional random distribution of inclusions (see Fig. 3.1) has been divided in to 20 cuboidal bins of height $60e_x$, thickness $50e_x$, and width $10e_x$. The average porosity, f_{avg}, in a bin is then estimated as,

$$f_{avg} = \sum_i \frac{V_i f_i}{V_{bin}} \tag{3.5}$$

where, i is the number of elements in the bin, V_i is the volume of element i, f_i is the average value of porosity in the element i and V_{bin} is the volume of the bin. The value of f_{avg} in a bin is estimated until the bin is crack free. The evolution of f_{avg} in the bins located at an average distance, x_{avg},

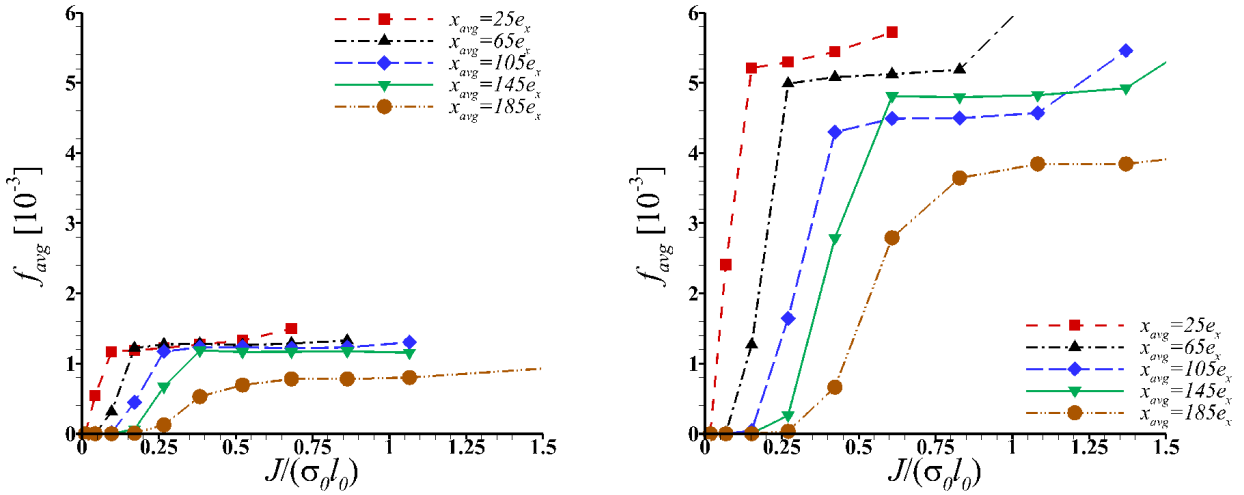

Figure 3.5: Evolution of average porosity, f_{avg}, in the bins located at distances x_{avg} directly ahead of the initial crack tip with applied normalized J, $J/\left(\sigma_0 l_0\right)$, for random distributions of inclusions of radius $r_0 = 3.0e_x$ and overall inclusion volume fractions, (a) $n = 0.024$ and (b) $n = 0.095$.

from the initial crack tip with applied normalized J, $J/\left(\sigma_0 l_0\right)$, for two inclusion volume fractions, $n = 0.024$ and 0.095, with $r_0 = 1.5e_x$ are shown in Fig. 3.4 and with $r_0 = 3e_x$ are shown in Fig. 3.5.

Based on the observations of [127], it would be expected that for $r_0 = 1.5e_x$ and $n = 0.024$, Fig. 3.4, the value of f_{avg} in the bins should evolve one-by-one (starting from the bin closest to the crack tip) and for all other cases shown in Figs. 3.4b, 3.5a and 3.5b, f_{avg} in many-bins ahead of the crack tip should evolve simultaneously with increasing $J/\left(\sigma_0 l_0\right)$. However, as shown in Figs. 3.4 and 3.5, for all the cases the value of $J/\left(\sigma_0 l_0\right)$ at which f_{avg} starts to evolve in a bin increases with increasing distance of the bin from the initial crack tip, suggesting f_{avg} in the bins evolve one-by-one. Also, for a given bin, the value of f_{avg} for all the cases initially increases rapidly with increasing $J/\left(\sigma_0 l_0\right)$ and then tends to increase rather slowly. There is, however, a clear difference between, Figs. 3.4a and 3.5a, and Figs. 3.4b and 3.5b, that suggests that the level of the f_{avg} versus $J/\left(\sigma_0 l_0\right)$ curve only depends on the inclusion volume fraction, n. The absence of a clear signature suggesting void-by-void or multiple-void interaction micromechanism of ductile

crack advance in the present analyses presented in Figs. 3.4 and 3.5, is likely due to the fact that the material microstructure in this work is characterized by randomly distributed inclusions in three-dimensional space for which the crack path is not fixed a priori.

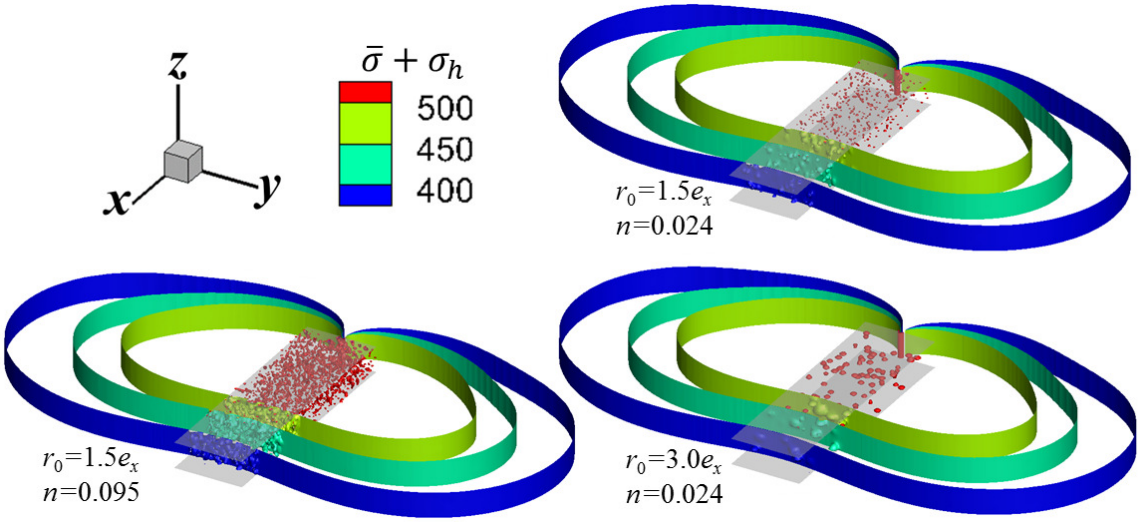

Figure 3.6: Isosurface plot of matrix flow strength, $\bar{\sigma}$, plus hydrostatic stress, σ_h, ahead of the initial crack tip together with active inclusions (inclusions that have already nucleated voids) at an applied normalized J, $J/(\sigma_0 l_0)$. The parameter $(\bar{\sigma} + \sigma_h)$ dictates the stress controlled nucleation of voids at the inclusion sites. For inclusions of radius $r_0 = 1.5e_x$ and overall inclusion volume fraction $n = 0.024$, $J/(\sigma_0 l_0) \approx 0.53$; for $r_0 = 1.5e_x$ and $n = 0.095$, $J/(\sigma_0 l_0) \approx 0.85$; and for $r_0 = 3.0e_x$ and $n = 0.024$, $J/(\sigma_0 l_0) \approx 0.27$.

The initial rapid increase in f_{avg} in a bin with increasing $J/(\sigma_0 l_0)$ seen in Figs. 3.4 and 3.5 arises from the stress controlled void nucleation at inclusions. In Fig. 3.6, isosurfaces of the matrix flow strength, $\bar{\sigma}$, plus the hydrostatic stress, σ_h, are plotted together with the active inclusions (inclusions that have already nucleated voids) for $r_0 = 1.5e_x$ with $n = 0.024$ and 0.095, and for $r_0 = 3.0e_x$ with $n = 0.024$. The parameter $\bar{\sigma} + \sigma_h$ is the driving force for void nucleation at the inclusions following the nucleation criteria in Eq. 2.10. For all the cases, the $\bar{\sigma} + \sigma_h$ isosurfaces in Fig. 3.6 are plotted at values of applied $J/(\sigma_0 l_0)$ that are less than the values of respective $J_{IC}/(\sigma_0 l_0)$. As seen in Fig. 3.6, at a fixed value of applied $J/(\sigma_0 l_0)$, the region ahead of the crack tip in which the inclusions are already active depends on the extent of $\bar{\sigma} + \sigma_h$ contours. Thus, for all

the cases, f_{avg} in the bins due to void nucleation evolves one-by-one as seen in Figs. 3.4 and 3.5. The calculations also show that once the inclusions have nucleated voids in a bin, only few voids within a bin are found to grow significantly. Crack advance then occurs by linking up the crack tip with the growing voids in the bin via strain induced void nucleation and growth in the matrix, as also seen in experiments [141]. This results in very little void growth off the crack plane as has been observed experimentally for a variety of ductile materials [142, 143]. This also explains why, once all the inclusions in a bin have been activated there is a very little increase in f_{avg} in that bin and the level of the $J/\left(\sigma_0 l_0\right)$ versus f_{avg} curve predominantly depend on the value of n. No inclusion size effect on void nucleation is modeled here but in line with experimental observations, for example [122, 125], an increase in J_{IC} with decreasing inclusion size for the same l_0 naturally emerges in the calculations.

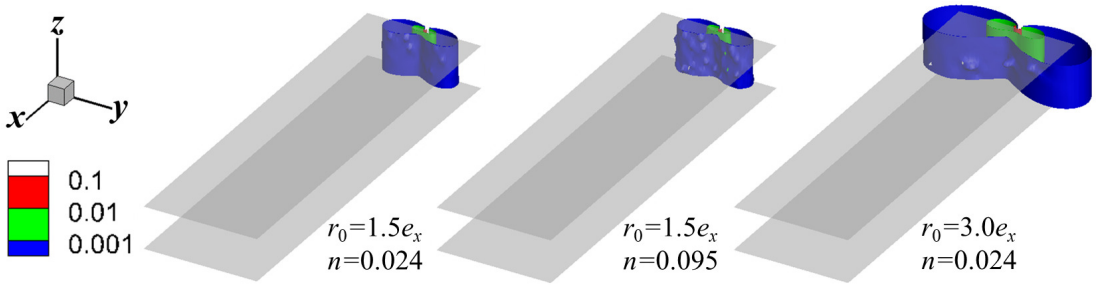

Figure 3.7: Isosurface plots of equivalent plastic strain ahead of the initial crack tip for random distributions of inclusions at an applied normalized J, $J/\left(\sigma_0 l_0\right)$. For inclusions of radius $r_0 = 1.5e_x$ and overall inclusion volume fraction $n = 0.024$, $J/\left(\sigma_0 l_0\right) \approx 0.09$; for $r_0 = 1.5e_x$ and $n = 0.095$, $J/\left(\sigma_0 l_0\right) \approx 0.14$; and for $r_0 = 3.0e_x$ and $n = 0.024$, $J/\left(\sigma_0 l_0\right) \approx 0.1$.

The variation of $J_{IC}/(\sigma_0 l_0)$ with n in Fig. 3.3, clearly suggest that the micromechanism of ductile crack advance for $r_0 = 1.5e_x$ and $n \leq 0.071$ differs from all other cases considered, even though it is not possible to identify these micromechanisms using analyses analogous to [127], Figs. 3.4 and 3.5. To further explore the micromechanisms of ductile crack advance, the isosurfaces of equivalent plastic strain ahead of the initial crack tip for $r_0 = 1.5e_x$ with $n = 0.024$ and 0.095, and for $r_0 = 3.0e_x$ with $n = 0.024$ at two values of applied $J/(\sigma_0 l_0)$ have been

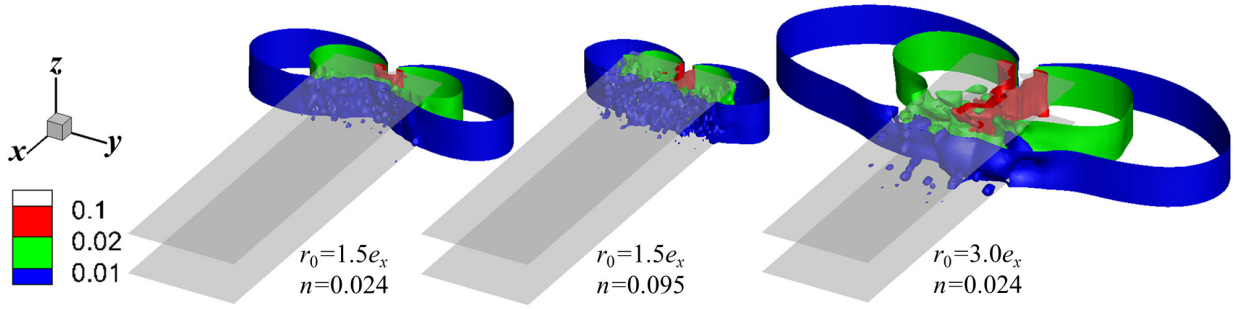

Figure 3.8: Isosurface plots of equivalent plastic strain ahead of the initial crack tip for random distributions of inclusions at an applied normalized J, $J/(\sigma_0 l_0)$. For inclusions of radius $r_0 = 1.5e_x$ and overall inclusion volume fraction $n = 0.024$, $J/(\sigma_0 l_0) \approx 1.04$; for $r_0 = 1.5e_x$ and $n = 0.095$, $J/(\sigma_0 l_0) \approx 1.22$; and for $r_0 = 3.0e_x$ and $n = 0.024$, $J/(\sigma_0 l_0) \approx 1.07$.

plotted in Figs. 3.7 and 3.8, respectively. In Fig. 3.7, the isosurfaces of equivalent plastic strain are plotted at values of applied $J/(\sigma_0 l_0)$ that are much less than the corresponding values of $J_{IC}/(\sigma_0 l_0)$ whereas in Fig. 3.8 the isosurfaces of equivalent plastic strain are plotted at values of applied $J/(\sigma_0 l_0)$ that are comparable to the corresponding values of $J_{IC}/(\sigma_0 l_0)$. As shown in Fig. 3.7, during the early stages of deformation the overall equivalent plastic strain distribution follows the expected pattern for plane strain Mode I loading with local perturbations due to stress controlled void nucleation at the inclusions. Following crack growth initiation for $r_0 = 1.5e_x$ with 0.095 and for $r_0 = 3.0e_x$ with $n = 0.024$, Fig. 3.8, plastic strain concentrates in a band. This shows that compared to the stress based void nucleation at inclusions, Fig. 3.6, the growth of nucleated voids and the plastic strain controlled secondary void nucleation in the material matrix are more sensitive to inclusion distribution. This is in line with the past experimental observations that have suggested that in ductile materials with increasing inclusions size or volume fraction final fracture occurs by microscopic plastic strain localization and secondary void nucleation between large voids [123, 135, 141, 144].

The overall mechanism of ductile crack advance for all the cases considered is same in a way that following the stress based void nucleation at the inclusions, it involves growth of a limited number of nucleated voids and coalescence of these voids via plastic strain controlled secondary void nucleation in the material matrix. Nevertheless, the results show that there is an increase in

the propensity of plastic strain localization with increasing inclusion volume fraction and/or size. This subtle change in the micromechanism of ductile crack advance results in the difference on the dependence of macroscopic fracture toughness on the material microstructure. So that for relatively low inclusion volume fraction and small inclusion size the normalized fracture toughness $J_{IC}/(\sigma_0 l_0)$ depends on both the inclusion size and the overall microstructural parameter i.e. inclusion volume fraction while for high inclusion volume fraction and large inclusion size $J_{IC}/(\sigma_0 l_0)$ depends only on the inclusion size. Furthermore, these results provide important guidelines for microstructural engineering to increase ductile fracture toughness, for example, the results show that for a material with small inclusions, increasing the mean inclusion spacing has a greater effect on fracture toughness than for a material with large inclusions.

3.3.3 Influence of matrix material properties

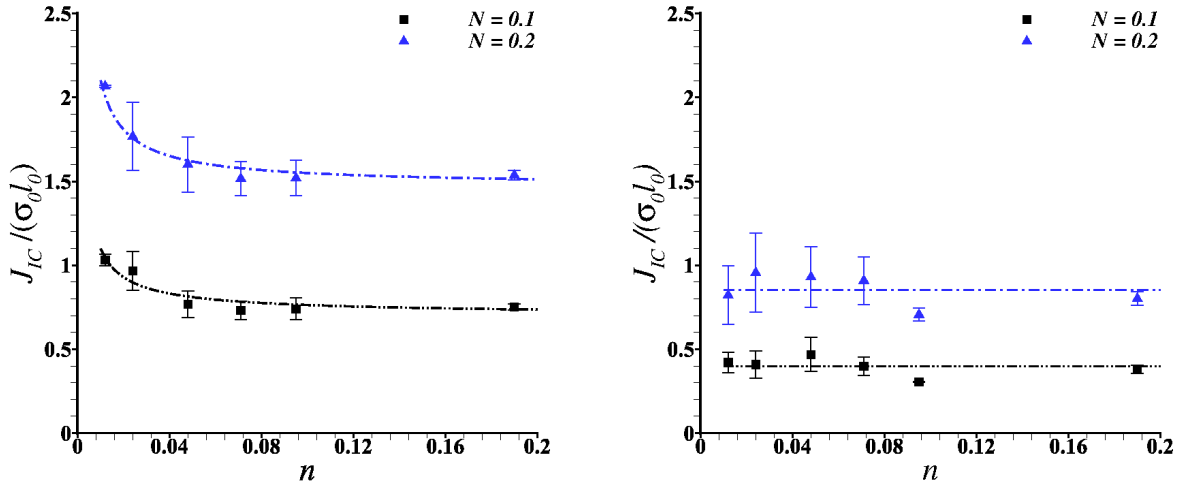

Figure 3.9: The effect of strain hardening exponent, N, on the variation of normalized fracture toughness, J_{IC}, $J_{IC}/(\sigma_0 l_0)$, with inclusion volume fraction, n, for inclusion radii, (a) $r_0 = 1.5e_x$ and (b) $r_0 = 4.5e_x$.

In this section, the influence of key matrix material parameters on the micromechanisms of

ductile crack advance and macroscopic fracture toughness of the material have been presented. The matrix material parameters that are considered, are the matrix strain hardening exponent, N in Eq. (2.7), the mean equivalent plastic strain to void nucleation in the matrix, ϵ_N in Eq. (2.9), and the critical void volume fraction to void coalescence, f_c in Eq. (2.4).

The effect of the matrix strain hardening exponent, N, on the variation of normalized fracture toughness, $J_{IC}/\left(\sigma_0 l_0\right)$, with inclusion volume fraction, n, for inclusion radii, $r_0 = 1.5e_x$ and $4.5e_x$, are shown in Fig. 3.9. As shown in the figure, decreasing the value of N results in a decrease in the value of $J_{IC}/\left(\sigma_0 l_0\right)$ for all values of r_0 and n considered, with the effect of N being more pronounced for $r_0 = 1.5e_x$ than for $r_0 = 4.5e_x$. For the smallest inclusion radius, $r_0 = 1.5e_x$, the value of $J_{IC}/\left(\sigma_0 l_0\right)$ initially decreases with increasing n and then tends to saturate, whereas for $r_0 = 4.5e_x$ the value of $J_{IC}/\left(\sigma_0 l_0\right)$ is independent of the value of n for both the values of $N = 0.1$ and 0.2. The dashed-dot lines in Fig. 3.9a show a fit to $J_{IC}/(\sigma_0 l_0) = C_1 n^{C_2} + C_3$ and in Fig. 3.9b show a fit to $J_{IC}/(\sigma_0 l_0) = C_4$. In Fig. 3.9a, for $r_0 = 1.5e_x$, $C_1 = 0.01$ for both $N = 0.1$ and 0.2, for $N = 0.1$, $C_2 = -0.8$ and $C_3 = 0.7$, and for $N = 0.2$, $C_2 = -0.9$ and $C_3 = 1.47$. In Fig. 3.9b, for $r_0 = 4.5e_x$, $C_4 \approx 0.4$ and 0.9 for $N = 0.1$ and 0.2, respectively. The values of the fitting parameter C_2 for $N = 0.1$ and 0.2 for $r_0 = 1.5e_x$ shows that the dependence of $J_{IC}/\left(\sigma_0 l_0\right)$ on n decreases with decreasing strain hardening exponent. The decrease in the dependence of $J_{IC}/\left(\sigma_0 l_0\right)$ on n with decreasing N observed in the calculations is consistent with experimental observations [145]. [145] analyzed the influence of initial porosity on the ductility of commercial pure (CP) titanium (Ti) and Ti-6Al-4V alloy. They showed that the dependence of ductility on the initial volume fraction of porosity is greater for CP Ti for which $N \approx 0.19$ than the Ti-6Al-4V alloy for which $N \approx 0.08$.

Next, focusing on the effect of mean equivalent plastic strain to void nucleation, ϵ_N, on the variation of $J_{IC}/\left(\sigma_0 l_0\right)$ with n and r_0, Fig. 3.10. The parameter ϵ_N dictates the secondary void nucleation in the material matrix. As shown in the figure, decreasing the value of ϵ_N results in a decrease in the value of $J_{IC}/\left(\sigma_0 l_0\right)$ for all values of r_0 and n considered. A decrease in fracture toughness of the material with increasing susceptibility to secondary void nucleation is consistent

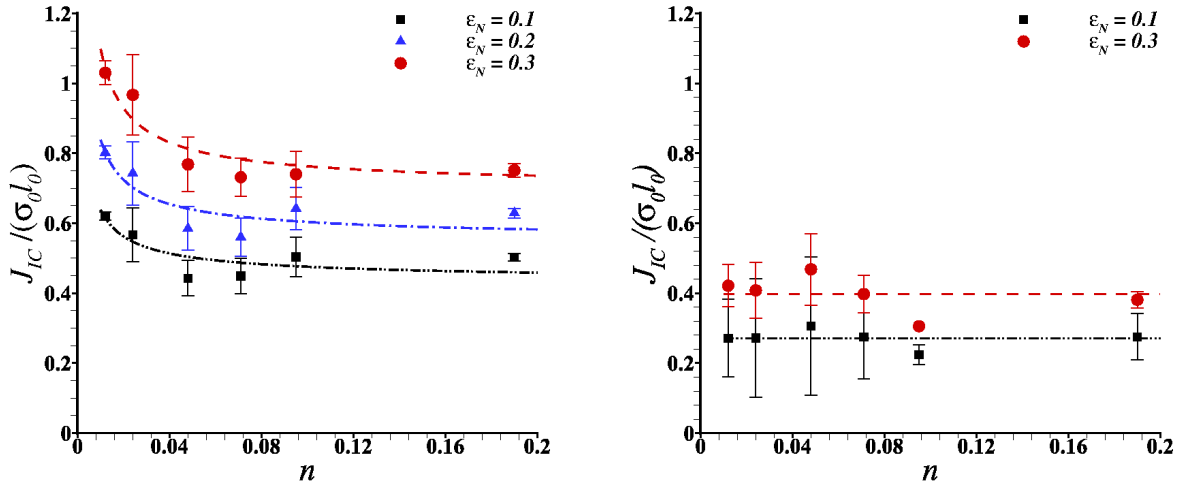

Figure 3.10: The effect of mean equivalent plastic strain to void nucleation in the matrix material, ϵ_N, on the variation of normalized fracture toughness, J_{IC}, $J_{IC}/(\sigma_0 l_0)$, with inclusion volume fraction, n, for inclusion radii, (a) $r_0 = 1.5e_x$ and (b) $r_0 = 4.5e_x$.

with previous works [128, 146, 147]. Similar to the effect of N, here as well, Fig. 3.10, the effect of ϵ_N is more pronounced for $r_0 = 1.5e_x$ than for $r_0 = 4.5e_x$, and for $r_0 = 1.5e_x$ the value of $J_{IC}/(\sigma_0 l_0)$ initially decreases with increasing n and then tends to saturate whereas for $r_0 = 4.5e_x$ the value of $J_{IC}/(\sigma_0 l_0)$ is independent of the value of n for all the values of ϵ_N considered. The dashed-dot lines in Fig. 3.10a show a fit to $J_{IC}/(\sigma_0 l_0) = C_1 n^{C_2} + C_3$ and in Fig. 3.10b show a fit to $J_{IC}/(\sigma_0 l_0) = C_4$. In Fig. 3.10a, for $r_0 = 1.5e_x$, $C_1 = 0.01$ for both $\epsilon_N = 0.1$ and 0.3, for $\epsilon_N = 0.1$, $C_2 = -0.66$ and $C_3 = 0.43$, and for $\epsilon_N = 0.3$, $C_2 = -0.8$ and $C_3 = 0.7$. In Fig. 3.10b, for $r_0 = 4.5e_x$, $C_4 \approx 0.3$ and 0.4 for $\epsilon_N = 0.1$ and 0.3, respectively. The values of the fitting parameter C_2 for $\epsilon_N = 0.1$ and 0.3 for $r_0 = 1.5e_x$ shows that the dependence of $J_{IC}/(\sigma_0 l_0)$ on n decreases with decrease in the value of ϵ_N or increasing susceptibility to secondary void nucleation.

Figure 3.11 shows the effect of the critical void volume fraction to void coalescence, f_c, on the variation of $J_{IC}/(\sigma_0 l_0)$ with n and r_0. The parameter f_c dictates the energy dissipated in the growth of the nucleated voids prior to crack advance. As shown in the figure, decreasing f_c results in a decrease in the value of $J_{IC}/(\sigma_0 l_0)$ for all values of r_0 and n considered. The effect

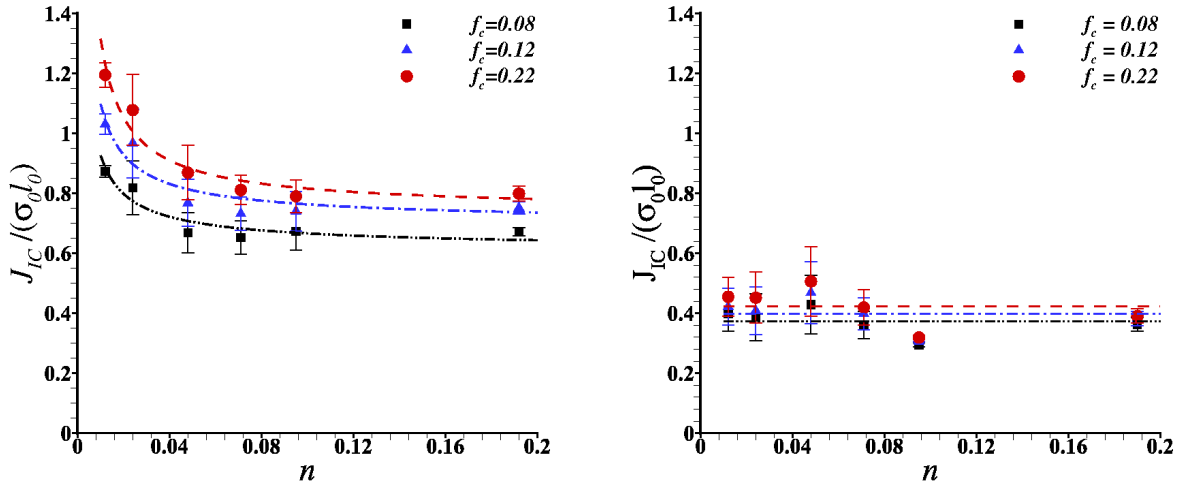

(a) (b)

Figure 3.11: The effect of critical volume fraction to void coalescence, f_c, on the variation of normalized fracture toughness, J_{IC}, $J_{IC}/(\sigma_0 l_0)$, with inclusion volume fraction, n, for inclusion radii, (a) $r_0 = 1.5e_x$ and (b) $r_0 = 4.5e_x$.

of f_c on fracture toughness that emerges in the calculations is consistent with the experimentally observed correlation between the radius of the cavities at failure and the fracture toughness of the material [124]. Also, similar to the results shown in Figs. 3.9 and 3.10, here as well, Fig. 3.11, the effect of f_c is more pronounced for $r_0 = 1.5e_x$ than for $r_0 = 4.5e_x$, and for $r_0 = 1.5e_x$ the value of $J_{IC}/(\sigma_0 l_0)$ initially decreases with increasing n and then tends to saturate whereas for $r_0 = 4.5e_x$ the value of $J_{IC}/(\sigma_0 l_0)$ is independent of the value of n for all the values of f_c considered. The dashed-dot lines in Fig. 3.11a show a fit to $J_{IC}/(\sigma_0 l_0) = C_1 n^{C_2} + C_3$ and in Fig. 3.11b show a fit to $J_{IC}/(\sigma_0 l_0) = C_4$. In Fig. 3.11a, for $r_0 = 1.5e_x$, $C_1 = 0.01$ for both $f_c = 0.08$ and 0.22, for $f_c = 0.08$, $C_2 = -0.75$ and $C_3 = 0.61$, and for $f_c = 0.22$, $C_2 = -0.88$ and $C_3 = 0.74$. In Fig. 3.11b, for $r_0 = 4.5e_x$, $C_4 \approx 0.37$ and 0.42 for $f_c = 0.08$ and 0.22, respectively. The values of the fitting parameter C_2 for $f_c = 0.08$ and 0.22 for $r_0 = 1.5e_x$ shows that the dependence of $J_{IC}/(\sigma_0 l_0)$ on n decreases with decreasing value of the critical void volume fraction to void coalescence, f_c.

To summarize, the ductile fracture toughness of the material decreases with, decreasing strain

hardening exponent of the matrix material (decreasing N), increasing susceptibility to secondary void nucleation in the matrix material (decreasing ϵ_N) and decreasing energy dissipation in the growth of the nucleated voids prior to crack advance (decreasing f_c). Furthermore, for the range of the values of N, ϵ_N and f_c considered, (i) the effect of these material parameters on fracture toughness is more pronounced for small inclusions than for large inclusions, and (ii) for small inclusions, the dependence of $J_{IC}/\left(\sigma_0 l_0\right)$ on inclusion volume fraction, n, decreases with decrease in the value of these material parameters, whereas for large inclusions the value of $J_{IC}/\left(\sigma_0 l_0\right)$ is always independent of the value of n. These observations are consistent with the discussion of micromechanisms of ductile crack advance presented in Section 3.3.2. As discussed in Section 3.3.2, the propensity of plastic strain localization increases with increasing inclusion size. Thus, for material microstructures with large inclusions, the damage induced softening due to inclusions is sufficient to cause plastic strain localization and decreasing the strain hardening exponent, increasing the susceptibility to secondary void nucleation or decreasing the energy dissipated in void growth just accelerates the localization process to various extents. Also, the dependence of $J_{IC}/\left(\sigma_0 l_0\right)$ on inclusion volume fraction decreases with increasing propensity of plastic strain localization. For material microstructures with small inclusions, the damage induced softening due to inclusions is not sufficient to cause plastic strain localization but a decrease in the strain hardening exponent, increase in the susceptibility to secondary void nucleation or decrease in the energy dissipated in void growth increases the propensity of plastic strain localization.

3.4 Conclusions

Finite element finite deformation calculations to correlate the macroscopic fracture toughness with the fracture mechanisms operating at the microscale for ductile material matrix with three-dimensional distribution of inclusions have been carried out in the study. While the study has not aimed at modeling any particular real material, several features of crack growth behavior and dependence of fracture toughness on microstructural parameters such as, volume fraction, size and spacing of inclusions, and matrix material properties such as, strain hardening exponent, susceptibility to secondary void nucleation and energy dissipated in the growth of the nucleated voids,

observed in experiments, naturally emerge in the calculations. The extent to which the microstructural parameters and matrix material properties affect the micromechanisms of ductile crack advance and the macroscopic fracture toughness of the material were illustrated.

The key conclusions are as follows:

1. For material microstructures consisting of a ductile matrix with three-dimensional (random) distribution of void nucleating inclusions, it is not possible to identify or distinguish between the void-by-void and the multiple-void interaction micromechanisms of ductile crack advance.

2. Results show that there is an increase in the propensity of plastic strain localization with increasing inclusion volume fraction and/or inclusion size.

3. Due to the increase in the propensity of plastic strain localization for high inclusion volume fraction and large inclusion size, $J_{IC}/(\sigma_0 l_0)$ only depends on the inclusion size while for relatively low inclusion volume fraction and small inclusion size, $J_{IC}/(\sigma_0 l_0)$ depends on both the inclusion size and the overall microstructural parameter i.e. inclusion volume fraction.

4. The dependence of $J_{IC}/\left(\sigma_0 l_0\right)$ on the inclusion volume fraction for small inclusions decreases with decreasing strain hardening exponent of the matrix material, increasing susceptibility of secondary void nucleation and decreasing energy dissipation in the growth of nucleated voids prior to ductile crack advance.

5. The results presented provide guidelines for microstructural engineering to increase ductile fracture toughness, for example, the results show that for a material with small inclusions, increasing the mean inclusion spacing has a greater effect on fracture toughness than for a material with large inclusions.

4. DUCTILE FRACTURE OF DUAL-PHASE STEELS UNDER BENDING*

4.1 Background

The performance, safety, reliability and manufacturability of a variety of engineering components and structures are limited by ductile fracture. At room temperature, ductile fracture of engineering metals and alloys involves nucleation, growth and coalescence of microscale voids [99]. This phenomenon is affected by the interlacing of length-scales induced by the geometry of deformation, local boundary conditions and/or heterogeneous microstructure of the material. These length-scales in turn interact and evolve. For instance, the deformation fields induced by geometry or boundary conditions can produce substantial microstructural modifications resulting in often unknown and counterintuitive subsequent fracture process. The objective of this work is to model the effect of length-scales induced by the geometry of deformation, in particular bending, and the material microstructure on ductile fracture of dual-phase (DP) advanced high strength steel (AHSS) sheets.

DP steel sheets with yield and tensile strengths in excess of 300MPa and 600MPa, respectively, are one of the most widely sought after AHSS for automotive applications [23] where safety, vehicle weight reduction and emission reduction are of paramount importance [15, 27]. DP steels were introduced in the mid-1970s [148] and since then have experienced the fastest growth in the automotive industry [27]. These are produced on continuous annealing lines that allow intercritical heating into the ferrite-austenite phase field followed by rapid cooling to cause diffusionless austenite to martensite transformation [148]. The final microstructure of DP steels primarily consists of hard martensite islands dispersed in a soft ferrite phase matrix. The presence of two elastic-plastic phases with contrasting strength and strain hardenability gives rise to complex deformation behavior, especially for DP steels with high martensite content and tensile strength of order 1GPa.

While the influence of microstructure on the deformation and fracture behavior of DP steel

*Reprinted with permission from "Ductile fracture of dual-phase steel sheets under bending" by **Liu, Y.**, Fan, D., Bhat, S.P. and Srivastava, A., 2020. *International Journal of Plasticity*, 125, pp.80-96, Copyright 2020 by Elsevier.

sheets under tensile loading conditions have been a topic of numerous experimental or computational studies, for example, [2,48,63,64,66–68,71,75–78,80,148–161], the role of DP microstructure on complex loading conditions have received far less attention [162–166]. The studies on the microstructural influence on deformation and fracture behavior of DP steels under simplified loading conditions, however, have provided several insights. The tensile stress-strain curve for DP steels with high martensite content has been found to exhibit three characteristic stages [165]. At low stresses, the response is elastic and with increasing stress levels the DP microstructure first reaches yield in the ferrite phase. Following initial yield, a period of steep strain-hardening is observed. In this regime, the martensite remains elastic while ferrite contributes 100% of the plastic strain. This stage continues until martensite reaches yield. At this point, there is a significant reduction in the strain-hardening rate, and both ferrite and martensite continue to deform plastically. The studies pertaining to damage nucleation and evolution in the DP microstructure suggest that the volume fraction, morphology and distribution of martensite, and the contrast between the properties of ferrite and martensite phases have a significant influence on damage accumulation. The state-of-the-art also suggests that the damage (or void) nucleation in DP steels occurs by mechanisms such as, decohesion at the ferrite/martensite interface, separation of adjacent martensite particles, and/or separation of fractured martensite particles.

The primary benefit of using DP AHSS in automotive body and structural parts is to enhance vehicles' crash resistance while reducing its overall weight. Steels are not inherently light weight material but vehicle weight reduction can be achieved by using AHSS with high density-normalized strength. DP steels with tensile strength of order 1GPa and above are one of the targeted structural material for such applications. However, as the strength of DP steel increases, the steel becomes less formable and more prone to ductile fracture under bending dominated manufacturing processes at room temperature [167]. In addition, DP steel sheets exhibit contrasting deformation and fracture anisotropy along the rolling direction (RD) and the transverse direction (TD) of the sheet under uniaxial tensile loading versus bending. Under uniaxial tension, DP steel sheets exhibit very similar stress-strain response along RD and TD up to the ultimate tensile strength with

ductility along RD being either equal to or greater than along TD [2, 80]. But under bending, the bendability of the sheet specimens with bend axis parallel to RD is less than the bendability of the sheet specimens with bend axis parallel to TD [3]. This clearly shows that there is a difference between the characterization of fracture in an imposed deformation field that is more or less uniform and the characterization of fracture in a heterogeneous field such as those observed in bending. In the former, a continuum description of fracture, can in principle be based on unstructured material parameters such as strength, strain hardening exponent, and volume fraction of the phases. On the other hand, in the latter, the fracture characterization must involve the interaction of length-scales induced by bending and the DP microstructure.

Several attempts have been directed towards modeling ductile fracture of DP steels. These approaches can be divided in to two categories: phenomenological fracture modeling [61–65] and microstructure-based fracture modeling [48, 66–79]. In phenomenological fracture models, a damage evolution equation is directly fit to macroscopic experimental data without a direct microstructure-fracture correlation. On the other hand, microstructure-based fracture modeling have been largely focused on 2D or 3D representative volume elements of the DP microstructures under idealized periodic boundary conditions. No effort has been made to model ductile fracture in DP steels under more realistic loading conditions in order to understand the interaction of length-scales originating from the geometry/boundary conditions, and material microstructure. Modeling fracture of DP steels under realistic boundary conditions is especially challenging because a loss of stress carrying capacity in the reinforcing phase due to void nucleation greatly affects the overall strain hardening response of the material. This leads to a breakdown in scale separation [53], making it very challenging to mathematically represent the material by an "effective homogenized media."

Here, microstructure-based finite element modeling to understand the influence of material microstructure on ductile crack nucleation and early stage ductile crack growth in DP steel sheets subjected to 90° V-bend loading conditions were carried out. In the calculations, the microstructural features, ferrite and martensite phases, of the DP steel in a small area (but large enough to

capture the nucleation and coalescence of micro-cracks) near the free surface of a thin slice of the bend specimen normal to the bend axis were discretely model . Both the ferrite and the martensite phases are modeled using a constitutive relation for progressively cavitating elastic-viscoplastic solid. For the microstructure-based modeling, several 2D SEM (Scanning Electron Microscope) images taken from the RD and TD cross-sections of an industrially produced galvannealed DP1000 steel sheet are first digitized. The digitized microstructure is then superimposed on the finite element grid and respective material properties are assigned based on integration points rather than finite elements as in [1,29]. This allows to smoothly resolve the interphase boundaries without any numerical complexities. Additionally, discretely modeling the microstructural features induces microstructural length-scale(s) [1,29,47,91]. The effect of length-scales induced by the geometry of deformation i.e. bending, and the material microstructure on ductile fracture of DP steel sheets are discussed. Parametric studies are also carried out to explore the effect of material parameters that dictate the propensity of void nucleation, energy dissipated in the growth of the nucleated voids prior to crack nucleation, and initial void volume fraction on ductile fracture of DP steel sheets under bending.

4.2 Problem formulation

Microstructure-based finite element modeling of deformation and fracture of DP steel sheets subjected to 90° V-bend loading conditions are carried out for a thin slice of material with dimensions, $L = 16mm$ (along x-axis), $d = 1.6mm$ (along y-axis) and $W = 0.01mm$ (along z-axis), as shown schematically in Fig. 6.8. The tip radius of the 90° V-bend punch is taken to be $0.1mm$. The finite element mesh consists of $22,920$ twenty node brick elements giving $161,973$ nodes. For the finite element mesh a single element through the width, W (along z-axis), of the specimen is used. A very fine uniform in-plane ($x-y$ plane) mesh is used in a $1.6mm \times 0.8mm$ region (marked as $abcd$ in Fig. 6.8) near the free surface of the bend specimen with in-plane element dimension $10\mu m \times 10\mu m$. The element dimension in the fine mesh region, $e = 10\mu m$, serves as a normalization length-scale.

The finite element calculations are carried out using in-house data parallel finite element code

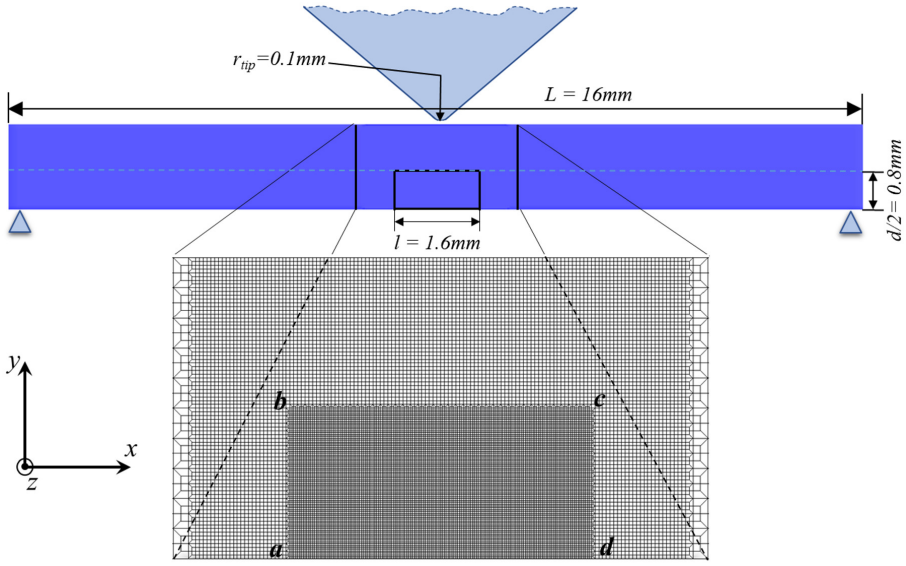

Figure 4.1: (top) A schematic of the bend specimen together with imposed constraint and loading conditions. (bottom) A zoomed view of the finite element mesh near the free surface of the bend specimen.

as in [1, 29, 47, 91, 168]. The finite element code is based on the dynamic principle of virtual work using a finite deformation Lagrangian convected coordinate formulation. The displacement and velocity boundary conditions imposed on the region analyzed follows the configuration shown schematically in Fig. 6.8. The y-displacement of the specimen is constraint at locations, $y = 0$, $x = -7.5mm$ and $y = 0$, $x = 7.5mm$ in the reference configuration. Overall plane strain conditions are imposed on $z = 0$ and $z = W$ surfaces of the bend specimen. The tip of the 90° V-bend punch is initially in contact with the bend specimen at $y = 1.6mm$ and $x = 0$. Although, calculations are based on the dynamic principle of virtual work for numerical convenience, the focus is on quasi-static response, hence to minimize the wave effects a time varying velocity, $V_y(t)$, in the negative y direction is applied to the tip of the punch that follows the relation:

$$V_y(t) = \begin{cases} V_y^0 t/t_r & \text{if} \quad t \leq t_r \\ V_y^0 & \text{if} \quad t > t_r \end{cases} \tag{4.1}$$

where, t is the analysis time, t_r is the rise time and V_y^0 is the final velocity of the punch for

Table 4.1: Average size of ferrite and martensite phases along x (specimen length) and y (specimen depth) axes in RD and TD cross-sections of the DP steel under consideration. The values in the units of μm are for the 'real' microstructure while the values in the units of e (normalization length-scale) are for the microstructure 'modeled'.

Orientation	Phase	Along x-axis	Along y-axis	Aspect ratio
RD	Ferrite	$2.09\mu m$ $(4.18e)$	$1.75\mu m$ $(3.5e)$	≈ 1.19
	Martensite	$1.76\mu m$ $(3.52e)$	$1.52\mu m$ $(3.04e)$	≈ 1.15
TD	Ferrite	$1.98\mu m$ $(3.96e)$	$1.63\mu m$ $(3.26e)$	≈ 1.21
	Martensite	$1.72\mu m$ $(3.44e)$	$1.49\mu m$ $(2.98e)$	≈ 1.15

$t > t_r$. In the calculations, $t_r = 1.0 \times 10^{-4}s$ and $V_y^0 = 3.0 \times 10^3 mm/s$ (along the negative y direction) is used. As the deformation proceeds i.e. the tip of the punch moves in the negative y direction, additional nodes on the top surface of the specimen comes in contact with the 90° V-bend punch. These additional nodes are assigned the value of V_y which is equal to the velocity of the tip of the punch at the time of contact. Also, to all the nodes that are in contact with the punch, zero velocity along x direction, $V_x = 0$, is imposed. This corresponds to perfect sticking of the material to the punch.

As in [1, 29, 47, 91], eight point Gaussian integration is used in each twenty-node element for integrating the internal force contributions and twenty-seven point Gaussian integration is used for the element mass matrix. Lumped masses are used so that the mass matrix is diagonal. The discretized equations are integrated using the explicit Newmark β-method with $\beta = 0$ [93]. The constitutive updating is based on the rate tangent modulus method proposed in [94], while material failure is implemented via the element vanishing technique proposed in [90].

4.2.1 Microstructure modeling

Microstructure-based finite element modeling of DP steel sheets under realistic boundary conditions requires modeling the entire specimen and the microstructure within. In theory, it is possible to carry out microstructure-based finite element modeling of an entire specimen with all of its microstructural details. However, the mesh density required to discretely model micron-size

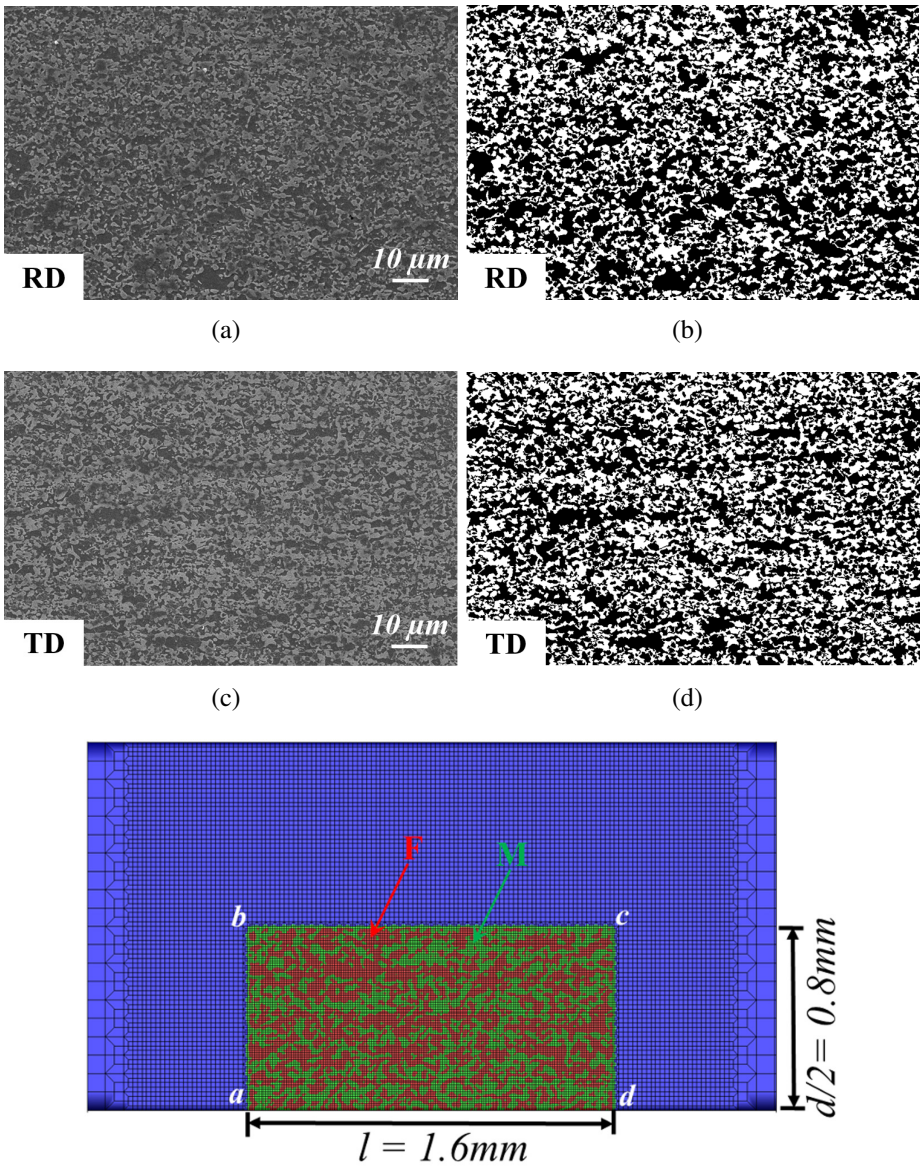

Figure 4.2: (a) A representative (secondary electron) SEM image and (b) its binary version of the microstructure taken from the rolling direction (RD) cross-section of the DP steel under consideration. (c) A representative SEM image and (d) its binary version of the microstructure taken from the transverse direction (TD) cross-section of the DP steel under consideration. (e) A zoomed view of the finite element mesh near the free surface of the bend specimen showing the discretely modeled, ferrite (F) and martensite (M), phases of the DP steel microstructure in the region marked as $abcd$.

microstructural features in a bending specimen of dimensions in centimeters would make the finite element calculations prohibitively time consuming. Hence, the material microstructure in a small area but large enough to capture nucleation and coalescence of micro-cracks near the free surface of the specimen, as shown in Fig. 4.2, has been discretely modeled. To this end, secondary electron SEM images of chemically etched metallographic specimens of a DP1000 steel sheet are digitized via Marker-Controlled Watershed Segmentation method [169] as shown in Figs. 4.2(a)-(b) and (c)-(d). The Marker-Controlled Watershed Segmentation method is used in lieu of Image thresholding because of the limited contrast between the constituent phases of the DP steel in an SEM image. The basic procedure of Marker-Controlled Watershed Segmentation method involves, computing a segmentation function, computing foreground and background markers, modifying the segmentation function so that it only has minima at the foreground and background marker locations, and finally computing the watershed transform of the modified segmentation function. All these steps can be carried out using the built-in Image Processing Toolbox™ in MATLAB [169]. Next, the SEM image is magnified by $20X$ to 'artificially' increase the feature sizes to allow to choose a reasonable mesh size to resolve the details of the microstructure. The $20X$ magnification increases an actual length of $1\mu m$ to $20\mu m$ (or in terms of the normalization length-scale, e, it is simply $2e$) while keeping the overall volume fraction of the phases fixed. The digitized and magnified microstructures are then superimposed on the mesh in the region marked as $abcd$ in Figs. 6.8 and 4.2(e), and material properties corresponding to respective microstructural features are assigned based on material (Gaussian) integration points rather than finite elements. Discretizing material microstructure based on integration points allows to smoothly resolve the interphase boundaries as shown in Fig. 4.2(e). The region outside $abcd$ in the bend specimen are assigned material properties corresponding to the overall (homogenized) mechanical response of the DP steel under consideration.

In this work, the microstructure of the DP steel in both RD and TD cross-sections, Figs. 4.2(a)-(b) and (c)-(d) respectively, are considered. The average size of ferrite and martensite phases along x (specimen length) and y (specimen depth) axes in the RD and TD cross-sections are given in Ta-

ble 4.1. In the DP steel under consideration, on average, the aspect ratio of the martensite phase in both RD and TD cross-sections are roughly the same. The average aspect ratio of the ferrite phase, however, is slightly greater in the TD cross-section as compared to the RD cross-section. Hereafter, RD (TD) refers to bend specimens with bending axis parallel to the RD (TD) of the DP steel sheet or the microstructure modeled in the region $abcd$, Figs. 4.2(e), is the microstructure corresponding to the RD (TD) cross-section. For both RD and TD bend specimens five microstructures taken from five locations on the respective cross-sections of the DP sheet steel under consideration have been analyzed.

4.2.2 Constitutive parameter identification

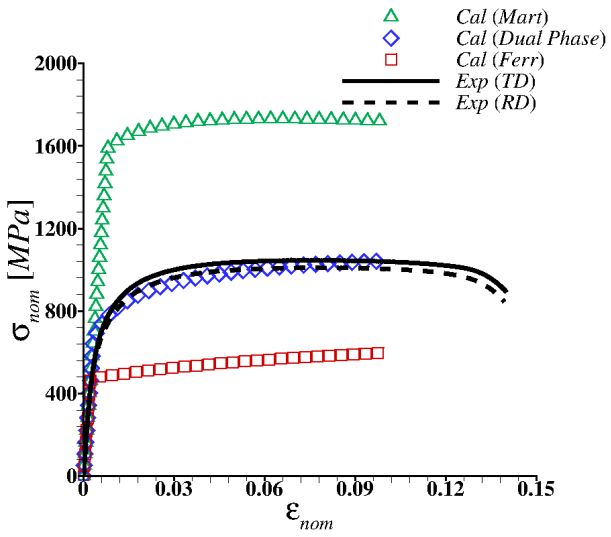

Figure 4.3: Comparison of uniaxial tensile nominal stress (σ_{nom}) - strain (ε_{nom}) response of the DP steel sheet obtained from uniaxial tensile tests with tensile axis parallel to rolling direction, $Exp(RD)$, and transverse direction, $Exp(TD)$, and finite element calculation using the calibrated constitutive relation, Eq. (2.7), for fully dense ($f = 0$ throughout the deformation) homogenized DP steel sheet, $Cal(DualPhase)$. The extracted uniaxial tensile, σ_{nom} - ε_{nom}, curves of fully dense ferrite, $Cal(Ferr)$, and martensite, $Cal(Mart)$, phases present in the DP steel under consideration are also shown in the figure.

The constitutive framework described in Section 2.2 contains several constitutive (material)

parameters. The values of these parameters must be determined for the overall DP microstructure as well as for the individual constituent phases, ferrite and martensite, in order to carry out microstructure-based finite element modeling. To determine the values of the constitutive parameters that best represent the overall stress-strain response of the fully dense ($f = 0$ throughout the deformation) DP steel sheet, firstly, the values of Young's modulus, E, Poisson's ratio, ν, and strain rate sensitivity exponent, m have been fixed. The value of m is fixed following the work of [165]. The values of the remaining constitutive parameters, initial flow strength, σ_0, strain hardening exponent, N, reference strain, ε_0, and reference strain rate, $\dot{\varepsilon}_0$, are then directly obtained using the portion of the experimental stress-strain curve before the onset of necking. The values of all the constitutive parameters that best represent the overall stress-strain response of the fully dense DP steel under consideration are tabulated in Table 5.1. A comparison of uniaxial tensile nominal stress - strain response of the industrially produced galvannealed DP1000 sheet steel under consideration and finite element calculation using the constitutive parameter given in Table 5.1 for fully dense DP steel sheet before the onset of necking is shown in Fig. 4.3.

Next, focusing on determining the values of the constitutive parameters for the fully dense ($f = 0$ throughout the deformation) constituent phases, ferrite and martensite. To this end, a 3D representative volume element (RVE) of the DP microstructure using the procedure described in [48, 170] has been constructed. The DP steel sheet considered in this work contains $\approx 54\%$ ferrite and $\approx 46\%$ martensite phase by volume. The values of the constitutive parameters, E, ν, and m are fixed a priori for both phases. The value of σ_0 for the ferrite phase is also fixed a priori based on prior experience [165, 171]. In addition, the range (upper and lower bound) of the values of N for the martensite phase is chosen to represent negligible strain hardening in the martensite phase based on prior experience. Following this, an iterative optimization procedure was used to determine the values of the constitutive parameters, N, ε_0, and $\dot{\varepsilon}_0$ for the ferrite phase and σ_0, N, ε_0, and $\dot{\varepsilon}_0$ for the martensite phase, that minimizes the mean squared error between the uniaxial stress-strain response of the RVE and prediction using the constitutive parameter given in Table 5.1 for fully dense DP steel. The iterative optimization scheme was implemented as a MATLAB function.

The MATLAB function carries out the finite element calculations of uniaxial tensile test of the RVE; calculates the average mean squared error of the difference between predicted and target stress-strain data; and minimizes the error by adjusting the values of the constitutive parameters following the Nelder-Mead simplex algorithm. The values of all the constitutive parameters for both constituent phases are tabulated in Table 5.1, and the uniaxial nominal stress-strain response of the two fully dense constituent phases obtained using these parameters are shown in Fig. 4.3.

Table 4.2: The values of the constitutive parameters for the overall (homogenized) DP steel, and for the individual constituent phases, ferrite and martensite, present in the DP microstructure under consideration.

Parameters	**Dual Phase**	**Ferrite**	**Martensite**
Young's modulus, $E(Gpa)$	200	200	200
Poisson's ratio, ν	0.3	0.3	0.3
Initial flow strength, $\sigma_0(MPa)$	610	430	1450
Strain hardening exponent, N	0.14	0.35	0.06
Reference strain, ε_0	0.00175	0.06	0.006
Strain rate sensitivity exponent, m	0.01	0.01	0.01
Reference strain rate, $\dot{\varepsilon}_0(\mathrm{s}^{-1})$	0.1	0.01	0.01

Apart from the constitutive parameters needed to model the mechanical response of the fully dense material that are given in Table 5.1, the constitutive framework detailed in Section 2.2 also contains parameters associated with the modified Gurson model. These parameters are, initial porosity, f_0, critical void volume fraction to void coalescence, f_c, and the three parameters, f_N^{ε}, s_N^{ε} and ε_N associated with the void nucleation criteria in Eq. (2.9). Note, damage is only considered to take place in the region marked $abcd$ in Fig. 6.8 or Fig. 4.2(e) where the constituent phases, ferrite and martensite, of the DP steel are discretely modeled. So that the constitutive parameters corresponding to the modified Gurson model are only needed for the ferrite and martensite phase

and not for the overall (homogenized) DP steel. Following the work of [48], $f_0 = 0$ in the ferrite phase and $f_0 = 0.002$ in the martensite phase have been taken. The values of the other four parameters, $f_c = 0.1$, $f_N^{\varepsilon} = 0.04$, $s_N^{\varepsilon} = 0.01$, and $\varepsilon_N = 0.2$, are initially taken to be same for both phases. Parametric studies are carried out to explore the effect of variation in the values of f_0, f_c and ε_N for both phases on the bendability of DP steel sheets.

4.3 Results

The initial undeformed and deformed configuration of a bend specimen subjected to a macroscopic flexural strain, $\varepsilon_F \approx 0.05$, using a 90° V-bend punch are shown in Fig. 4.4(a). The distribution of the equivalent plastic strain ($\bar{\varepsilon}$) in the region $a'b'c'd'$ on the tension (convex) side of the deformed bend specimen at $\varepsilon_F \approx 0.05$ for the scenario where the entire bend specimen is modeled as homogenized DP steel is shown in Fig. 4.4(b). Similarly, the distribution of $\bar{\varepsilon}$ in the region $a'b'c'd'$ for the scenario where the DP steel microstructure is discretely modeled in the region $abcd$ and the rest of the specimen is modeled as homogenized DP steel is shown in Fig. 4.4(c). Finally, the macroscopic flexural stress (σ_F) - strain (ε_F) response of the bend specimen modeled as homogenized material and discrete DP steel microstructure in the region $abcd$ are compared in Fig. 4.4(d). The values of σ_F and ε_F are estimated as,

$$\sigma_F = \frac{3F_y L}{2Wd^2}, \quad \varepsilon_F = \frac{6\delta_y d}{L^2} \tag{4.2}$$

where, F_y is the reaction force on the punch and δ_y is the deflection of the tip of the punch along the loading direction.

The results in Fig. 4.4 correspond to the calculations with $f = 0$ everywhere in the specimen and throughout the deformation history i.e. the initiation and evolution of ductile damage are suppressed. As shown in Fig. 4.4(d), in the absence of any damage, the macroscopic σ_F - ε_F response of the homogeneous bend specimen is very similar to the response of the heterogeneous microstructure. This shows that the overall deformation response of DP steel sheets under bending is not very sensitive to the details of local microstructural length-scales. The comparison of σ_F

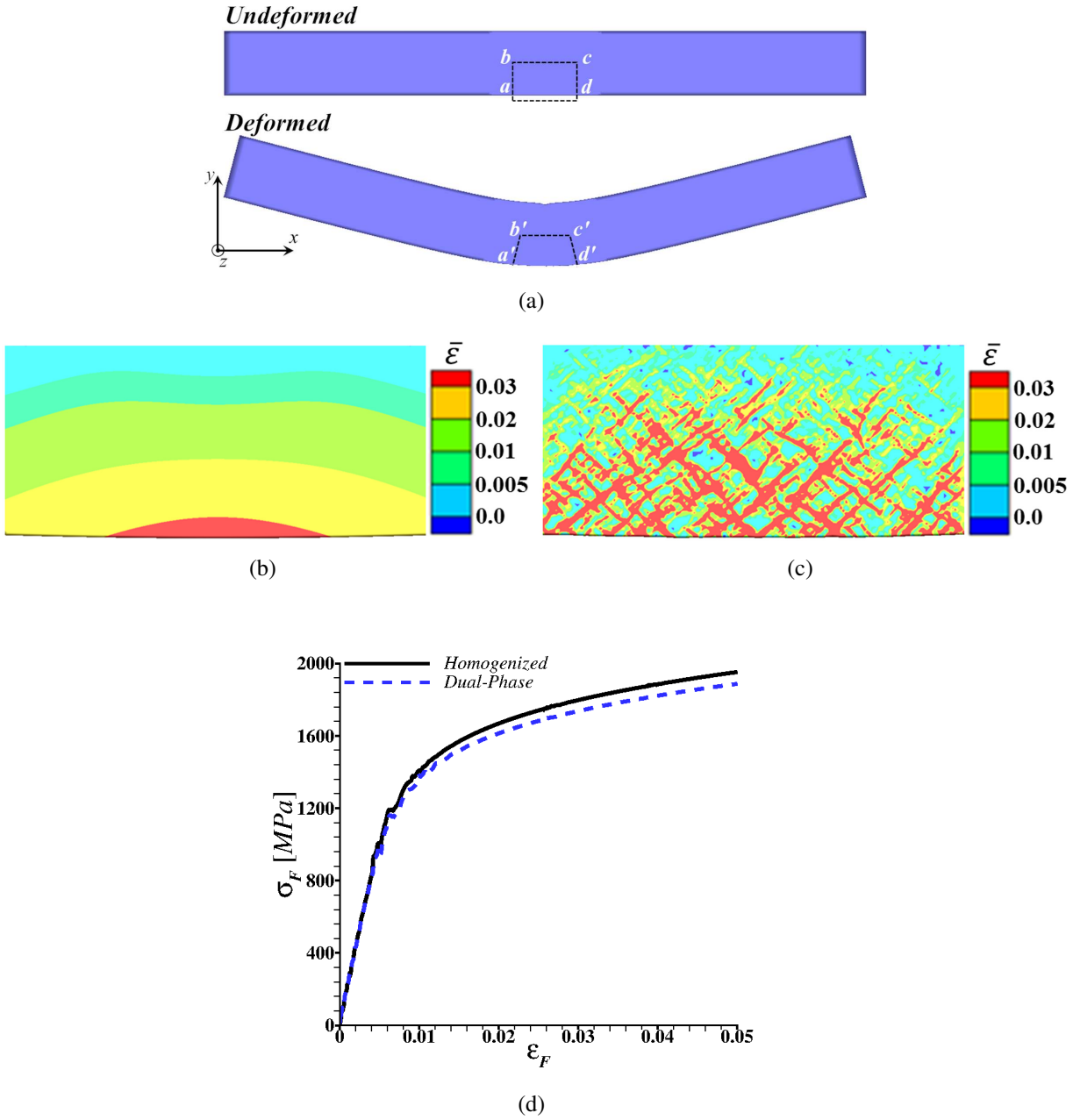

Figure 4.4: (a) The undeformed and deformed configuration of a bend specimen subjected to a macroscopic flexural strain, $\varepsilon_F \approx 0.05$, using a 90° V-bend punch. The distribution of equivalent plastic strain, $\bar{\varepsilon}$, in the near surface region ($a'b'c'd'$) on the tension side of the deformed bend specimen ($\varepsilon_F \approx 0.05$) with (b) homogenized material and (c) discrete DP steel microstructure in the region marked as $abcd$ in (a). (d) Comparison of the macroscopic flexural stress (σ_F) - strain (ε_F) response of the bend specimen modeled as homogenized material and discrete DP steel microstructure in the region marked as $abcd$ in (a).

- ε_F curves in Fig. 4.4(d) also shows that the extracted local mechanical properties of ferrite and martensite phases are correct. The discreteness of the local microstructure of the DP steel, however, does affect the local distribution of the field variables. For example, the local distribution of $\bar{\varepsilon}$, is very different in Fig. 4.4(c) compared to Fig. 4.4(b). In the homogeneous bend specimen, bending induces a single length-scale that leads to a smooth gradient in the distribution of $\bar{\varepsilon}$, Fig. 4.4(b) whereas, in the bend specimen with DP microstructure the interlacing of the length-scales induced by bending and DP microstructure results in extremely complex and heterogeneous distribution of $\bar{\varepsilon}$, Fig. 4.4(c).

4.3.1 Micromechanism of ductile fracture

The distribution of $\bar{\varepsilon}$ in the near surface region on the tension side of the deformed bend specimen with discrete DP steel microstructure undergoing damage initiation and growth at four ε_F values are shown in Figs. 4.5(a)-(d). The corresponding macroscopic σ_F - ε_F curve is shown in Fig. 4.5(e). The ε_F values corresponding to Figs. 4.5(a)-(d) are marked with letters $a - d$ on σ_F - ε_F curve in Fig. 4.5(e). The 'white' regions in Figs. 4.5(a)-(d) mark the locations of micro-crack nucleation and growth. Similarly, the distribution of stress triaxiality, $\sigma_h/\bar{\sigma}$, at four ε_F values corresponding to $a - d$ on σ_F - ε_F curve in Fig. 4.5(e) are shown in Figs. 4.6(a)-(d).

As shown in Figs. 4.5(a) and 4.6(a), in bend specimens with discretely modeled DP steel microstructure, the interlacing of length-scales induced by bending and material microstructure results in extremely heterogeneous distribution of strains and stresses even before the onset of any ductile damage. The length-scale induced by bending results in a gradient in the distribution of $\bar{\varepsilon}$ with the value of $\bar{\varepsilon}$ being greater at the surface, while due to the discreteness of the DP microstructure the value of $\bar{\varepsilon}$ is greater in the soft phase i.e. ferrite. Additionally, due to the local constrained imposed by the distribution of the hard phase i.e. martensite, the value of σ_h is greater in the ferrite phase while the value of $\bar{\sigma}$ is greater in the martensite phase. This results in greater $\sigma_h/\bar{\sigma}$ values in the ferrite phase.

With continued bending deformation, Fig. 4.5(b), the value of $\bar{\varepsilon}$ localizes in bands inclined at $\approx 45^\circ$ with the loading axis, and the free surface on the tension side undergoes surface rough-

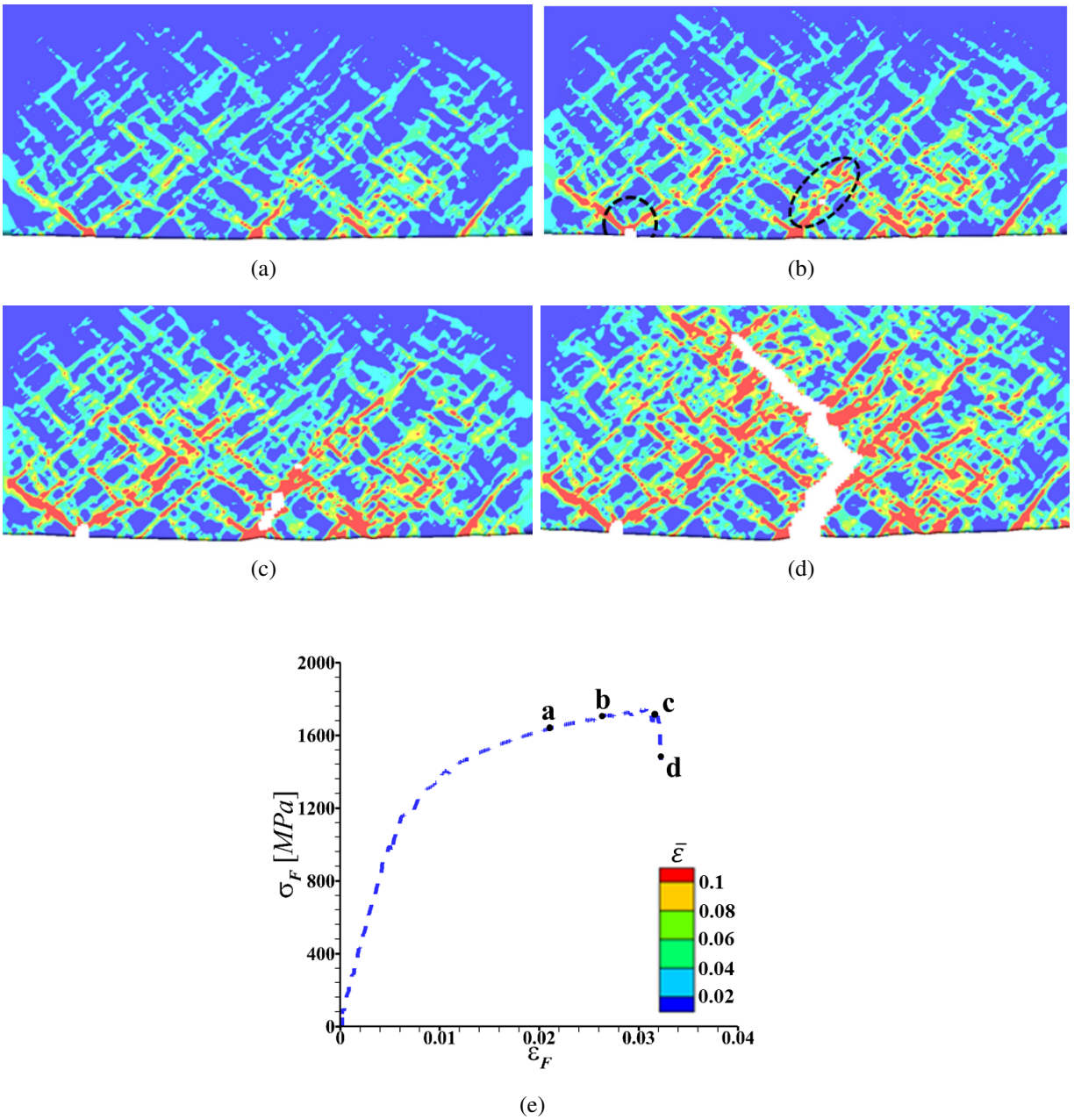

Figure 4.5: (a)-(d) The distribution of equivalent plastic strain, $\bar{\varepsilon}$, in the near surface region on the tension side of the deformed bend specimen with discrete DP steel microstructure at four macroscopic flexural strain, ε_F, levels marked with letters, $a - d$, on the macroscopic flexural stress (σ_F) - strain (ε_F) curve in (e).

ening. The 'hot spots' of $\sigma_h/\bar{\sigma}$ are however seems to be randomly distributed, Fig. 4.6(b). The interaction of $\bar{\varepsilon}$ localization bands and surface roughening results in nucleation of surface (marked

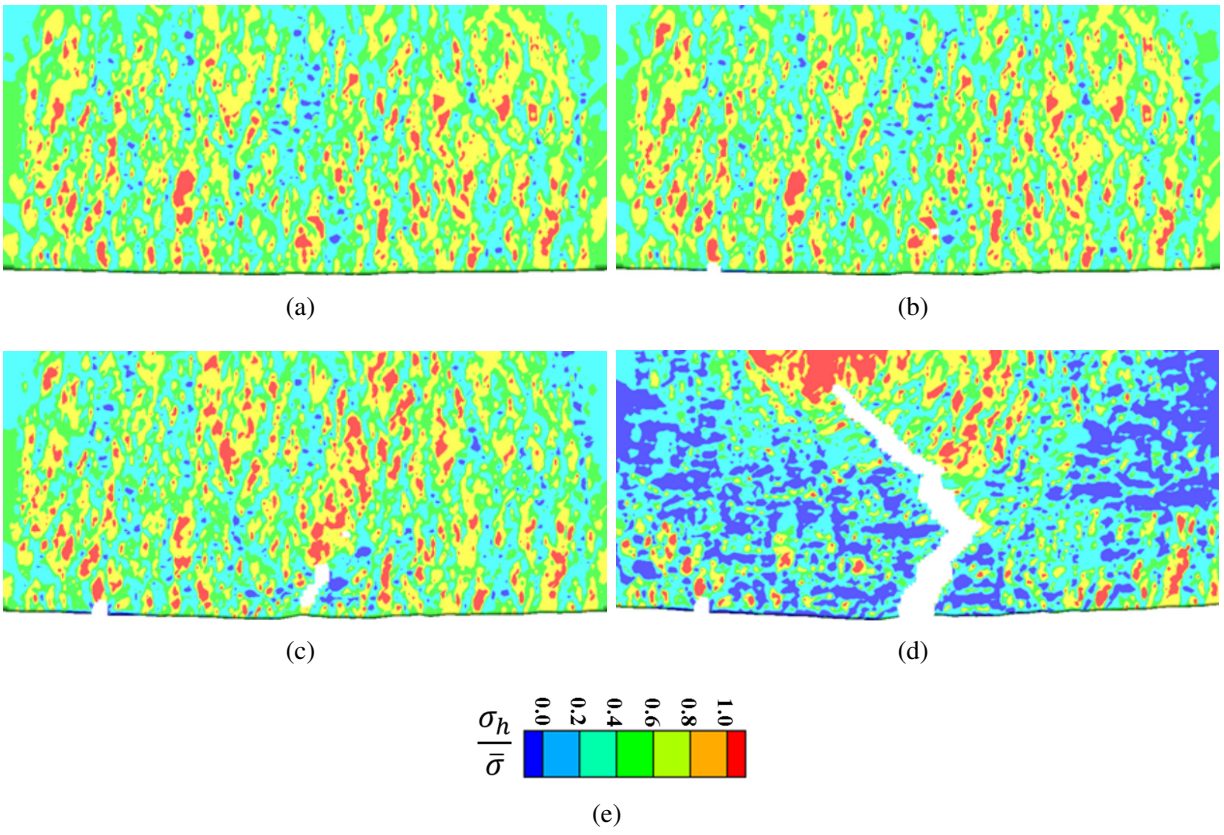

Figure 4.6: The distribution of stress triaxiality (ratio of hydrostatic stress and matrix flow strength), $\sigma_h/\bar{\sigma}$, in the near surface region on the tension side of the deformed bend specimen with discrete DP steel microstructure at four macroscopic flexural strain, ε_F, levels marked with letters, $a-d$, on the macroscopic flexural stress (σ_F) - strain (ε_F) curve in Fig. 4.5(e).

with dashed-line circle) and sub-surface (marked with dashed-line ellipse) micro-cracks that are away from the center of the specimen, Fig. 4.5(b). Note that in a homogeneous isotropic material under bending the cracks nucleate at the center of the specimen. The relatively large surface micro-crack that nucleates away from the center of the specimen does not seem to grow but with continued bending deformation the small sub-surface micro-crack marked with the ellipse in Fig. 4.5(b) grows towards the free surface along one of the $\bar{\varepsilon}$ localization band, Fig. 4.5(c). The presence of this large sub-surface micro-crack also results in redistribution of the 'hot spots' of $\sigma_h/\bar{\sigma}$, Fig. 4.6(c). The continued bending deformation, hereafter, results in growth of this micro-crack towards the interior of the specimen, Fig. 4.5(d), as well as drop in the macroscopic σ_F value,

Fig. 4.5(e). As shown in Figs. 4.5(d) and 4.6(d), the crack initially grows away from the loading axis but with continued bending deformation the crack deflects back towards the loading axis.

4.3.2 Effect of RD and TD microstructures

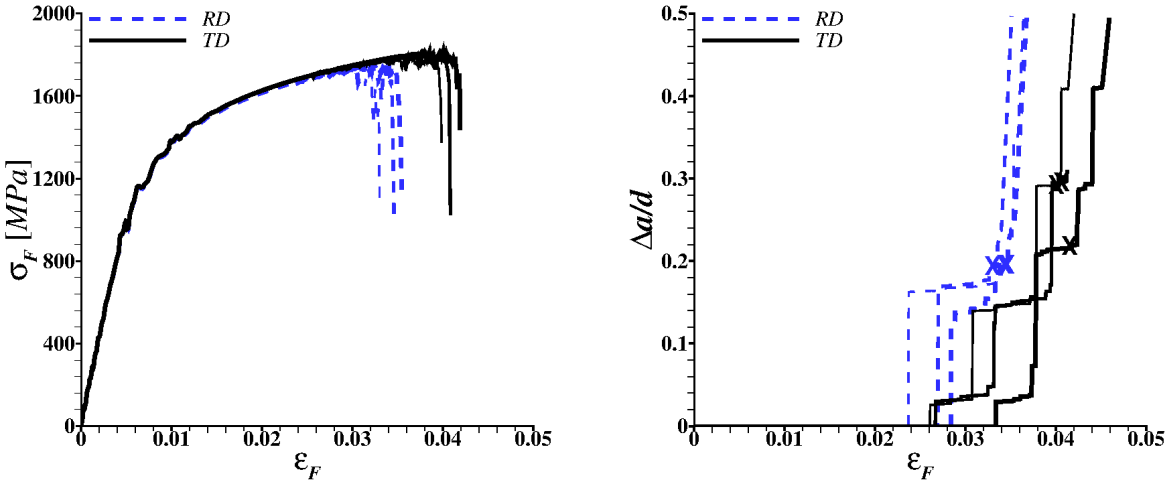

(a) (b)

Figure 4.7: (a) Macroscopic flexural stress (σ_F) - strain (ε_F) response of bend specimens with discrete DP steel microstructures corresponding to RD (rolling direction) and TD (transverse direction) cross-sections. (b) Evolution of normalized crack length, $\Delta a/d$, with ε_F. The values of $\Delta a/d$ at ε_F corresponding to drop in the value of σ_F in (a) is marked with cross in (b). For both RD and TD bend specimens, results for three microstructures taken from three locations on the respective cross-sections of the DP steel sheet are presented in (a) and (b).

Here, the effect of RD and TD microstructures on the bend fracture of DP steel sheets have been analyzed. The calculated macroscopic σ_F - ε_F curves for bending along RD and TD directions are shown in Fig. 4.7(a). The calculations show that the deformation response of RD and TD specimens under bending prior to fracture i.e. drop in the value of σ_F are the same. The value of ε_F corresponding to drop in the value of σ_F is however greater for TD specimens than for RD specimens. The three σ_F - ε_F curves for bending along RD and TD directions shown in

Fig. 4.7(a) are for three local microstructures taken from different locations on the respective cross-sections of the DP steel sheet. In all the calculations, RD or TD, the values of the constitutive parameters, overall volume fraction of the constituent phases, the specimen geometry and the loading conditions are the same so that the difference in the response of RD and TD specimens under bending is solely due to the variations in the topological features of the microstructure in RD and TD cross-sections. The evolution of the normalized crack length, $\Delta a/d$, with ε_F, is shown in Fig. 4.7(b). As shown in Fig. 4.7(b), the value of ε_F at first crack nucleation is on average greater for TD specimens than RD specimens. Furthermore, the evolution of Δa with ε_F is faster for RD specimens compared to TD specimens, resulting in poor damage tolerance and bend fracture resistance for RD specimens compared to TD specimens.

Next, the distributions of $\bar{\varepsilon}$ along a line in the subsurface of the tension side of bend specimens deformed to a macroscopic $\varepsilon_F \approx 0.03$ have been analyzed. The distribution is taken along a line parallel to the length of the specimen and at a depth of $y_0/d \approx 0.0325$ from the tension side of the specimen in the undeformed configuration. The distribution of $\bar{\varepsilon}$ along this line in a RD specimen is shown in Fig. 4.8(a) and in a TD specimen is shown in Fig. 4.8(b). Several general observations can be made from Figs. 4.8(a) and (b): (i) the value of $\bar{\varepsilon}$ in the ferrite phase is in general greater than the value of $\bar{\varepsilon}$ in the martensite phase, (ii) the peaks in the value of $\bar{\varepsilon}$ in the ferrite phases lies close to the ferrite-martensite interface, (iii) not all peaks in the value of $\bar{\varepsilon}$ in the ferrite (or in the martensite) region have the same amplitude, (iv) the peaks in the value of $\bar{\varepsilon}$ in the ferrite (or in the martensite) region with high amplitudes do not lie at the center of the bend specimen (contrary to what is expected for a homogeneous material undergoing bending), and (v) the number of peaks in the value of $\bar{\varepsilon}$ in the RD specimen is greater than the number of peaks in the TD specimen.

Similarly, the distribution of porosity, f, along the same line in the subsurface of the tension side of RD and TD bend specimens are shown in Figs. 4.8(c) and 4.8(d), respectively. In the calculations, void nucleation in both phases is assumed to follow a plastic strain controlled nucleation criteria, Eq. (2.9). So that the observed peaks in the value of f in the ferrite phase near the ferrite-martensite interface shown in Figs. 4.8(c) and (d) are consistent with the distribution of $\bar{\varepsilon}$

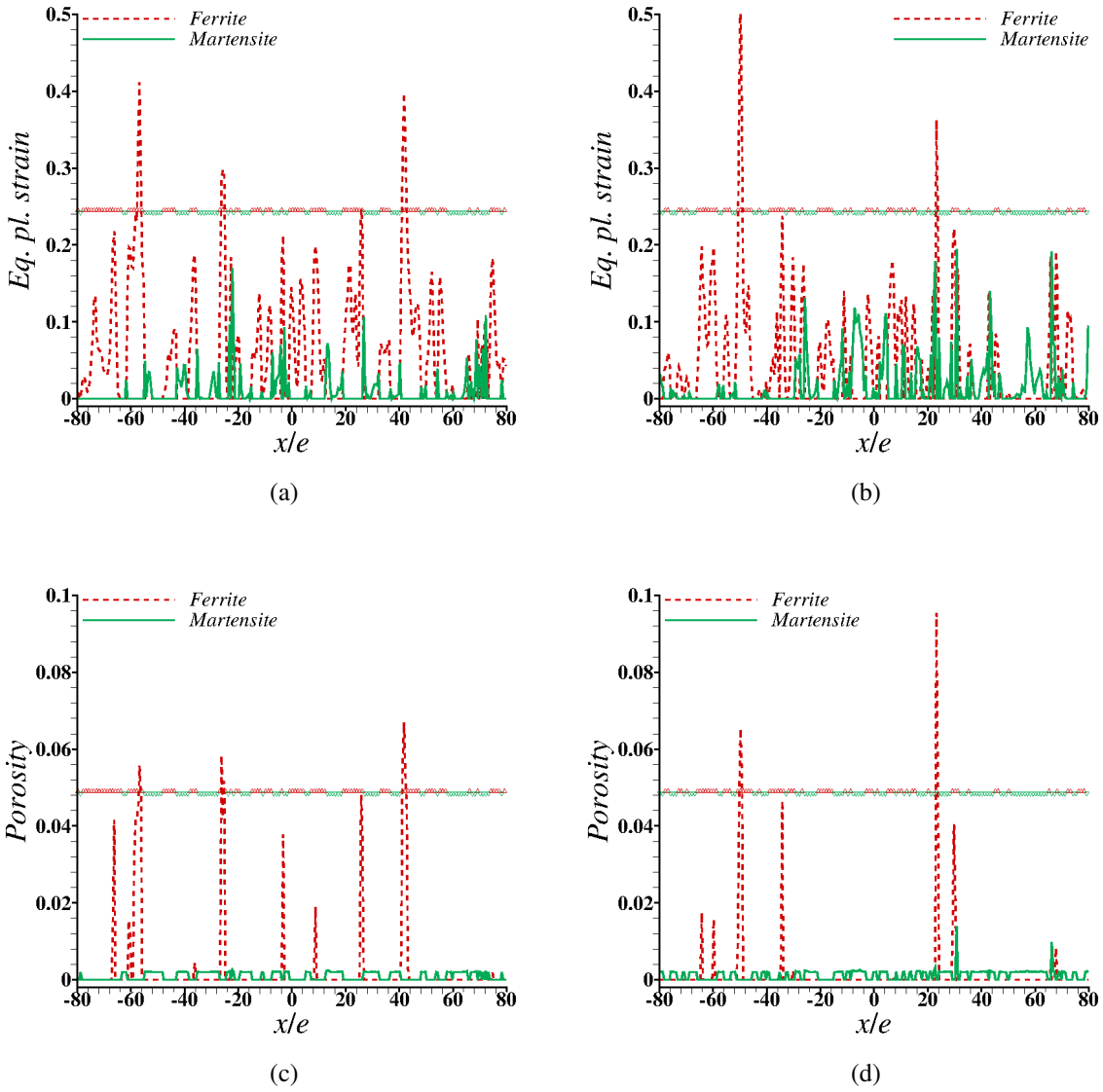

Figure 4.8: The distribution of equivalent plastic strain, $\bar{\varepsilon}$, at a macroscopic flexural strain, $\varepsilon_F \approx 0.03$, along a line in the subsurface of the tension side of bend specimens with discrete DP steel microstructures corresponding to (a) RD and (b) TD cross-sections. Similar distribution of porosity, f, at $\varepsilon_F \approx 0.03$ in (c) RD and (d) TD bend specimens. The line profile is taken along a line parallel to the length of the specimen (along x-axis) and at a depth of $y_0/d \approx 0.0325$ from the tension side of the specimen in the undeformed configuration. The location, $x/e = 0$, corresponds to the center of the bend specimen. The respective constituent phase along the line (i.e. at an x/e value) are marked with horizontally arranged symbols: $delta$ for ferrite phase and $gradient$ for martensite phase.

shown in Figs. 4.8(a) and (b). The growth of the nucleated voids, however, strongly depend on the local stress state thus not all the locations (corresponding to ferrite phase) where a peak in the value of $\bar{\varepsilon}$ is observed in Figs. 4.8(a) and (b) contains a peak in the value of f in Figs. 4.8(c) and (d). Nevertheless, similar to the distribution of $\bar{\varepsilon}$ the number of peaks in the value of f in the RD specimen is greater than the number of peaks in the TD specimen. Recall, in the calculations it is assumed that the initial porosity in the ferrite phase is zero while the martensite phase contains a small amount of initial porosity, $f_0 = 0.002$. Despite the presence of initial porosity, the value of f in the martensite phase is significantly less than that in the ferrite phase at least up to $\varepsilon_F \approx 0.03$ i.e. prior to significant micro-cracking in the specimen.

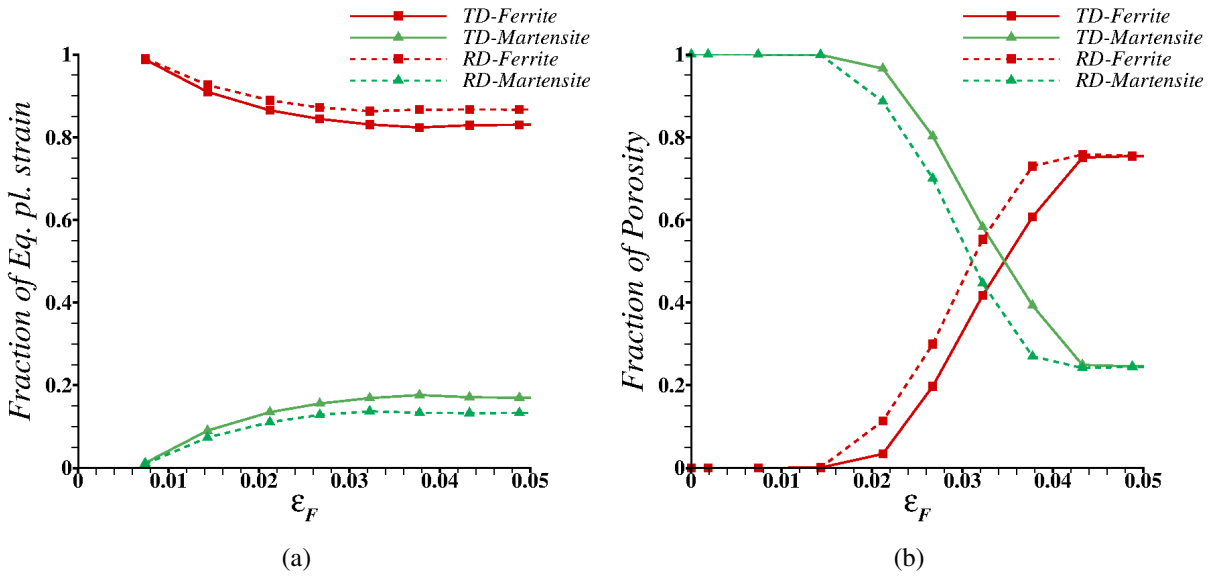

(a) (b)

Figure 4.9: Partitioning of (a) equivalent plastic strain, $\bar{\varepsilon}$, and (b) porosity, f, among the two constituent phases, ferrite and martensite, with macroscopic flexural strain, ε_F, in the bend specimens with discrete DP steel microstructures corresponding to RD and TD cross-sections.

To further understand the effect of RD and TD microstructures on the bend fracture of DP steel sheets, the contribution to the plastic strain and damage from each of the phases present in the DP steel at various macroscopic ε_F levels have been determined. To this end, the $\bar{\varepsilon}^{Phase}$ and f^{Phase} in

each phase as has been defined as,

$$\bar{\varepsilon}^{Phase} = \frac{1}{V_{Phase}} \sum_{EL \in Phase} \bar{\varepsilon}^{(k)} V^{(k)}, \qquad f^{Phase} = \frac{1}{V_{Phase}} \sum_{EL \in Phase} f^{(k)} V^{(k)} \tag{4.3}$$

where the sum is taken over all the elements (ELs) within one of the two phases, $V^{(k)}$ is the volume of the k^{th} element, $\bar{\varepsilon}^{(k)}$ and $f^{(k)}$ are the equivalent plastic strain and porosity computed at the centroid of the k^{th} element, and V_{Phase} is the total volume of the phase present in the microstructure in the region marked as $abcd$ in Fig. 4.2(e). Then defining the fractional contribution to the total $\bar{\varepsilon}$ and f from each phase as the ratio of $\bar{\varepsilon}^{Phase}$ and f^{Phase} to the total $\bar{\varepsilon}$ and f in both phases, respectively.

The fractional contributions of $\bar{\varepsilon}$ and f by the two phases as a function of macroscopic ε_F in RD and TD specimens are shown in Fig. 4.9. As shown in Fig. 4.9(a), the ferrite phase yields at an early stage of deformation and hence initially contributes almost all the plastic strain. Following the yielding of martensite phase the contribution to plastic strain of ferrite phase decreases gradually and that of martensite phase increases gradually. On the other hand, due to the presence of initial porosity in the martensite phase almost all the contribution to porosity initially comes from the martensite phase, Fig. 4.9(b). Following void nucleation in the ferrite phase the contribution to porosity of ferrite phase increases rapidly and that of martensite phase decreases rapidly. Post failure i.e. drop in σ_F values (see Fig. 4.7(a)), the fractional contributions of $\bar{\varepsilon}$ and f by the two phases saturates. The general trend of the fractional contributions of $\bar{\varepsilon}$ and f by the two phases as a function of ε_F is same for both RD and TD specimens. However, at a fixed ε_F prior to failure, the difference in the fractional contributions of $\bar{\varepsilon}$ by the two phases in the RD specimen is greater than that in the TD specimen, suggesting that the deformation in the TD specimen is slightly more uniform than the RD specimen. The difference in the fractional contributions of f by the two phases at a fixed ε_F in the RD and the TD specimens is simply due to the fact that damage initiation in RD specimens occurs at a lower value of ε_F than in TD specimens.

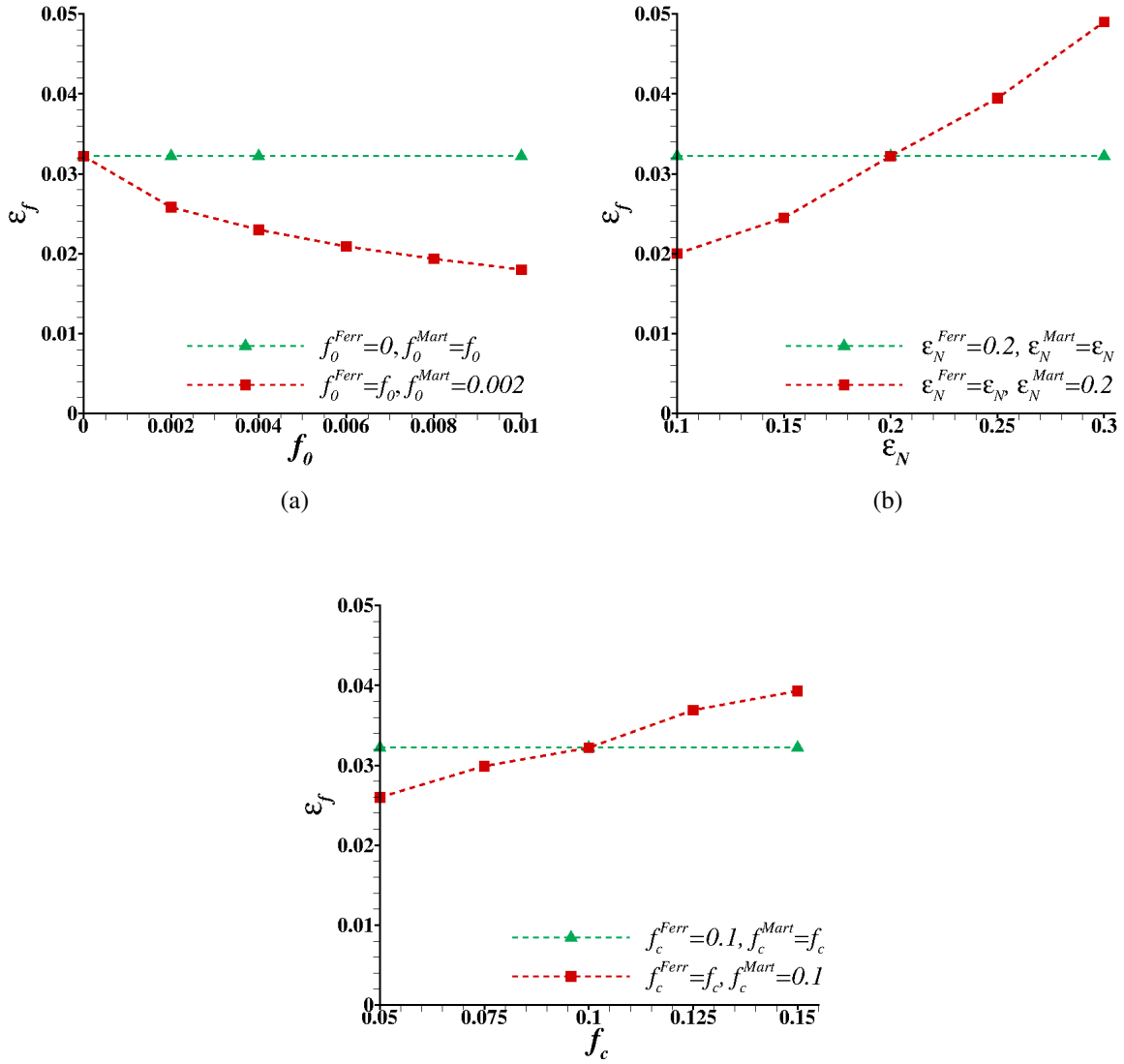

Figure 4.10: The effect of variation in (a) initial porosity, f_0, (b) mean equivalent plastic strain to void nucleation, ε_N, and (c) critical void volume fraction to void coalescence, f_c, in the two constituent phases, ferrite (superscript $Ferr$) and martensite (superscript $Mart$), of a DP steel microstructure corresponding to RD cross-section on macroscopic flexural strain at failure, ε_f.

4.3.3 Effect of damage parameters

In this section, influence of ductile damage parameters on the bend fracture of DP steel sheets have been presented. The damage parameters that are considered, are the initial porosity, f_0, the

mean equivalent plastic strain to void nucleation, ε_N, and the critical void volume fraction to void coalescence, f_c. The parameter, f_c, dictates the energy dissipated in the growth of nucleated voids prior to micro-crack nucleation. The parametric studies are carried out by varying the values of f_0, ε_N and f_c, one at a time, for each constituent phase. The results of this parametric study are shown in Fig. 4.10. As shown in the figure, a variation in the value of f_0, ε_N and f_c for the martensite phase has no effect on the macroscopic flexural strain to failure, ε_f, of DP steel sheets. On the contrary, a variation in the value of f_0, ε_N and f_c for the ferrite phase has a strong influence on the value of ε_f of DP steel sheets. Such that an increase in f_0 results in a decrease in ε_f while an increase in ε_N and f_c results in an increase in the value of ε_f.

4.4 Discussion

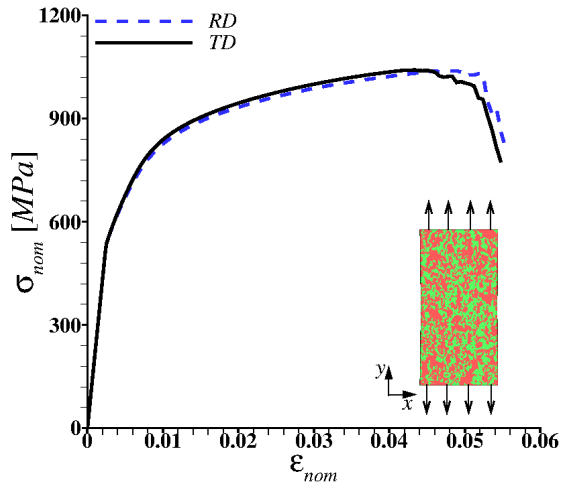

Figure 4.11: Comparison of the calculated uniaxial tensile nominal stress (σ_{nom}) - strain (ε_{nom}) response of DP steel microstructures corresponding to RD (rolling direction) and TD (transverse direction) cross-sections.

The experimental results, Fig. 4.3, and microstructure-based finite element calculations, Fig. 4.11, both show that the uniaxial tensile deformation and fracture response of the DP sheet steel under

consideration is not very sensitive to the details of the topological features of the microstructure along RD and TD. The microstructure-based finite element calculations of DP steel sheets are carried out for a thin slice of material with dimensions, $l_y = 1.6mm$, $l_z = 0.01mm$ and l_x given as,

$$l_x = l_x^0 - 2A\cos(2\pi\frac{y}{2l_y}), \qquad \left(-\frac{l_y}{2} \leq y \leq \frac{l_y}{2}\right) \tag{4.4}$$

where A is the amplitude of a small geometrical imperfection to the width, l_x^0, of the sheet specimen. The small geometrical imperfection is introduced to break the symmetry of the problem and facilitate onset of necking. The value of l_x^0 is taken to be $0.8mm$ and that of A is taken to be 1% of l_x^0. Overall plane strain conditions are imposed on $z = 0$ and $z = l_z$ surfaces of the sheet specimen and the uniaxial tensile loading along the y-axis is simulated using a velocity profile similar to Eq. (6.6). In the calculations, both RD and TD microstructures of the DP steel sheet are modeled using the procedure described in Section 5.2.1 and the values of the constitutive parameters given in Section 4.2.2. The microstructure-based finite element calculations of DP steel sheets under uniaxial tension are carried out for several RD and TD microstructures. The results show that for the set of constitutive parameters given in Section 4.2.2, under uniaxial tension, the average nominal strain to fracture is 0.053 with a standard deviation of 0.0065 for RD specimens and for TD specimens it is 0.05 with a standard deviation of 0.0031.

The unstructured continuum material property descriptors such as, strength and strain hardenability, the overall microstructural parameter i.e. volume fraction of the phases, and the fracture response under uniaxial tensile loading are same for both RD and TD specimens of the DP steel under consideration. So that any analysis based on classical engineering fracture mechanics will predict the same fracture response for both RD and TD specimens under bending. Nonetheless, consistent with the experimental observations, the results show that the bendability of TD specimens is greater than the bendability of RD specimens. In the calculations, the difference in the bendability of RD and TD specimens are due to the difference in the topological features of the material microstructure in RD and TD specimens of the DP steel sheet.

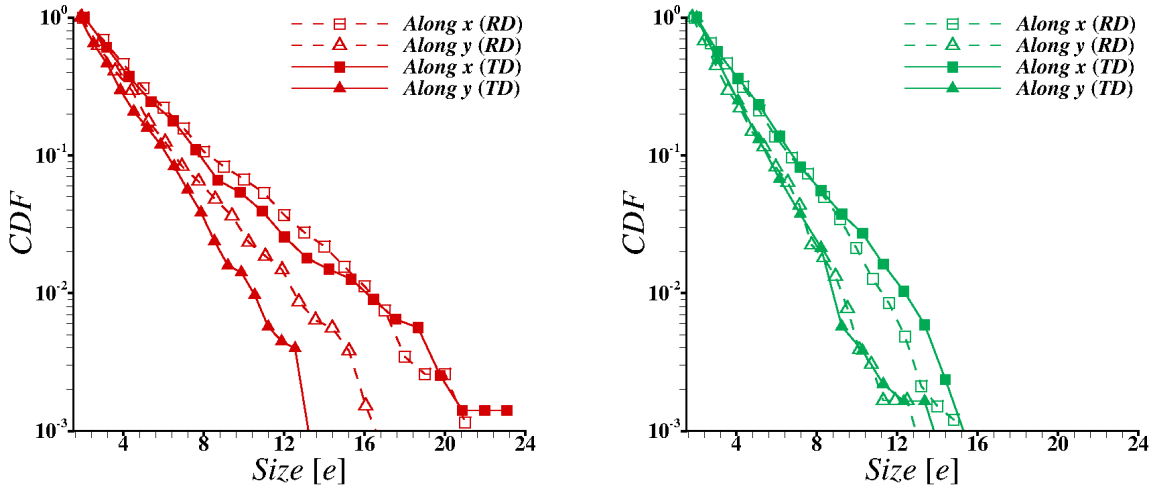

Figure 4.12: The descending cumulative distribution function (CDF) of (a) the size of ferrite phase in the modeled DP steel microstructure along x (specimen length) and y (specimen depth) axes in rolling (RD) and transverse direction (TD) cross-sections, and (b) the size of martensite phase in the modeled DP steel microstructure along x and y axes in RD and TD cross-sections. The vertical axes in the plots are on logarithmic scale, and e is the normalization length-scale.

The descending cumulative distribution function of the sizes of ferrite and martensite phases in RD and TD specimens of the DP steel sheet modeled are shown in Fig. 4.12. The plots in Fig. 4.12 can be interpreted as displaying the probability that the size will exceed a given value on the horizontal axis. From Fig. 4.12, it can be seen that the probability that the size of the ferrite phase along the specimen length and that of the martensite phase along the specimen depth will exceed a given threshold is roughly the same for both RD and TD specimens. The probability that the size of the ferrite phase along specimen depth will exceed a given threshold is, however, greater for RD specimens compared to TD specimens. Similarly, the probability that the size of the martensite phase along the specimen length will exceed a given threshold is slightly greater for TD specimens compared to RD specimens. Note, that since the volume fraction of both phases are same in RD and TD specimens, Fig. 4.12 suggest that the probability of finding deeper ferrite-martensite interfaces are greater for RD specimens compared to TD specimens.

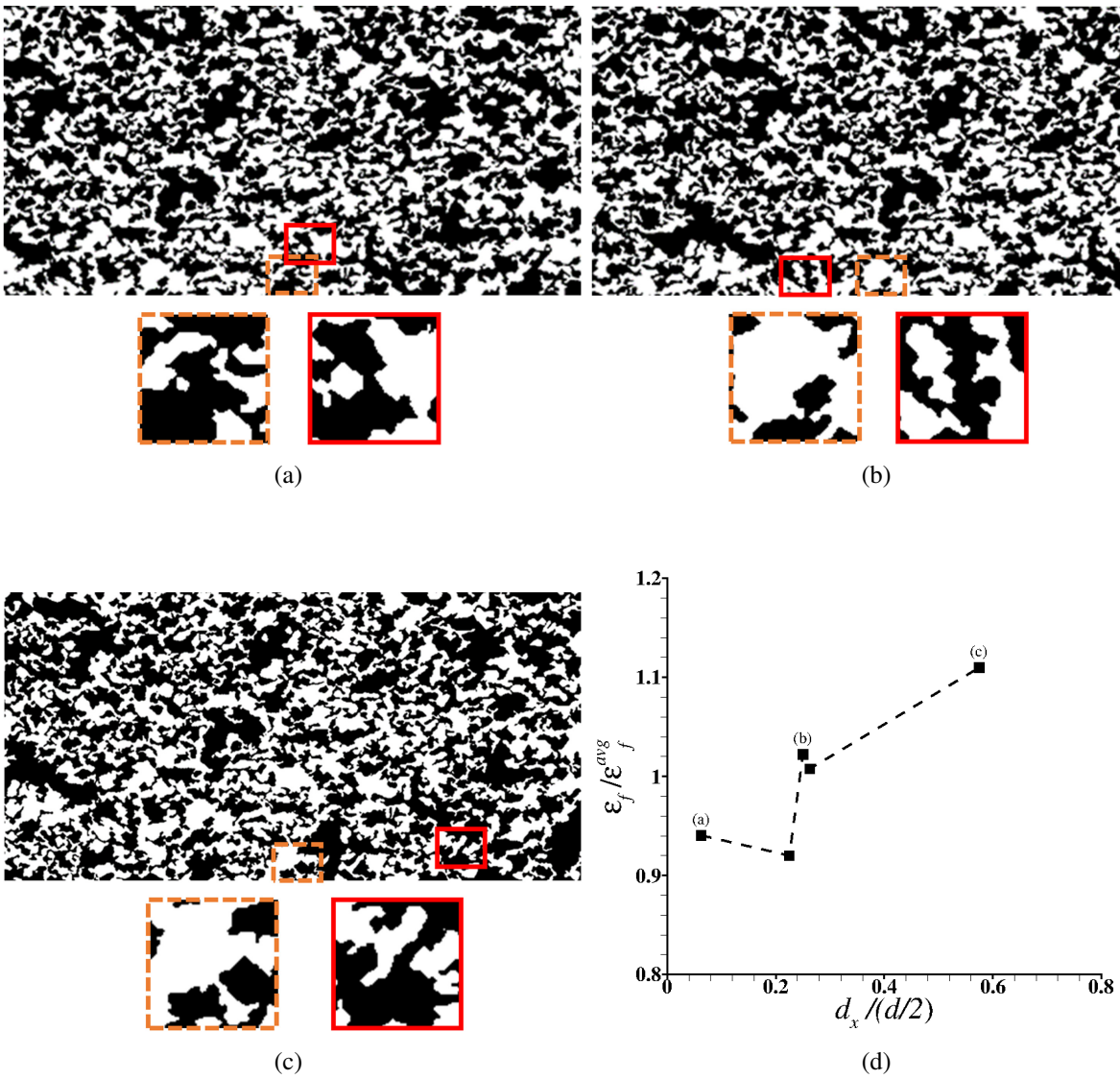

Figure 4.13: (a)-(c) The distribution of ferrite (black) and martensite (white) phases in three DP steel microstructures corresponding to RD cross-section. In (a)-(c), the bottom edge of the figure is on the tension side of the bend specimen, and the dashed-line box highlights the local microstructure in the center of the bend specimen while the solid-line box highlights the microstructure at the location of first micro-crack nucleation. (d) The variation of the normalized macroscopic flexural strain at failure, $\varepsilon_f/\varepsilon_f^{avg}$, with the normalized projected (along the length of the bend specimen or x-axis) distance between the center of the bend specimen and the location of first micro-crack nucleation, $d_x/(d/2)$.

The subtle difference in the size of ferrite and martensite phases between RD and TD specimens of the DP steel sheet is apparently sufficient to cause a difference in the fracture response under

bending. This is because bending results in an overall gradient in the distribution of $\bar{\varepsilon}$ with the value of $\bar{\varepsilon}$ being greater at the surface and within this gradient the value of $\bar{\varepsilon}$ is greater in the ferrite phase close to the ferrite-martensite interface. With continued bending deformation the value of $\bar{\varepsilon}$ localizes in bands inclined at an angle ($\approx 45°$) with the loading axis. The peaks in the value of $\bar{\varepsilon}$ in the ferrite phase close to the ferrite-martensite interface results in void nucleation at these locations. The small difference in the topological features of the microstructure between RD and TD specimens results in: (i) fewer number of peaks in the value of $\bar{\varepsilon}$ and f near the tension side of TD specimens compared to RD specimens, and (ii) slightly smaller difference in the fractional contribution of $\bar{\varepsilon}$ by the two phases in TD specimens compared to RD specimens.

The results of parametric studies show that in DP steel sheets under bending both the plastic deformation, and the damage nucleation and growth are concentrated in the ferrite phase. This is why, a variation in the values of the material parameters that dictate the propensity of void nucleation, energy dissipated in the growth of nucleated voids prior to crack nucleation, and initial porosity on ductile fracture of DP steel sheets under bending for martensite phase does not significantly affect the bendability of DP steel sheets. Thus, any effort to improve the bendability of DP steel sheets must focus on improving the mechanical properties of the ferrite phase.

The results presented in Fig. 4.7, show that even though the overall volume fraction, mechanical properties and damage parameters of the constituent phases and the orientation (RD or TD) of the bend specimens of the DP steel sheet are the same, there is a difference in the value of the macroscopic flexural strain to failure, ε_f, for different bend specimens. The difference in the value of ε_f for different RD (or TD) specimens stems from the specimen to specimen variation in the microstructure. The microstructure of three RD bend specimens are shown in Figs. 4.13(a)-(c) together with the zoomed view of the local microstructure in the center of the bend specimen and the crack nucleation site. The volume fraction of the ferrite phase in the local microstructure at the center of the bend specimens shown in Figs. 4.13(a)-(c) are ≈ 0.66, ≈ 0.44 and ≈ 0.29, respectively, while the volume fraction of the ferrite phase in the local microstructure at the first crack nucleation sites are ≈ 0.52, ≈ 0.58 and ≈ 0.49, respectively. This suggests that a right

combination of the amount of ferrite phase and constraint imposed by the martensite phase is needed to nucleate a crack. Anyhow, analyses show that the values of ε_f can be correlated with the projected distance between the center of the bend specimens and the crack nucleation site. As shown in Fig 4.13(d), the value of ε_f increases with increasing distance between the center of the bend specimen and the crack nucleation site.

The microstructure-based finite element calculations here have been carried out using a fixed finite element mesh so the question arises as to the extent of mesh dependence. In a grid based calculation such as finite element method, in the absence of a physical length-scale, the finite element mesh size is the dominant length-scale. However, in the microstructure-based finite element calculations, the discretely modeled material microstructure introduces microstructural length-scale(s). This is apparent from the predicted difference in the ductile fracture response of RD and TD specimens of DP steel sheets under bending. In addition, the rate dependence in the constitutive relation, Eq. (2.7), also regularizes the mesh dependence issues associated with localization of deformation [172]. Although, it is not possible to guarantee that the finite element mesh size does not play any role, a simple mesh convergence study show that for the mesh size considered here, the role of mesh size is not dominant. Here, the finite element mesh size convergence by carrying out bending calculations of a RD specimen with element sizes, e = $8.3\mu m$, $10.0\mu m$, and $12.5\mu m$ in the fine mesh region (marked as $abcd$ in Fig. 6.8) and comparing the predicted values of ε_f have been assessed. The results of this exercise show that decreasing the mesh size from $12.5\mu m$ to $10.0\mu m$ results in a $\approx 8.6\%$ decrease in the value of ε_f, whereas further decreasing the mesh size from $10.0\mu m$ to $8.3\mu m$ results in an insignificant change in the value of ε_f.

4.5 Conclusions

Microstructure-based finite element modeling to understand the influence of the interlacing of length-scales induced by 90° V-bend loading conditions and microstructure on ductile crack nucleation and early stage ductile crack growth in a DP steel with tensile strength of order $1GPa$ have been carried out. In the calculations, the microstructural features, ferrite and martensite phases, of the DP steel are discretely modeled in a thin slice of bend specimen normal to the

bend axis using a constitutive relation for progressively cavitating elastic-viscoplastic solid. The calculations are carried out for several microstructures taken from both RD and TD cross-sections of the DP steel sheet. Parametric studies are also carried out to explore the effect of material parameters that govern the ductile damage and crack nucleation.

The key conclusions are as follows:

1. In-line with the experimental observations, the calculations predict that despite similar strength and strain hardenability, volume fraction of the phases, and fracture response under uniaxial tension along RD and TD, the bendability of RD specimens are less than the bendability of TD specimens. The difference between the bendability of RD and TD specimens in the calculations naturally emerge due to the differences in the topological features of the microstructure along RD and TD.

2. The interlacing of length-scales induced by bending and DP microstructure results in an overall gradient in the distribution of $\bar{\varepsilon}$ with the value of $\bar{\varepsilon}$ being greater at the surface and within this gradient the value of $\bar{\varepsilon}$ being greater in the ferrite phase close to the ferrite-martensite interface.

3. The greater values of $\bar{\varepsilon}$ in the ferrite phase close to the ferrite-martensite interface results in void nucleation at these locations. The growth of these nucleated voids, however, depends on the constrained imposed by the local distribution of the martensite phase.

4. A variation in the values of the material parameters that govern the ductile damage and crack nucleation in the ferrite phase significantly affect the bendability of DP steel sheets. Thus, efforts to improve the bendability of DP steel sheets must focus on improving the mechanical properties of the ferrite phase.

5. The variation in the bendability of DP steel sheet specimens with fixed overall microstructure and sheet orientation can be correlated with the distance between the center of the bend

specimen and the crack nucleation site, such that an increase in the distance results in an increase in the bendability.

5. EFFECT OF INCLUSIONS ON THE BENDABILITY OF DUAL-PHASE STEELS

5.1 Background

A 10% reduction in the weight of an automobile results in 6-8% increase in the fuel efficiency [15]. One of the primary approaches to reducing weight is through increased use of materials with relatively high specific strength such as advanced high strength steels [23]. The potential of weight reduction through increased use of advanced high strength steels in automobiles has been estimated to be as high as 25% [25]. Advanced high strength steels derive their exceptional mechanical properties from a well-engineered complex, heterogeneous microstructure. With an exception of few, most advanced high strength steels comprise two or more phases (a combination of martensite, ferrite, retained austenite or bainite) which help achieve desired properties [23]. Of the various advanced high strength steels, dual-phase steels [148], are one of the most widely sought after materials for automotive applications [27]. The microstructure of advanced high strength dual-phase steels primarily consists of hard martensite phase islands dispersed in comparatively softer ferrite phase matrix, together with a small amount of process induced non-metallic inclusions [173], Figs. 5.1(a) and (b).

The influence of the 'intended' ferritic-martensitic microstructure on the deformation and fracture response of dual-phase steels has been a topic of numerous experimental and computational studies, for example [2,48,63,63,64,66,71,75,78,80,150,152,156,157,160,161,163–166,174,175]. These studies have shown that the deformation and fracture characteristics of dual-phase steels, especially those with high martensite content and high tensile strength, are quite complex. The macroscopic flow behavior of these dual-phase steels exhibits low initial yield strength due to early yielding in ferrite, followed by steep strain-hardening while martensite is still elastic and finally significant reduction in strain-hardening post yielding in martensite. In high strength dual-phase steels decohesion at ferrite/martensite interface and separation of adjacent martensite particles result in damage nucleation; and damage evolution depends on the volume fraction, morphology and

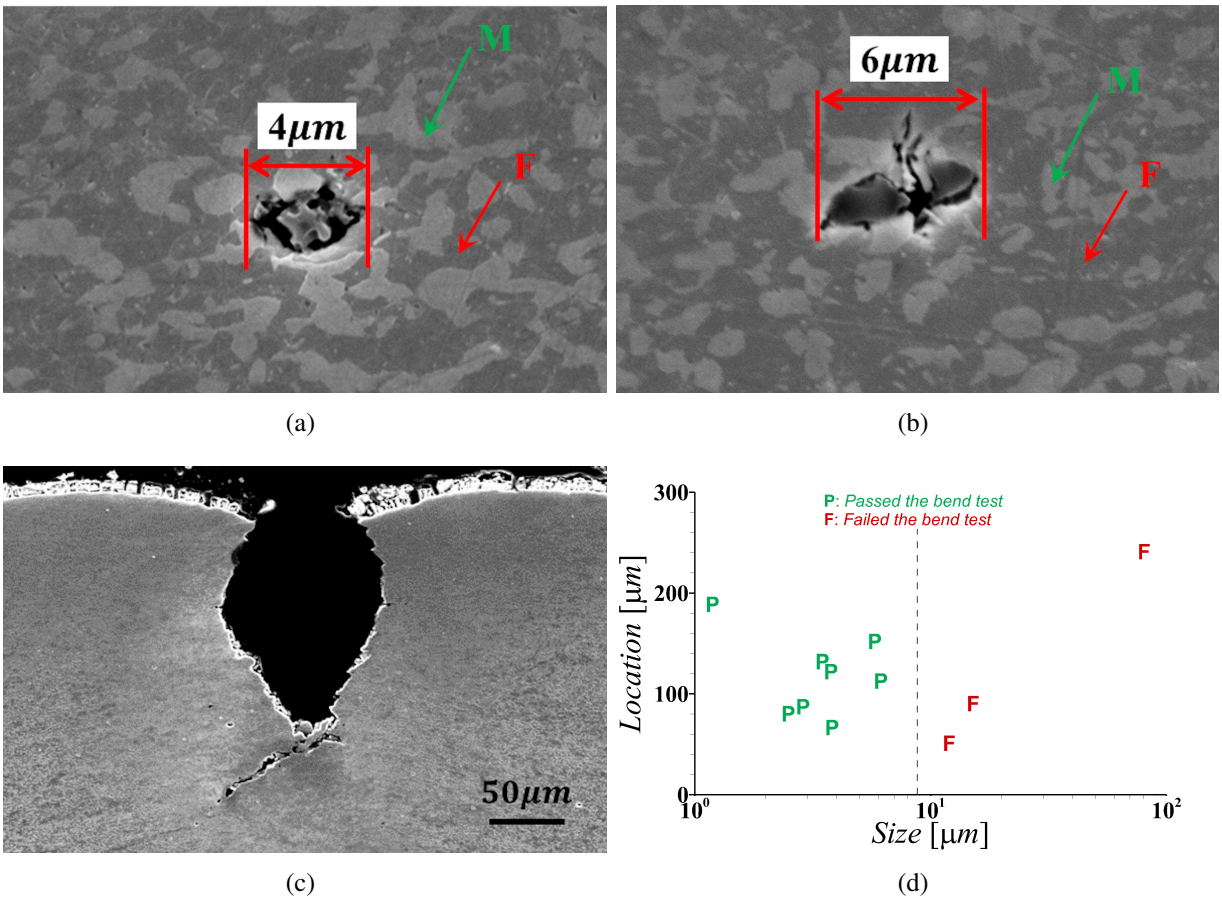

Figure 5.1: SEM images of an advanced high strength dual-phase, DP1000, steel specimens showing (a)-(b) the 'intended' ferritic (F)-martensitic (M) microstructure and 'unintended' sub-surface inclusions in the undeformed material and (c) cross-section of a deep surface crack formed during 90° V-bending. (d) Experimental results showing the effect of the location (distance from the tension side free surface) and size of sub-surface inclusions on the bendability of DP1000 steel sheets.

distribution of martensite, and the difference between the mechanical properties of the two phases. Note that in contrast to damage evolution (void growth) in a homogeneous material, the growth leading to coalescence of voids along an interface of two elastic-plastic material is much more severe, Section 4. This is because the coalescence of adjacent voids along the ferrite/martensite interface preferential occurs in the softer ferrite phase and close to the interface [48]. This also leads to a breakdown in scale separation [53], making it challenging to mathematically represent

dual-phase steels as 'effective homogenized media' post damage nucleation.

The dual-phase steels with high tensile strength ($\approx\ 1.0GPa$) are the targeted material for automotive applications to reduce overall weight while enhancing the crash worthiness. However, these high strength steels are prone to fracture under bending dominated manufacturing processes [4, 167]. At industrial scale, the bendability of a sheet metal is in general characterized by 90° V-bend test. In this test, a specimen of the sheet metal is deformed at a constant speed using a 90° V-bend punch, and post deformation the tension side of the specimen is visually inspected for the presence of cracks. A specimen fails the bend test, if a crack is observed post bending. A series of bend tests of a galvannealed DP1000 steel sheet of thickness $1.6mm$ conducted at ArcelorMittal Global R&D revealed significant sample to sample variability in the bendability of the steel. The root cause of sample to sample variability in the bendability of the steel, through detailed fractographic investigations, was associated with the presence of 'unintended' subsurface non-metallic inclusions, Figs. 5.1(a)-(c). It was also found that the inclusions in the high strength dual-phase steel exhibit strong size effect as shown in Fig. 5.1(d).

It is extremely difficult and expensive, if not impossible, to produce inclusion free steels. Nonetheless, the well-engineered microstructure of advanced high strength dual-phase steels does not contain large amount of inclusions. Also, the small amount of inclusions in dual-phase steels are in general assumed to have insignificant effect on the mechanical response of the material under simple uniaxial tensile loading condition [176, 177]. However, the mechanical response of a dual-phase material in an imposed deformation field that is homogeneous, such as those under uniaxial tension, is different from the response in an imposed deformation field that is heterogeneous, such as those under bending, Section 4. This is because, in the latter, damage nucleation and evolution involves the interaction of the length-scales induced by both bending and the material microstructure. So that, even a subtle difference in the material microstructure is exacerbated under bending. For example, in Section 4 it was shown that a dual-phase steel that under uniaxial tension exhibits similar mechanical response along the rolling and transverse directions, can exhibit very different mechanical response along the two directions under bending.

The objective of this work is to understand the effect of the length-scales induced by the mode of deformation i.e. bending, 'intended' dual-phase microstructure, and size, shape, location and properties of 'unintended' microstructural features i.e. inclusions, on crack nucleation and early stage crack growth in advanced high strength dual-phase steels. To this end, a series of microstructure-based finite element calculations of ductile crack nucleation and early stage crack growth in a dual-phase steel under 90° V-bend loading condition were carried out . The microstructure-based finite element calculations in this work builds on the recent work, Section 4 on ductile fracture of dual-phase steels under bending. In the calculations here, both the 'intended' microstructure of an industrially produced dual-phase steel, DP1000 (Fig. 5.1), as in Section 4 and the 'unintended' inclusions are discretely modeled in a thin slice of a bend specimen. To gain additional insight, the effect of an inclusion on the bendability of a single-phase material with material properties corresponding to the overall mechanical response of the dual-phase steel under consideration were analyzed.

The results show that the presence of a subsurface inclusion in the bend specimens leads to subsurface micro-void/crack nucleation under bending that can accelerate the localization of plastic strain in the material. In line with the experimental observations, strong inclusion size effects on the bendability of the dual-phase steels naturally emerge in the calculations. Furthermore, supervised machine learning to quantify the effect of the multivariable input space associated with the 'intended' and 'unintended' microstructural features on the bendability of the advanced high strength dual-phase steel were carried out. The supervised machine learning approach used here utilizes an ensemble learning method for classification and regression. The results of supervised machine learning are then used to identify the contribution of individual features and isolate critical features that control the bendability of the advanced high strength dual-phase steel. Specifically, the machine learning based analysis shows that unlike a single-phase material, the bendability of a dual-phase steel is not only affected by the features associated with the sub-surface inclusion but it is also affected by the underlying dual-phase microstructure.

5.2 Problem formulation

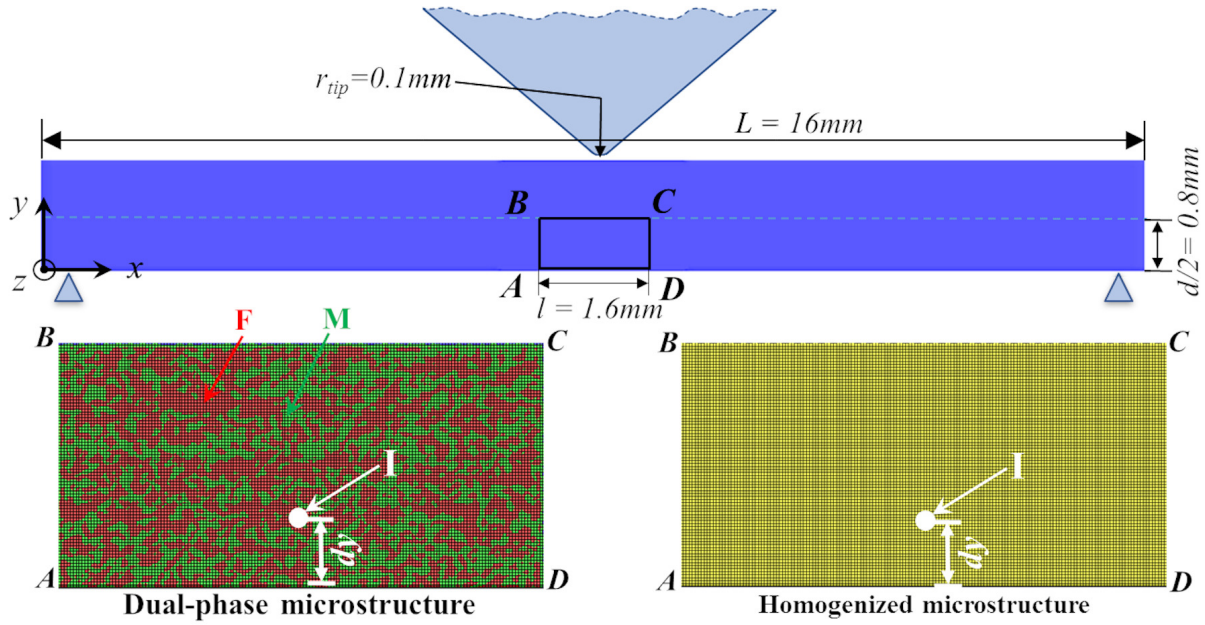

Figure 5.2: (top) A schematic of the bend specimen together with imposed constraint and loading conditions. (bottom left) A zoomed view of the finite element mesh near the free surface of the bend specimen of a dual-phase steel showing the discretely modeled ferrite (F) and martensite (M) phases, and an inclusion (I). (bottom right) A zoomed view of the finite element mesh near the free surface of the bend specimen of a single-phase material with an inclusion (I).

As in Section 4, microstructure-based finite element modeling of deformation and fracture of a dual-phase steel sheet subjected to 90° V-bend loading condition are carried out for a thin slice of material with dimension along z-axis i.e. $W = 0.01mm$, and other dimensions and details shown in Fig. 5.2. The finite element calculations are carried out using the in-house data parallel finite element code [1, 47], which is based on the dynamic principle of virtual work using a finite deformation Lagrangian convected coordinate formulation. More complete description of the finite element method is given in the references cited. For the finite element mesh a single element through the width, W, of the specimen is used and overall plane strain conditions are imposed on $z = 0$ and $z = W$ surfaces. A very fine uniform in-plane ($x - y$ plane) mesh is used in a

$1.6mm \times 0.8mm$ region (marked as $ABCD$ in Fig. 5.2) near the free surface of the bend specimen with in-plane element dimension $10\mu m \times 10\mu m$. The element dimension in the fine mesh region, $e = 10\mu m$, serves as a normalization length-scale. The finite element mesh of the entire specimen consists of $22,920$ twenty node brick elements. A mesh convergence study in Section 4 showed that for the mesh size considered in the fine mesh region, the role of mesh size is not dominant on the predictions of these microstructure-based finite element calculations.

The imposed displacement and velocity boundary conditions follows the configuration shown schematically in Fig. 5.2. Although the calculations are based on the dynamic principle of virtual work for numerical convenience, the focus is on the quasi-static response, hence to minimize the wave effects a time varying velocity, $V_y(t)$, in the negative y direction is applied to the tip of the punch that follows the relation:

$$V_y(t) = \begin{cases} V_y^0 t/t_r & \text{if} \quad t \leq t_r \\ V_y^0 & \text{if} \quad t > t_r \end{cases} \tag{5.1}$$

where, t is the analysis time, t_r is the rise time and V_y^0 is the final velocity of the punch for $t > t_r$. In the calculations, $t_r = 1.0 \times 10^{-4}s$ and $V_y^0 = 3.0 \times 10^3 mm/s$ (along the negative y direction) is used.

5.2.1 Microstructure modeling

As in Section 4, the material microstructure in a small area but large enough to capture the nucleation and coalescence of micro-cracks near the free surface of the specimen as shown in Fig. 5.2 were discretely modeled. To this end, 2D SEM images of the microstructure of an industrially produced galvannealed DP1000 steel sheet are digitized via Marker-Controlled Watershed Segmentation method [169]. The average size of ferrite and martensite phases in the as-produced steel are $2.09\mu m$ and $1.76\mu m$. Next, the SEM image is magnified by 20X to 'artificially' increase the feature sizes to allow choosing a reasonable mesh size to resolve the details of the dual-phase microstructure. The 20X magnification increases an actual length of $1\mu m$ to $20\mu m$ or in terms of the element dimension, e, it is simply $2e$, while keeping the overall volume fraction of the phases

fixed. The average size of the ferrite and martensite phases modeled in terms of the element dimension are ($2 \times r_F$ =) $4.18e$ and ($2 \times r_M$ =) $3.52e$, respectively. Finally, an inclusion of radius, r_I, is introduced in the digitized and magnified microstructure in the center along the length of the bend coupon (marked as 'I' in Fig. 5.2) at a distance dy from the free surface on the tension side. The dual-phase microstructure together with the inclusion are then superimposed on the finite element mesh in the region marked as $ABCD$ in Fig. 5.2, and material properties corresponding to respective microstructural features are assigned based on material (Gaussian) integration points rather than the finite elements. This allows to smoothly resolve the interphase boundaries. The region outside $ABCD$ in the bend specimen are assigned the material properties corresponding to the overall mechanical response of the dual-phase steel under consideration. To gain additional insight, the effect of an inclusion on the bendability of a single-phase material, Fig. 5.2, with constitutive parameters corresponding to the overall 'homogenized' dual-phase steel under consideration were analyzed.

5.2.2 Constitutive parameter identification

Table 5.1: The values of the constitutive parameters for the overall (homogenized) dual-phase (DP) steel, the individual constituent phases (ferrite and martensite) and the non-metallic inclusion.

Parameters	**DP**	**Ferrite**	**Martensite**	**Inclusion**
Young's modulus, $E(GPa)$	200	200	200	300
Poisson's ratio, ν	0.3	0.3	0.3	0.2
Initial flow strength, $\sigma_0(MPa)$	610	430	1450	$1.1\sigma_N$
Strain hardening exponent, N	0.14	0.35	0.06	0.001
Reference strain, ε_0	0.00175	0.06	0.006	σ_0/E
Strain rate sensitivity exponent, m	0.01	0.01	0.01	0.01
Reference strain rate, $\dot{\varepsilon}_0(\mathrm{s}^{-1})$	0.1	0.01	0.01	0.1

The constitutive framework described in Section 2.2 contains several constitutive (material) parameters that need to be determined. The values of the constitutive parameters associated with the

elastic-viscoplastic response of the fully dense ($f = 0$ throughout the deformation) 'homogenized' dual-phase microstructure and that of the individual constituent phases, ferrite and martensite, of the DP1000 steel under consideration were determined in Section 4 and are given in Table 5.1. The values of the constitutive parameters associated with the elastic-viscoplastic response of the inclusion in Table 5.1 are chosen to represent generic non-metallic inclusions such as, spinels, calcium aluminates, silicates, titanium nitride and alumina, that undergo linear elastic deformation up until the onset of damage nucleation, note for inclusions $\sigma_0 = 1.1\sigma_N$. As modeled, any inelastic deformation that occurs in the inclusions, occurs post damage nucleation and are modeled to allow graceful fracture of the inclusion for numerical convenience.

Apart from the constitutive parameters needed to model the mechanical response of the fully dense material that are given in Table 5.1, the constitutive framework detailed in Section 2.2 also contains parameters associated with the modified Gurson model. These parameters for the ferrite and martensite phases, and for the 'homogenized' dual-phase steel are, initial void volume fraction, f_0, critical void volume fraction to void coalescence, f_c, void volume fraction at failure, f_f, and the three parameters, f_N^{ε}, s_N^{ε}, ε_N associated with the void nucleation criteria in Eq. (2.9). Following the work of Section 4, $f_0 = 0$ was taken for the ferrite phase, $f_0 = 0.002$ for the martensite phase, and $f_0 = 0.001$ for the 'homogenized' dual-phase, while $f_c = 0.1$, $f_f = 0.2$, $f_N^{\varepsilon} = 0.04$, $s_N^{\varepsilon} = 0.01$, and $\varepsilon_N = 0.2$ are taken to be the same for all three. For the non-metallic inclusion, $f_0 = 0$, $f_c = 0.1$, $f_f = 0.12$, $f_N^{\sigma} = 0.1$ and $s_N^{\sigma} = 0.1\sigma_0$ are used in the calculations. Parametric studies are carried out to explore the effect of σ_N i.e. the strength of the inclusion on the bendability of the steel sheets.

5.3 Numerical results

The objective is to understand the effect of the length-scales induced by the mode of deformation i.e. 90° V-bending, 'intended' dual-phase microstructure, and size, shape, location and properties of 'unintended' microstructural features i.e. inclusions, on crack nucleation and early stage crack growth in advanced high strength dual-phase steels. To this end, a series of microstructure-based finite element calculations of ductile crack nucleation and early stage crack growth in a

dual-phase steel under 90° V-bend loading condition using the procedure detailed in Section 5.2 were carried out. For the purpose of comparison and to gain additional insight, the effect of an inclusion on the bendability of a single-phase material with constitutive parameters corresponding to the overall 'homogenized' dual-phase steel under consideration were analyzed. Firstly, the results of the finite element calculations of ductile fracture in a single-phase material with an inclusion under 90° V-bend loading condition were presented in Section 5.3.1. The results of the finite element calculations of ductile fracture in a dual-phase steel with discretely modeled dual-phase microstructure and inclusion under 90° V-bend loading condition are presented in Section 5.3.2.

5.3.1 Effect of an inclusion on the bendability of a single-phase material

The near surface distribution of equivalent plastic strain, $\bar{\varepsilon}$, on the tension side (in the region labeled as $ABCD$ in Fig. 5.2) of a 90° V-bend specimen of a single-phase material with an inclusion at four macroscopic flexural strain (ε_F) levels together with the macroscopic flexural stress (σ_F) - strain response are shown in Fig. 5.3. For the specimen in Fig. 5.3, inclusion size, $r_I \approx 3e$ (e is a normalization length-scale introduced in Section 5.2), strength, $\sigma_N \approx 0.5 \times \sigma_0$ (σ_N is defined in Eq. 2.10 and σ_0 is the initial flow strength of the 'homogenized' dual-phase or simply single-phase material given in Table 5.1) and is located at a distance, $dy = 0.125 \times d$ (dy is the distance from the free surface and d is the thickness of the specimen, Fig. 5.2). The values of the macroscopic σ_F and ε_F are estimated as,

$$\sigma_F = \frac{3F_y L}{2Wd^2}, \quad \varepsilon_F = \frac{6\delta_y d}{L^2} \tag{5.2}$$

where, F_y is the reaction force on the punch and δ_y is the deflection of the tip of the punch along the loading direction.

As shown in Figs. 5.3(a)-(c), in a single-phase material, sub-surface void nucleation ('white' region in the figures) due to the presence of a sub-surface inclusion results in the localization of $\bar{\varepsilon}$ in bands emanating from the sub-surface void that are oriented at $\approx 45^\circ$ with respect to the loading axis. As also shown in Figs. 5.3(a)-(c), the intensity of the localization of $\bar{\varepsilon}$ increases with

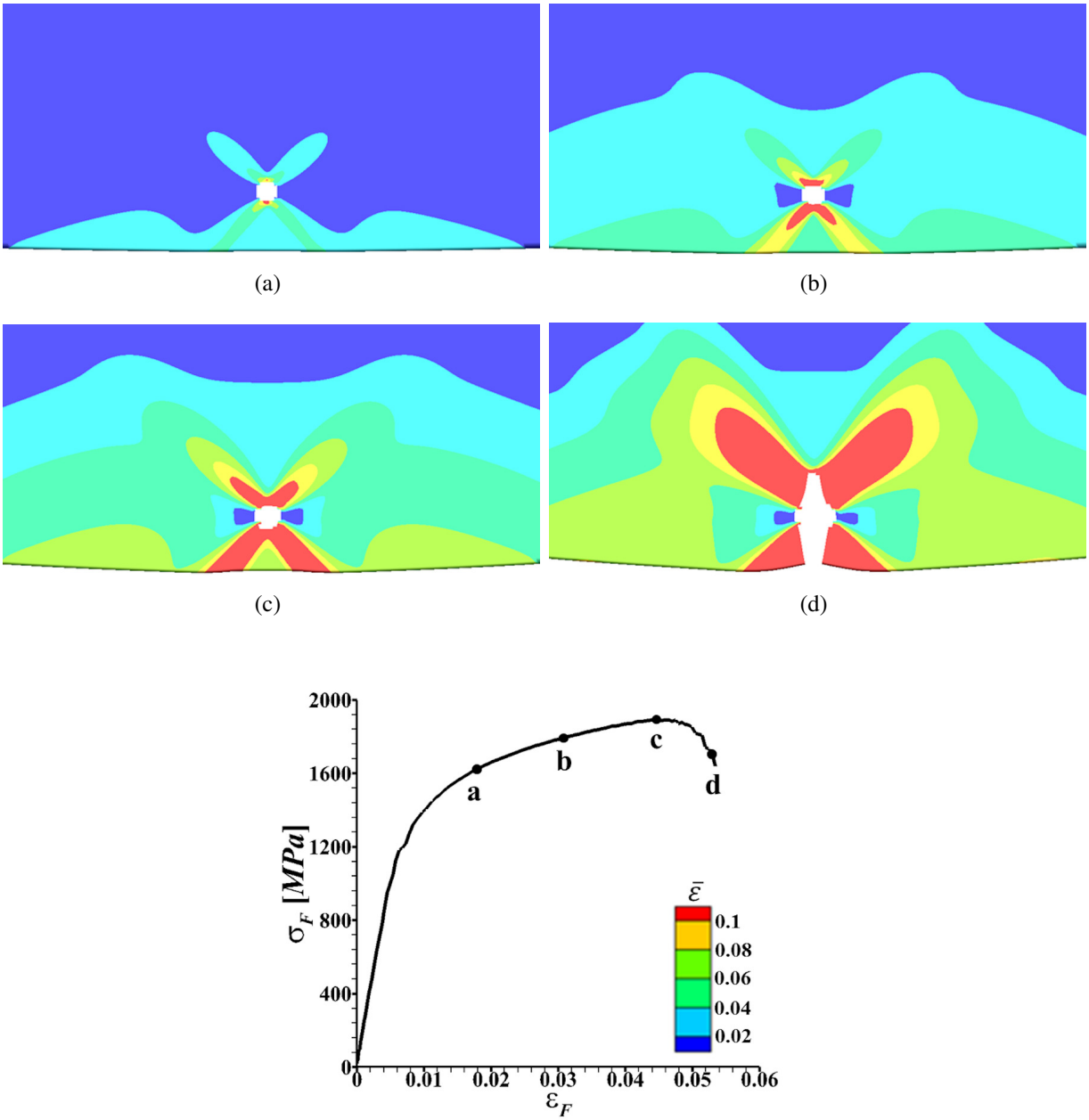

Figure 5.3: (a)-(d) The distribution of equivalent plastic strain, $\bar{\varepsilon}$, in the near surface region on the tension side of a deformed 90° V-bend specimen of a single-phase material with an inclusion of size, $r_I \approx 3e$, strength, $\sigma_N = 300MPa$ ($\sigma_N/\sigma_0 \approx 0.5$) and location, $dy/d = 0.125$, at four macroscopic flexural strain, ε_F, levels marked as, a-d, on the macroscopic flexural stress (σ_F) - strain (ε_F) curve in (e).

progressive bending. Next, with continued bending, the ligament between the surface and the sub-surface micro-crack parallel to the loading direction undergoes slight localized thinning that results in an increase in the value of the stress triaxiality in the thinned ligament. Subsequently, nucleation and propagation of a crack connecting the surface and the sub-surface void, Fig. 5.3(d), results in the final fracture i.e. loss of the load bearing capacity of the specimen which is marked by a drop in the value of σ_F, Fig. 5.3(e). The ductile fracture mechanism of the single-phase material with an inclusion under bending shown in Fig. 5.3 is qualitatively the same for the range of inclusion size, $1e \leq r_I \leq 5e$, and location, $0.0625 \leq dy/d \leq 0.3125$, considered in this work.

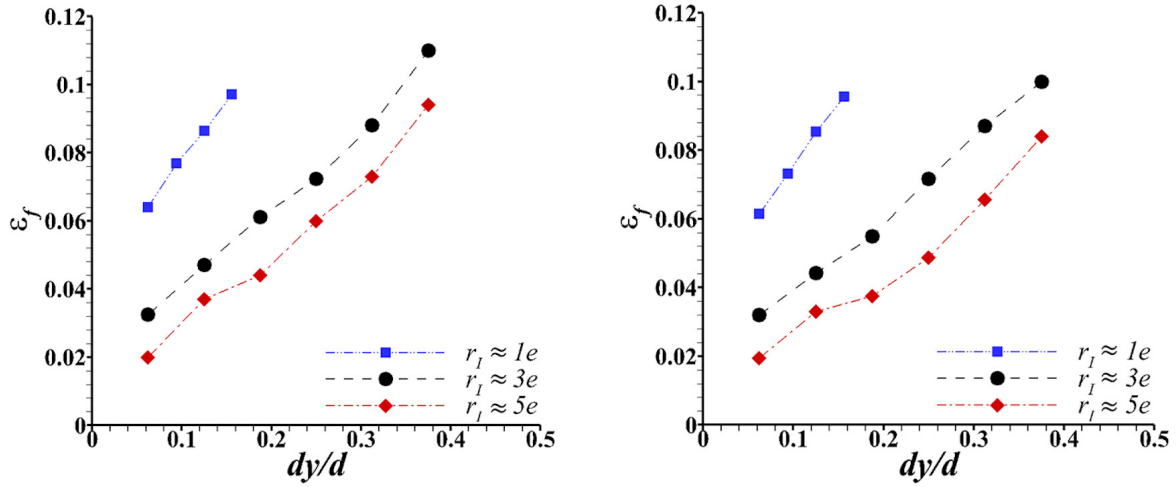

(a) (b)

Figure 5.4: Effect of the size, r_I, and location, dy/d, of an inclusion of strength (a) $\sigma_N = 300MPa$ ($\sigma_N/\sigma_0 \approx 0.5$) and (b) $\sigma_N = 800MPa$ ($\sigma_N/\sigma_0 \approx 1.3$) on the flexural strain to failure, ε_f, (i.e. bendability) of the single-phase material.

The effects of the inclusion size, r_I, location, dy/d, and strength, σ_N, on the bendability of a single-phase material with a sub-surface inclusion are shown in Fig. 5.4. The bendability of a specimen is characterized by the value of the macroscopic flexural strain to failure, ε_f, which is the value of ε_F that corresponds to the drop in the value of σ_F. As shown in Fig. 5.4(a), for

an inclusion of strength, $\sigma_N = 300MPa$, which is less than the initial flow strength, σ_0, of the material, the value of ε_f increases roughly linearly with increasing distance, dy/d, of the inclusion from the surface, for all three values of r_I considered in this work. While for a fixed value of dy/d, the value of ε_f decreases with increasing value of r_I. The effect of the inclusion size and location on the bendability of a single-phase material shown in Fig. 5.4(a) is unaffected by an increase in the value of the inclusion strength from $\sigma_N = 300MPa \approx 0.5 \times \sigma_0$ to $\sigma_N = 800MPa \approx 1.3 \times \sigma_0$, as shown in Fig. 5.4(b). Although, not presented here, the effect of an inclusion of strength, $\sigma_N \approx 2.6 \times \sigma_0$ have been analyzed. The results show that a significant increase in the strength of the inclusion above the initial flow strength of the material improves the bendability of the material for a fixed inclusion size and location.

5.3.2 Effect of an inclusion on the bendability of a dual-phase material

The near surface distribution of $\bar{\varepsilon}$ on the tension side of a 90° V-bend specimen of a dual-phase steel with an inclusion of size, $r_I \approx 1.7 \times r_M$, strength, $\sigma_N \approx 0.7 \times \sigma_0^F$ (σ_0^F is the initial flow strength of the ferrite phase) and location, $dy = 0.125 \times d$, from the free surface at four values of ε_F together with the σ_F - ε_F response are shown in Fig. 5.5.

As shown in Figs. 5.5(a)-(c), the presence of an inclusion results in a sub-surface void nucleation ('white' region in the figures) and with progressive deformation $\bar{\varepsilon}$ localizes in a band emanating from the free surface that is oriented at an angle close to (but not at) 45° with respect to the loading axis. Also, with continued bending, the intensity of the localization of $\bar{\varepsilon}$ in the band increases, the sub-surface void starts to grow and a micro-crack nucleate at the free surface, Fig. 5.5(b). Subsequently, the sub-surface micro-crack connects with the surface micro-crack along the localization band of $\bar{\varepsilon}$, Figs. 5.5(c) and (d), resulting in final fracture at a distance d_x from the center of the specimen. The final fracture of the specimen leads to a drop in the value of σ_F, Fig. 5.5(e).

Next, a specimen with everything being the same as the specimen in Fig. 5.5 but with an inclusion of size, $r_I \approx 0.6 \times r_M$ was considered. The near surface distribution of $\bar{\varepsilon}$ on the tension side of this specimen at four values of ε_F together with the σ_F - ε_F response are shown in Fig. 5.6. As

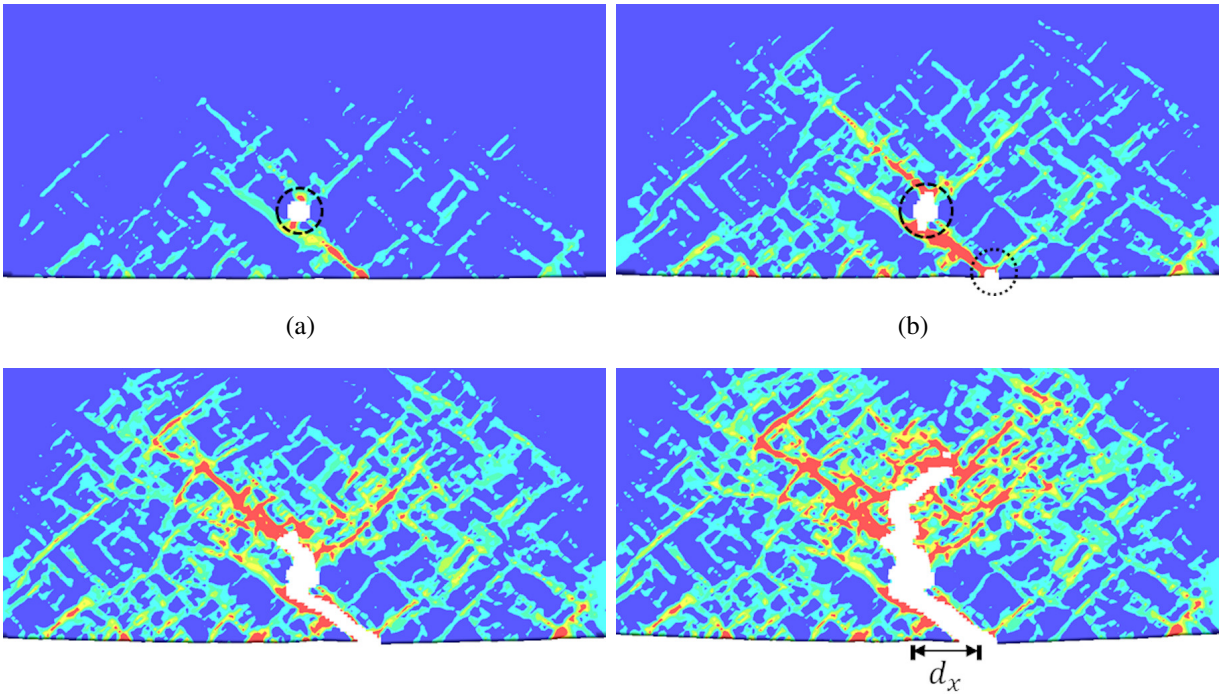

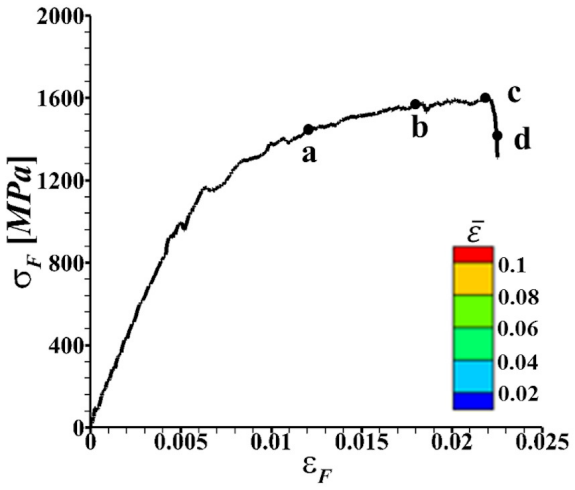

(e)

Figure 5.5: (a)-(d) The distribution of equivalent plastic strain, $\bar{\varepsilon}$, in the near surface region on the tension side of a deformed 90° V-bend specimen with 'discrete' dual-phase microstructure and an inclusion of size, $r_I \approx 3e$ ($r_I/r_M \approx 1.7$), strength, $\sigma_N = 300MPa$ ($\sigma_N/\sigma_0^F \approx 0.7$) and location, $dy/d = 0.125$, at four macroscopic flexural strain, ε_F, levels marked as, a-d, on the macroscopic flexural stress (σ_F) - strain (ε_F) curve in (e).

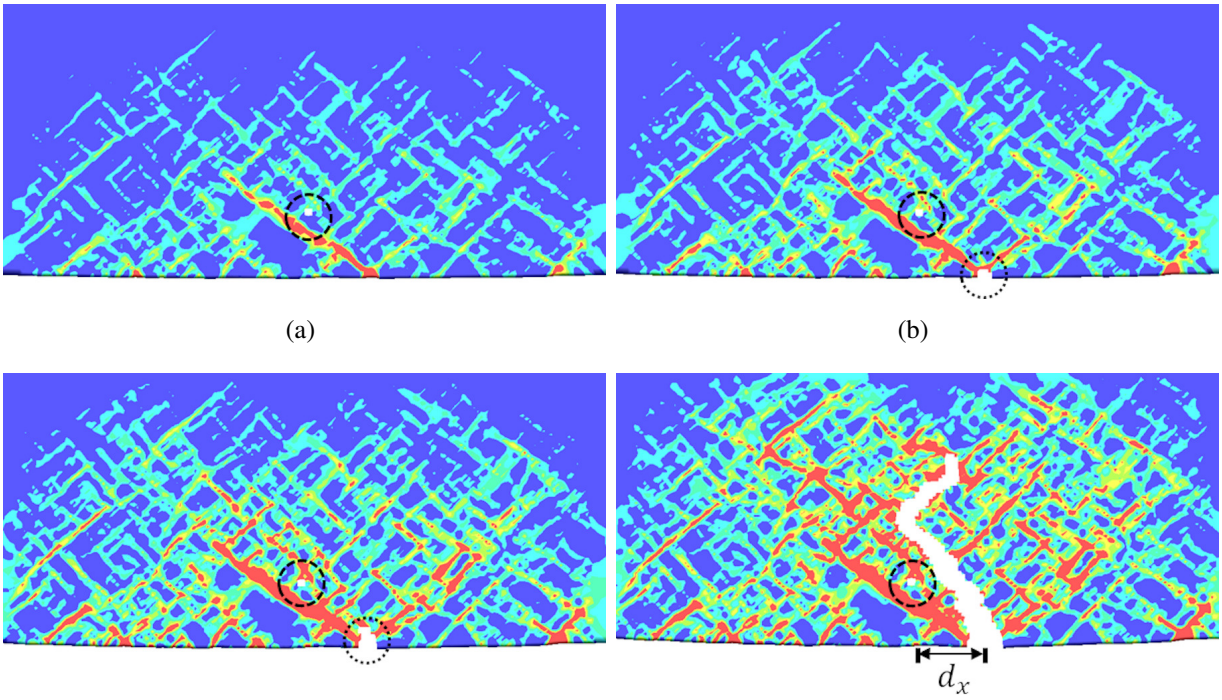

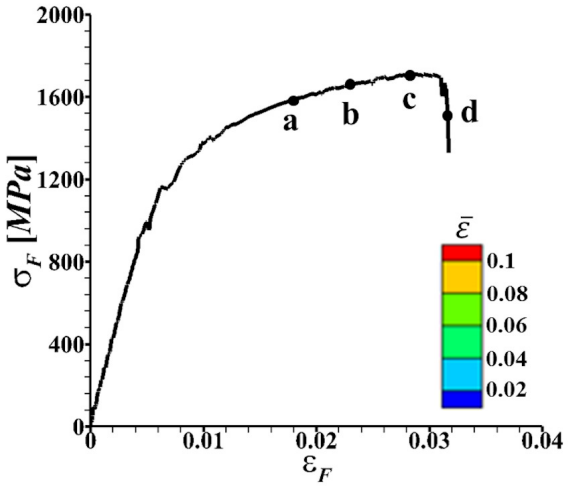

(e)

Figure 5.6: (a)-(d) The distribution of equivalent plastic strain, $\bar{\varepsilon}$, in the near surface region on the tension side of a deformed 90° V-bend specimen with 'discrete' dual-phase microstructure and an inclusion of size, $r_I \approx 1e$ ($r_I/r_M \approx 0.6$), strength, $\sigma_N = 300MPa$ ($\sigma_N/\sigma_0^F \approx 0.7$) and location, $dy/d = 0.125$, at four macroscopic flexural strain, ε_F, levels marked as, a-d, on the macroscopic flexural stress (σ_F) - strain (ε_F) curve in (e).

shown in Fig. 5.6(a), here as well, the sub-surface inclusion results in sub-surface void nucleation. However, the nucleated void doesn't significantly affect the localization of $\bar{\varepsilon}$ and the localization of $\bar{\varepsilon}$ predominantly depends on the interlacing of the length-scales induced by bending and the discreteness of the underlying dual-phase microstructure. With progressive deformation, the intensity of the localization of $\bar{\varepsilon}$ in the band increases and a surface micro-crack nucleates, while the inclusion induced sub-surface void doesn't grow significantly, Fig. 5.6(b)-(c). Subsequently, the surface micro-crack grows inwards while completely ignoring the inclusion induced sub-surface void, Fig. 5.6(d). The growth of the surface micro-crack results in final fracture i.e. drop in the value of σ_F, Fig. 5.6(e).

The effects of the inclusion size, r_I, location, dy/d, and strength, σ_N, on the bendability of the dual-phase steel with a sub-surface inclusion are shown in Fig. 5.7. As in Fig. 5.4, the bendability of a dual-phase specimen is characterized by the value of ε_F at failure, ε_f. The values of ε_f in Fig. 5.7 are normalized by the values of the macroscopic flexural strain to failure of the underlying inclusion free dual-phase steel microstructure, ε_f^0. For a fixed value of r_I, dy/d and σ_N of the inclusion, calculations are carried out for five underlying dual-phase steel microstructures taken from different locations of the dual-phase steel under consideration. The error bars in Fig. 5.7 are the standard error for five realizations of the underlying dual-phase steel microstructure.

As shown in Fig. 5.7(a), for an inclusion of strength, $\sigma_N = 300MPa$, which is less than the initial flow strength of both the ferrite and martensite phases, and a fixed size, the value of ε_f first increases with increasing value of dy/d and then tends to saturate. The saturation in the value of ε_f corresponds to $\varepsilon_f \rightarrow \varepsilon_f^0$, implying that the detrimental effect of the inclusion on the bendability of the dual-phase steel vanishes. The value of dy/d for which $\varepsilon_f \approx \varepsilon_f^0$ strongly depends on the inclusion size relative to the size of the martensite phase. For example, for inclusions of size, $r_I \approx 1.7 \times r_M$ and $2.8 \times r_M$, the values of dy/d for which $\varepsilon_f \approx \varepsilon_f^0$ are ≈ 0.3 and 0.44, respectively. While for an inclusion of size, $r_I \approx 0.6 \times r_M$, the value of dy/d for which $\varepsilon_f \approx \varepsilon_f^0$ is ≈ 0.125. The effect of the inclusion size and location on the bendability of a dual-phase steel shown in Fig. 5.7(a) is not significantly affected by an increase in the value of the inclusion strength

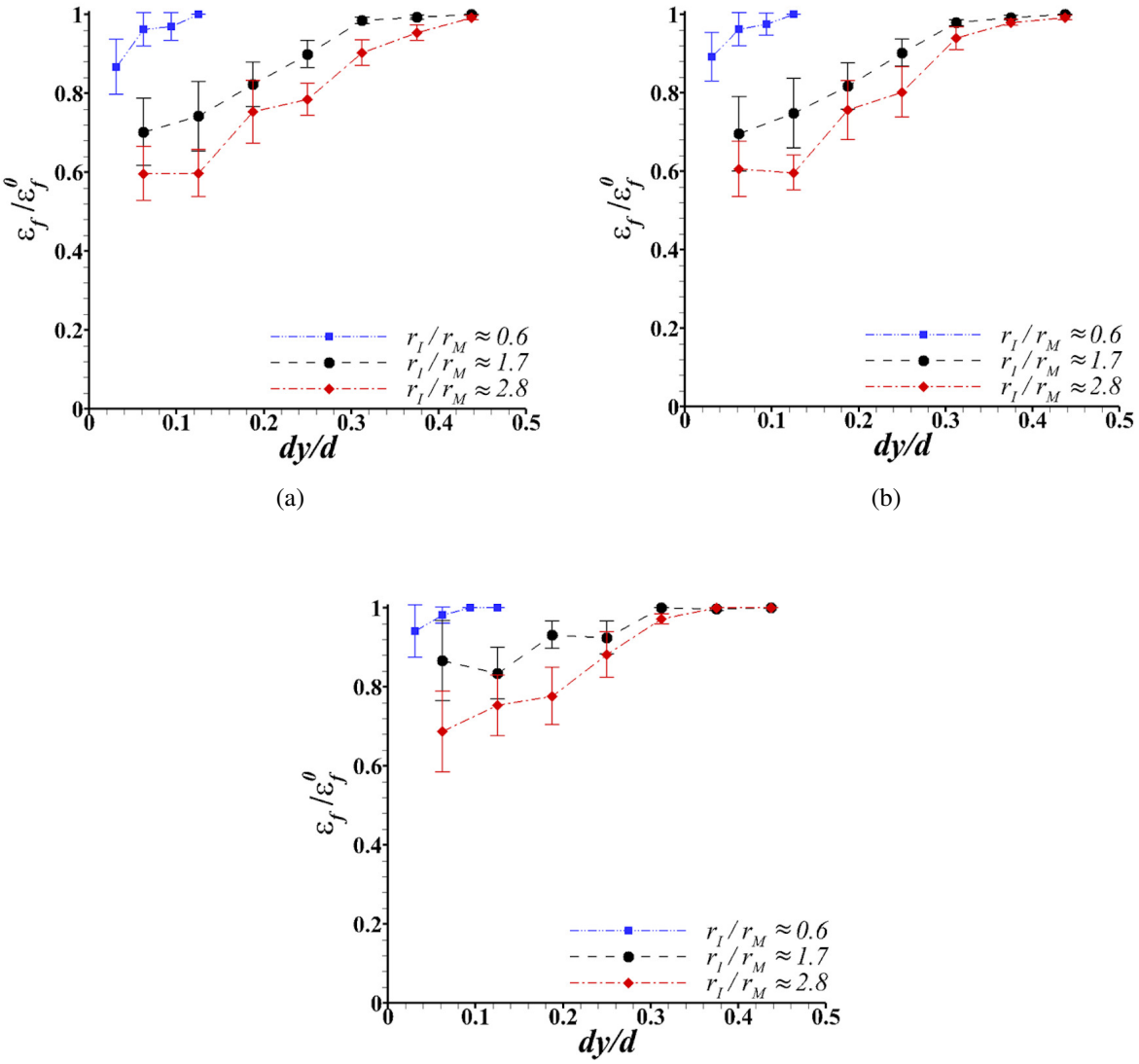

Figure 5.7: Effect of the size, r_I, and location, dy/d, of an inclusion of strength (a) $\sigma_N = 300MPa$ ($\sigma_N/\sigma_0^F \approx 0.7$ and $\sigma_N/\sigma_0^M \approx 0.2$), (b) $\sigma_N = 800MPa$ ($\sigma_N/\sigma_0^F \approx 1.9$ and $\sigma_N/\sigma_0^M \approx 0.6$) and (c) $\sigma_N = 1600MPa$ ($\sigma_N/\sigma_0^F \approx 3.7$ and $\sigma_N/\sigma_0^M \approx 1.1$) on the flexural strain to failure, ε_f, (i.e. bendability) of the dual-phase steel.

from $\sigma_N = 300MPa$ to $\sigma_N = 800MPa$, as shown in Fig. 5.7(b). The value of inclusion strength, $\sigma_N = 800MPa$, is greater than the initial flow strength of the ferrite phase but is less than the initial flow strength of the martensite phase. However, a further increase in the value of the inclusion

strength such that the inclusion is stronger than the martensite phase significantly improves the bendability of the dual-phase steel sheet for a fixed inclusion size and location, Fig. 5.7(c). A notable observation from Fig. 5.7(c) is that the detrimental effect of an inclusion which is smaller but stronger than the martensite phase on the bendability of a dual-phase steel is negligible. Finally, the error bars on the values of $\varepsilon_f/\varepsilon_f^0$ for a fixed inclusion size, location and strength in Fig. 5.7 highlight that the detrimental effect of an inclusion on the bendability of a dual-phase material is also sensitive to the variations in the underlying dual-phase microstructure.

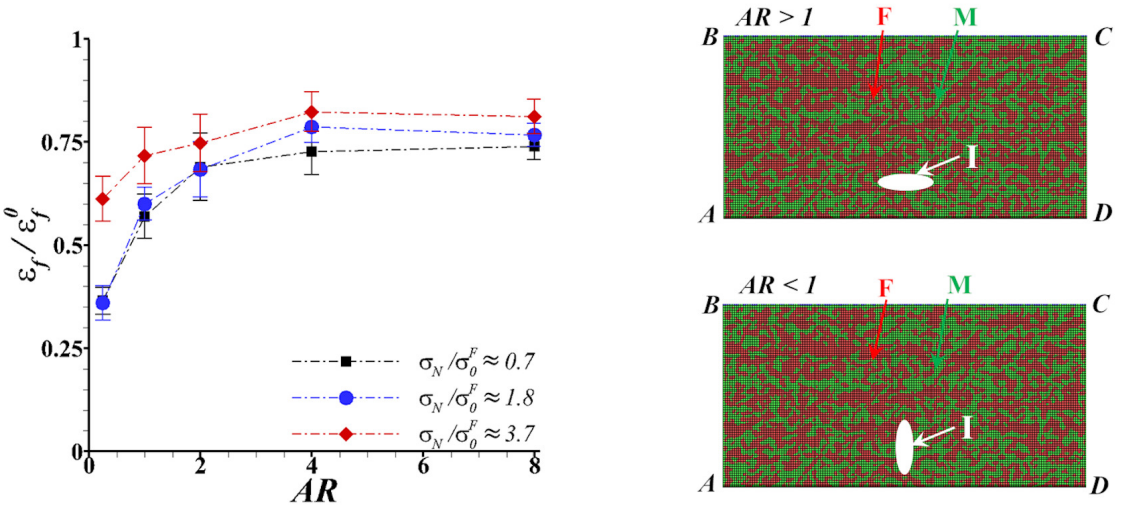

(a) (b)

Figure 5.8: (a) Effect of the aspect ratio (AR) of an elliptical inclusion on the flexural strain to failure, ε_f, (i.e. bendability) of the dual-phase steel. The cross-section area of the inclusion, $A \approx 25\pi e^2$ (giving $\sqrt{A}/2r_M \approx 2.5$), and the location of the inclusion center, $dy/d = 0.125$, is fixed for all the calculations in (a). (b) Schematic of elliptical inclusions with aspect ratio (AR) greater than (top) and less than (bottom) one.

Limited analyses of the effect of the shape of an inclusion on the bendability of the dual-phase steel have been analyzed. To this end, an elliptical inclusion has been modeled of size, r_I^x along the length and r_I^y along the thickness (loading direction) of the specimen. The cross-sectional area, $A = \pi r_I^x r_I^y$, of all the elliptical inclusions are taken to be $25\pi e^2$ (giving, $\sqrt{A}/2r_M \approx 2.5$) while

their aspect ratio, r_I^x/r_I^y are varied. The effect of the aspect ratio of an inclusion center located at $dy/d = 0.125$ on the normalized macroscopic flexural strain to failure, $\varepsilon_f/\varepsilon_f^0$, for three inclusion strength levels together with schematics of elliptical inclusions modeled are shown in Fig. 5.8. As shown in the figure, for all three inclusion strengths, the value of macroscopic flexural strain to failure, ε_f, increases with increasing aspect ratio of the elliptical inclusion for aspect ratios less than 4. While the detrimental effect of the aspect ratio of the elliptical inclusion on the bendability of the dual-phase steel vanishes for aspect ratios greater than 4. Similar to the results presented in Fig. 5.7, here as well, increasing the inclusion strength such that the inclusion is stronger than the martensite phase ($\sigma_N/\sigma_0^F \approx 3.7$ i.e. $\sigma_N/\sigma_0^M \approx 1.1$) improves the bendability of the dual-phase steel especially when the aspect ratio of the elliptical inclusion is less than 4.

5.4 Supervised machine learning approach and predictions

In the preceding section, the key results of the microstructure-based finite element calculations of the effect of an inclusion on ductile crack nucleation and early stage crack growth in single-phase and dual-phase materials under 90° V-bend loading condition were presented. The results show that the bendability of a material, in particular that of a dual-phase material, is greatly affected by the size, shape, location and strength of the 'unintended' inclusion as well as the underlying 'intended' dual-phase microstructure of the material. Thus, to quantify the effect of the multivariable input space associated with the 'intended' and 'unintended' microstructural features on the bendability of the advanced high strength dual-phase steel, supervised machine learning analysis have been carried out. The supervised machine learning approach and predictions of the effect of an inclusion on the bendability of the simple single-phase material is presented in Section 5.4.1. The approach and results of supervised machine learning on the effect of an inclusion on the bendability of more complex dual-phase material is presented in Section 5.4.2.

5.4.1 Effect of an inclusion on the bendability of a single-phase material

In the microstructure-based finite element calculations of the effect of an inclusion on the bendability of a simple single-phase material in Section 5.3.1, the effect of three features associated with

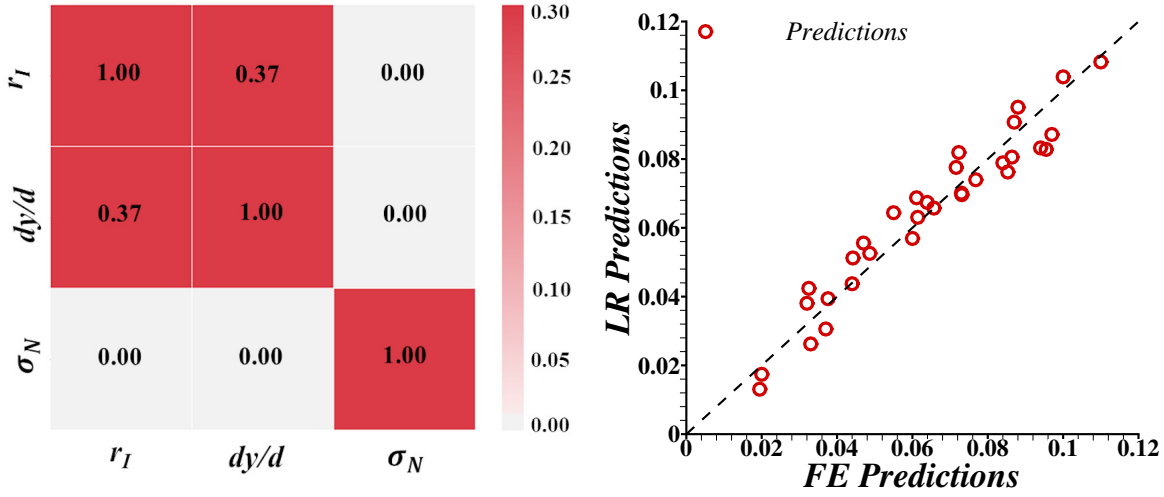

(a) (b)

Figure 5.9: (a) Correlation matrix of variables in analyzing the effect of an inclusion on the bendability of the single-phase material. (b) Comparison of the macroscopic flexural strain to failure, ε_f, predicted using linear regression (LR) analysis and finite element (FE) calculations.

an inclusion have been considered. These three features are, inclusion size, r_I, location, dy/d, and strength, σ_N. Thus, for supervised machine learning these three features are the input space while the macroscopic flexural strain to failure, ε_f, is the target or the output space. The goal of this exercise is to quantify the effect of the individual input variables on the response i.e. the value of ε_f and identify any redundancy in the input space. To this end, the simplest supervised machine learning approach, linear regression analysis has been chosen. The accuracy of the regression analysis is evaluated by the widely used performance measure [178], coefficient of determination, R^2. The R^2 is the proportion of the variance in the dependent variable that is predictable from the independent variable and is a statistical measure of how well the regression predictions approximate the real data. The value, $R^2 = 1$, indicates that the regression predictions perfectly fit the data.

The results of the linear regression analysis are shown in Fig. 5.9. The correlation matrix of the three input variables, r_I, dy/d and σ_N in Fig. 5.9(a) clearly shows that these three input variables are not highly correlated. A comparison of the predictions of the linear regression analysis and the

results of the microstructure-based finite element calculations are shown in Fig. 5.9(b). As shown in the figure, the two predictions are in very good agreement and the value of $R^2 \approx 0.93$. The final calibrated linear regression model follows:

$$\varepsilon_f = 6 \times 10^{-2} - 1.25 \times 10^{-2} r_I + 2.11 \times 10^{-1} \frac{dy}{d} + 8.7 \times 10^{-6} \sigma_N \tag{5.3}$$

The calibrated linear regression model in Eq. (5.3) shows that the inclusion size and location are the two important features that greatly affect the bendability of a simple single-phase material with a sub-surface inclusion. While the inclusion strength as a whole has a small effect on the bendability of a single-phase material.

5.4.2 Effect of an inclusion on the bendability of a dual-phase material

Next, the focus is on quantifying the effects of the multivariable input space associated with both the 'unintended' and 'intended' microstructural features on the bendability of the advanced high strength dual-phase steel using supervised machine learning. The results of the microstructure-based finite element calculations in Section 5.3.2 suggest that there are several features associated with an inclusion that affect the bendability of the material. While the results of the microstructure-based finite element calculations of the bendability of the dual-phase steel without any inclusion in Section 4 suggest that there are several additional features associated with the underlying dual-phase microstructure that affect the bendability of the material. In particular, in Section 4, it was found that the intrinsic bendability of a dual-phase steel (i.e. without inclusion) depends on the volume fraction of the martensite in a small region in the center of the specimen on the tension side, the volume fraction of the martensite in a small region at the fracture initiation site, and the distance between the center of the bend specimen (on the tension side) and the fracture initiation site. Apart from these, the effect of an inclusion, especially that of smaller size, on the bendability of the dual-phase steel may also depend on its neighboring phase i.e. does the inclusion entirely lie in the ferrite phase, martensite phase or it extends over both the phases. All the possible features associated with both the 'unintended' and 'intended' microstructural features that may affect the

Table 5.2: All the possible features identified from microstructure-based finite element calculations that may affect the bendability of the dual-phase steel with (in this work) and without (in Section 4) an inclusion.

Category	Features	Details
Inclusion	r_I^x	Size of inclusion along $x\text{-}axis$ (length)
	r_I^y	Size of inclusion along $y\text{-}axis$ (thickness)
	σ_N	Inclusion strength
	dy/d	Location of inclusion
	A_I	Area of inclusion ($A_I = \pi r_I^x \cdot r_I^y$)
Dual-phase microstructure	$(V_f^M)_N$	Volume fraction of the martensite phase in a small box of area $\approx 8r_M^2$ at the fracture initiation site
	$(V_f^M)_{CS}$	Volume fraction of the martensite phase in a small box of area $\approx 8r_M^2$ in the center of the specimen
	$(V_f^M)_{CL}$	Volume fraction of the martensite phase in a slightly larger box of area $\approx 32r_M^2$ in the center of the specimen
	Neighbor	Neighboring phase of the inclusion (ferrite, martensite or both)
	d_x	Projected distance between the center of the specimen and the location of crack initiation site

bendability of a dual-phase steel are given in Table 5.2.

The simple supervised machine learning approach, linear regression analysis, as in Section 5.4.1 to quantify the effect of all the input variables in Table 5.2 on the response i.e. normalized macroscopic flexural strain to failure, $\varepsilon_f/\varepsilon_f^0$, and identify any redundancy in the input space were considered at first. To this end, the results of 80% of $\approx$ 400 microstructural-based finite element calculations carried out in this work were randomly selected to train the linear regression model. The trained linear regression model was then tested on remaining 20% of the data set. The accuracy of the regression analysis was evaluated by two performance measures [178], coefficient of determination, R^2, as in Section 5.4.1 and mean squared error, MSE. MSE is the average of the squares of the errors and $MSE = 0$ indicates that the estimator predicts observations with perfect accuracy. However, not only the input space, Table 5.2, for dual-phase steel is significantly greater

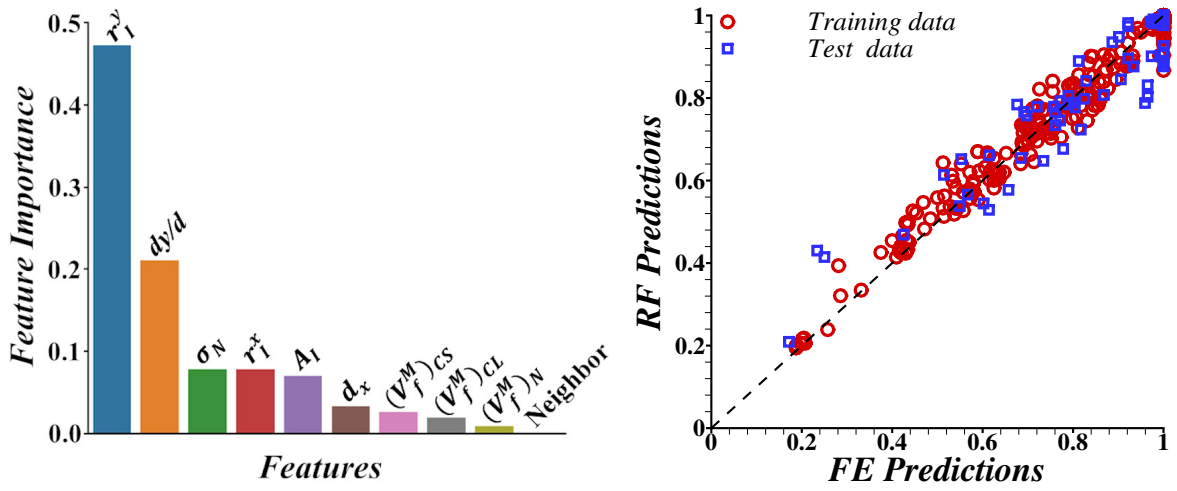

(a) (b)

Figure 5.10: (a) Feature importance obtained from the random forest regression analysis of the effect of an inclusion on the bendability of the dual-phase steel. (b) A comparison of the bendability, normalized macroscopic flexural strain to failure, $\varepsilon_f/\varepsilon_f^0$, obtained from random forest regression analysis using feature set 2 in Table 5.3 and microstructure-based finite element calculations of 90° V-bending of the dual-phase steel.

than the single-phase material, the effect of inclusion on the bendability of dual-phase steel is also extremely non-linear. Thus, due to these complexities, the trained linear regression model failed to reasonably predict the bendability of the test cases. The values of R^2 and MSE for the test cases were found to be 0.75 and 0.011, respectively.

Next, a more sophisticated supervised machine learning approach, random forest regression analysis, was chosen. The random forest supervised machine learning approach has been extensively applied for predictive analytics and is a type of additive model that makes predictions by combining decisions from a sequence of base models, see for example, [179–182]. In addition, the feature importance can be obtained by permuting the values of the input variables and measuring their impact on prediction accuracy. For regression, the variance of random forest model is the measure of impurity. Thus, when training a tree, it is possible to compute how much each feature decreases the impurity. The more a feature decreases the impurity, the more important is

Table 5.3: Feature reduction using random forest regression analysis of the effect of an inclusion on the bendability of the dual-phase steel. The description of all the features are given in Table 5.2. The value of R^2 is the coefficient of determination of the fit, MSE(CV) is the mean squared error of the cross-validation predictions, and MSE(Test) is the mean squared error of the test data.

Set	Features	R^2	MSE (CV)	MSE (Test)
1	All features	0.915	0.004	0.004
2	r_I^x, r_I^y , σ_N, dy/d, A_I, d_x, $(V_f^M)_{CS}$	0.919	0.004	0.004
3	r_I^x, r_I^y , σ_N, dy/d, A_I, d_x	0.909	0.004	0.004
4	r_I^x, r_I^y , σ_N, dy/d, A_I, $(V_f^M)_{CS}$	0.915	0.004	0.005
5	r_I^x, r_I^y , σ_N, dy/d, A_I	0.813	0.009	0.008

the feature. In random forests, the impact on impurity of each feature can be averaged across trees to determine the final importance of the variable. To avoid over-fitting and minimize the selection bias, 10-fold cross-validation scheme was chosen for regression analysis. While grid-search was used to find the optimal hyper-parameters of the random forest model that results in the most accurate predictions.

At first, building a random forest model with all 10 features listed in Table 5.2 and their importance is shown in Fig. 5.10(a). As shown in the figure, not all features have the same impact on the bendability of the dual-phase steel. The two most important features that greatly affect the bendability of the dual-phase steel are the inclusion size along the thickness of the sheet, r_I^y, and the location of the inclusion, dy/d. These two features are also the most important features that affect the bendability of the single-phase material. However, there are features associated with the 'intended' dual-microstructure such as projected distance between the center of the specimen and the location of the crack initiation site, d_x, and the volume fraction of the martensite in a small box in the center of the specimen, $\left(V_f^M\right)_{CS}$, that have small but significant impact on the bendability of the dual-phase steel. Thus, feature reduction were carried out by building random forest models using a sub-set of the features in Table 5.2 and rigorously testing their performance. The perfor-

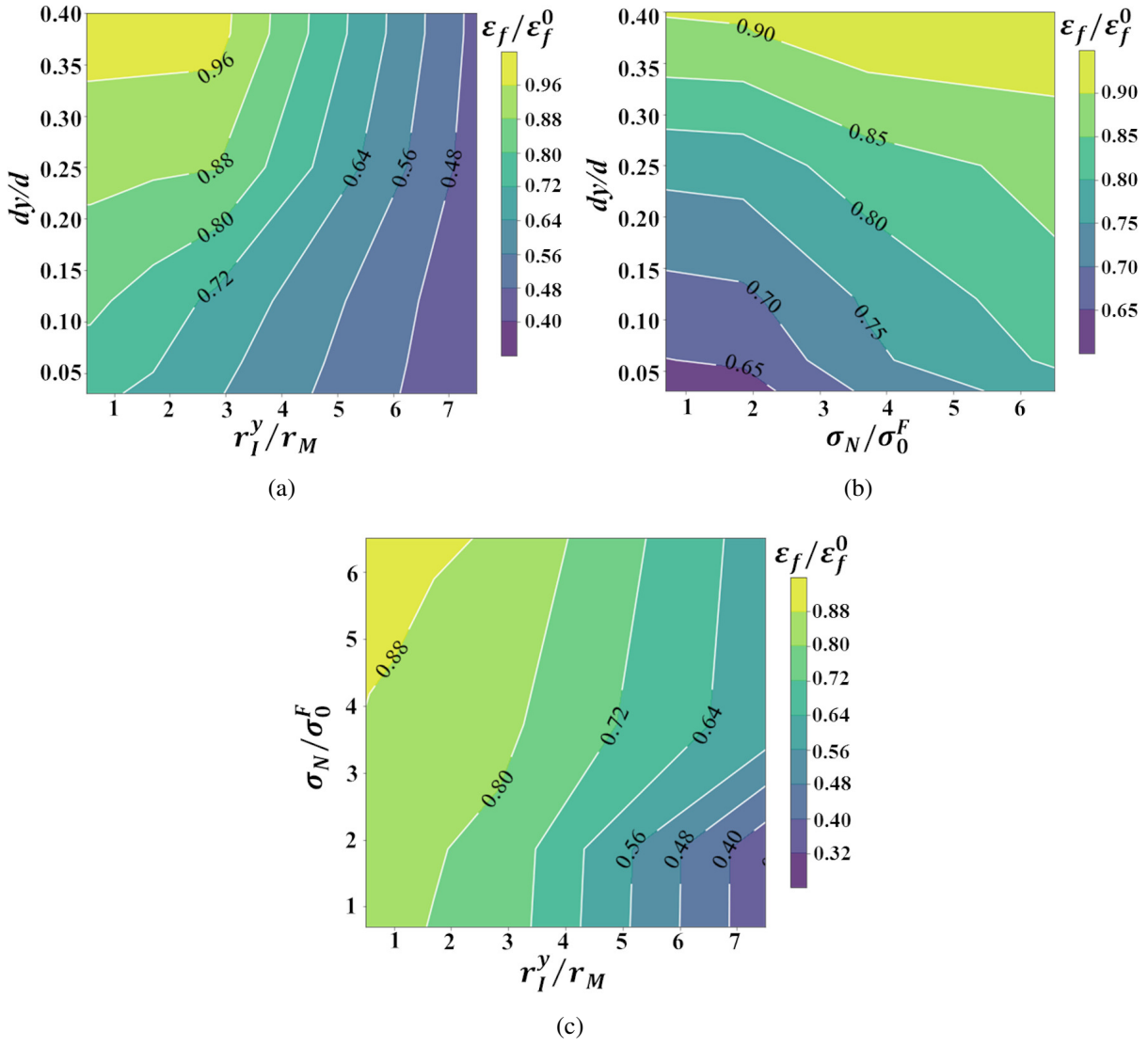

Figure 5.11: Partial dependence plots showing the effects of (a) normalized location, dy/d, and size, r_I^y/r_M, (b) normalized location, dy/d, and strength, σ_N/σ_0^F, and (c) normalized strength, σ_N/σ_0^F, and size, r_I^y/r_M, of the inclusion on the bendability i.e. the normalized macroscopic flexural strain to failure, $\varepsilon_f/\varepsilon_f^0$, of the dual-phase steel.

mance of the random forest model based on all the features as well as four example sub-sets of features are given in Table 5.3. As shown in Table 5.3, the performance of a random forest model built using the seven most important features, feature set 2, is the best. Among the seven features, five of them are associated with the inclusion and two are associated with the underlying dual-

phase microstructure. Note, that the performance of a random forest model built using only the features associated with the inclusion, feature set 5, is the worst. A comparison of the bendability, normalized macroscopic flexural strain to failure, $\varepsilon_f/\varepsilon_f^0$, obtained from the random forest model built using the feature set 2 in Table 5.3 and microstructure-based finite element calculations of 90° V-bending of the dual-phase steel is shown in Fig. 5.10(b). A good correlation between the predictions of the random forest machine learning model and the microstructure-based finite element calculations in Fig. 5.10(b) is noted.

With the trained random forest machine learning model (with feature set 2 in Table 5.3 as input space and corresponding values of $\varepsilon_f/\varepsilon_f^0$ as output space) at hand, the partial dependence of few key features on the bendability ($\varepsilon_f/\varepsilon_f^0$) of the dual-phase steel have been analyzed. The partial dependence plots allow to visualize the marginal effect of select features at a time on the predicted outcome [183]. The partial dependence function is given as:

$$\hat{f}_{x_S}(x_S) = E_{x_C}\left[\hat{f}(x_S, x_C)\right] = \int \hat{f}(x_S, x_C) d\mathbb{P}(x_C) \tag{5.4}$$

with, x_S being the features for which the partial dependence function is sought and x_C are the other features of the input space used in the machine learning model, $\hat{f}$. The partial dependence works by marginalizing the output of the machine learning model over the distribution of the features in the set x_C, so that the function highlights the correlation between the features of interest i.e. the feature set x_S and the predictions. The partial function, $\hat{f}_{x_S}$, is estimated by calculating averages in the training data (also referred to as Monte Carlo Method):

$$\hat{f}_{x_S}(x_S) = \frac{1}{n}\sum_{i=1}^{n} \hat{f}(x_S, x_C^{(i)}) \tag{5.5}$$

where, $x_C^{(i)}$ are the values of the features from the dataset and n is the number of instances in the dataset.

The partial dependence plots visualizing the effects of a combination of two features associated with the inclusion on the bendability (values of $\varepsilon_f/\varepsilon_f^0$) of the dual-phase steel are shown in

Fig. 5.11. These plots clearly highlight the extremely non-linear and oftentimes discrete effect of individual features associated with the inclusion on the bendability of the dual-phase steel. The partial dependence plot in Fig. 5.11(a) shows that the detrimental effect of a smaller inclusion decreases rapidly as the distance of the inclusion from the free surface increases. However, the detrimental effect of a relatively larger inclusion is rather insensitive to its location. The partial dependence plot in Fig. 5.11(b) shows that the detrimental effect of an inclusion that is close to the free surface decreases with increasing inclusion strength for inclusion strength sufficiently greater than the strength of the ferrite phase. While the effect of an inclusion that is located far away from the free surface is rather insensitive to the inclusion strength. Similarly, the partial dependence plot in Fig. 5.11(c) shows that the detrimental effect of a large inclusion decreases with increasing inclusion strength but that of a small inclusion is relatively insensitive to the inclusion strength.

5.5 Discussion

An imposed three-point bending like deformation, such as 90° V-bending on the specimen of a single-phase isotropic elastic-plastic material induces a single length-scale. This results in a smooth gradient in the distribution of the plastic strain, $\bar{\varepsilon}$, with the value of $\bar{\varepsilon}$ being greater at the free surface close to the center of the specimen along the length direction, Section 4. Even in this simple problem, introducing a single sub-surface inclusion in the material induces another (microstructure-based) length-scale. The interaction of the length-scales induced by the mode of deformation and the microstructure greatly affects the deformation pattern as well as damage nucleation and evolution in the material. The results show that the sub-surface void nucleation due to the presence of the inclusion in a single-phase material under 90° V-bending results in plastic strain localization in bands. These bands emanate from the sub-surface void and are oriented at $\approx 45^\circ$ with respect to the loading axis. Next, with continued bending the ligament between the surface and the sub-surface void parallel to the loading axis undergoes ductile fracture post-localized thinning.

Unlike a single-phase material, in a specimen of a dual-phase steel, 90° V-bending induces one length-scale, while the discreteness of the underlying dual-phase microstructure induces another

length-scale(s). The interlacing of these length-scales results in an overall gradient in the distribution of $\bar{\varepsilon}$ with the value of $\bar{\varepsilon}$ being greater at the surface and within this overall gradient the value of $\bar{\varepsilon}$ is greater in the soft ferrite phase, Section 4. Also, due to the local constrained imposed by the distribution of the hard martensite phase, the value of the stress triaxiality is greater in the soft ferrite phase close to ferrite-martensite interface [48]. Next, the presence of a sub-surface inclusion in the dual-phase microstructure may induce yet another length-scale(s) and the interlacing of all these length-scales greatly affects the distribution of $\bar{\varepsilon}$ as well as the crack nucleation and growth in the specimen. Specifically, in a bend specimen of a dual-phase steel with a sub-surface inclusion of size sufficiently greater than the martensite phase and/or located rather close to the free-surface, the distribution of $\bar{\varepsilon}$ localizes in an inclined band emanating from the free-surface towards the sub-surface void nucleated at the inclusion. Finally, with continued bending ductile fracture occurs along the localization band. However, in a bend specimen of a dual-phase steel with a sub-surface inclusion of size comparable to (or less than) the martensite phase and/or located sufficiently away from the free-surface, the localization band of $\bar{\varepsilon}$ emanating from the free-surface ignores the sub-surface void nucleated at the inclusion. Under these circumstances the detrimental effect of the presence of an inclusion is negligible and the bendability of the specimen is largely dictated by the underlying dual-phase microstructure of the material.

The results of the parametric studies show that for a fixed inclusion size and location, and other material properties, the effect of the strength of the inclusion on the bendability of both single-phase and dual-phase materials is somewhat discrete. For instance, the strength of the inclusion does not significantly affect the bendability of a single-phase material as long as the strength is less than or comparable to the flow strength of the material. Similarly, the strength of the inclusion does not significantly affect the bendability of a dual-phase material as long as the strength is less than or comparable to the flow strength of the martensite phase. Although not present here, parametric studies to explore the effects of elastic properties of the inclusion on the bendability of the dual-phase steel were carried out. To this end, calculations were carried out for three values of the Young's modulus, $E = 150GPa$, $300GPa$ and $450GPa$, and two values of the Poisson's

ratio, $\nu = 0.2$ and 0.3 of the inclusion. The results show that for the range of the values of E and ν considered, the elastic properties of an inclusion of strength less than or comparable to the flow strength of the martensite phase does not significantly affect the bendability of the dual-phase steel.

Furthermore, the supervised machine learning based analysis helped unravel the effect of the multivariable input space affecting the bendability of the single-phase and dual-phase materials. In particular, the machine learning based analysis shows that the inclusion size and location, and (to an extent) strength of the inclusion are the key features that affect the bendability of a simple single-phase material with a sub-surface inclusion. On the contrary, the effect of an inclusion on the bendability of the dual-phase steel is more complex. The machine learning based analysis clearly highlight the extremely non-linear and oftentimes discrete effect of the individual features associated with the inclusion on the bendability of the dual-phase steel. The machine learning based analysis also shows that the bendability of a dual-phase steel is not only affected by the size, shape, location and (to an extent) strength of the sub-surface inclusion but it is also affected by the underlying dual-phase microstructure.

The bendability of a sheet metal via industrial scale 90° V-bend test is characterized by visually inspecting the tension side of the deformed specimen for the presence of cracks, Fig. 5.12(a). A specimen passes the bend test, if no crack is observed while a specimen fails the bend test, if a crack is observed post 90° V-bending. As shown in Fig. 5.1(d), the 90° V-bendability of a galvannealed dual-phase, DP1000, steel sheet was correlated with the size and location of the inclusions in the specimens through detailed post-mortem analysis. Although the focus is to develop a fundamental understanding of the effects of the length-scales induced by bending, dual-phase microstructure and inclusion on the ductile fracture of the dual-phase steel, the question arises to the extent to which the results provide physically realistic predictions. There are two basic limitations of the microstructure-based finite element calculations that prohibit from directly comparing the predictions with the experimental results shown in Fig. 5.1(d). First, the dual-phase microstructure and the inclusion modeled in the plane strain slice of the material, Fig. 5.2, is essentially

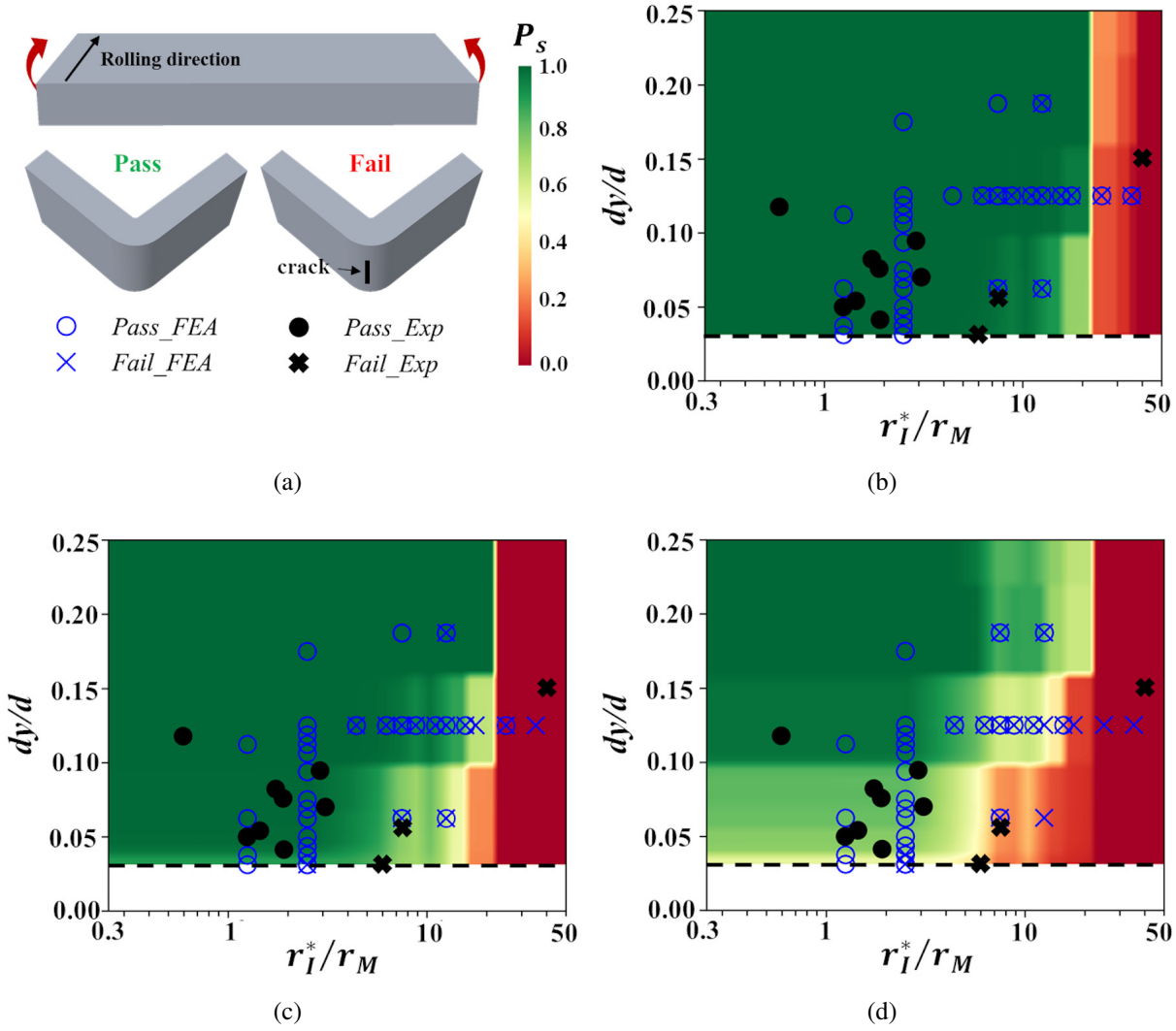

Figure 5.12: (a) Schematic of a bend specimen, and examples of 'pass' and 'fail' characterization during $90°$ V-bend tests. (b)-(d) The effect of the normalized location, dy/d, and normalized size, r_I^*/r_M, of the sub-surface inclusion on the bendability of an advanced high strength, DP1000, dual-phase steel as characterized by $90°$ V-bend tests (Exp), and as predicted by microstructure-based finite element calculations (FEA) and supervised machine learning model (contour plot of the probability of survival, P_s). In the finite element calculations and machine learning model, a dual-phase steel specimen with an inclusion passes the bend test if the value of the normalized macroscopic flexural strain to failure, (b) $\varepsilon_f/\varepsilon_f^0 \geq 0.6$, (c) $\varepsilon_f/\varepsilon_f^0 \geq 0.7$ or (d) $\varepsilon_f/\varepsilon_f^0 \geq 0.8$.

two-dimensional. Second, the constitutive parameters associated with the damage model for the constituent phases are not calibrated for the dual-phase steel under consideration but are assigned values that artificially accelerate the damage process in the material to achieve numerical results

within a reasonable time. To overcome the first limitation, scaling the size of the inclusion modeled as $r_I^* = 5 \times r_I^y$ following the works of [104, 140] to approximate the size of an inclusion in the three-dimensional bend specimen. Next, to overcome the second limitation, defining a simple criteria i.e. a specimen passes the bend test if the value of the normalized macroscopic flexural strain to failure, $\varepsilon_f/\varepsilon_f^0$, is greater than or equal to a critical value, c.

Figures 5.12(b)-(d) show the effect of the location, dy/d, and size, r_I^*/r_M, of a sub-surface inclusion on the bendability of the dual-phase steel as characterized by 90° V-bend tests (Exp) and as predicted by the microstructure-based finite element calculations (FEA) considering the values of $c = 0.6$, 0.7 and 0.8, respectively. In Figs. 5.12(b)-(d), finite element results corresponding to a range of values of the inclusion strength and aspect ratio, as well as multiple realizations of the underlying dual-phase microstructures are superimposed on top of each other in the dy/d versus r_I^*/r_M space. The contour plots in Figs. 5.12(b)-(d) are the probability of survival, P_s, as a function of dy/d and r_I^*/r_M obtained from the trained supervised machine learning model. The value of P_s is estimated as,

$$P_s = \frac{1}{N}\sum_{i=1}^{N} P_i, \quad P_i = \begin{cases} 1, & \varepsilon_f/\varepsilon_f^0 \geqslant c \\ 0, & \varepsilon_f/\varepsilon_f^0 < c \end{cases} \tag{5.6}$$

where, N is the total number of samples with fixed set of values of dy/d and r_I^*/r_M. For a fixed set of values of dy/d and r_I^*/r_M, $N = 5000$ random samples are analyzed with the values of the remaining parameters of the feature set 2 in Table 5.3 lying within a lower and an upper bound ($0.7 \leq \sigma_N/\sigma_0^F \leq 6.7$, $0.06 \leq r_I^x/r_M \leq 11.4$, $0.05 \leq \sqrt{A}/2r_M \leq 10.1$, $0 \leq d_x/d \leq 0.28$, $0.4 \leq (V_f^M)_{CS} \leq 0.6$). The results presented in Figs. 5.12(b)-(d), clearly highlight the strong and somewhat discrete inclusion size effect on the bendability of the dual-phase advanced high strength steel. Also, very good correlation between the predictions and the limited experimental results with $c = 0.7$ in Fig. 5.12(c) is noted.

5.6 Conclusions

Microstructure-based finite element calculations were carried out to understand the effect of the length-scales induced by the mode of deformation i.e. 90° V-bending, 'intended' dual-phase ferritic-martensitic microstructure, and 'unintended' microstructural features i.e. inclusions on ductile crack nucleation and early stage crack growth in an advanced high strength dual-phase steel. In the calculations, the inclusion modeled was always located in the center along the length of the bend specimens and parametric studies were carried out to explore the effects of inclusion size, shape, location (along the thickness of the specimen) and strength on the bendability of the dual-phase steel. In line with the experimental observations, strong inclusion size effects on the bendability of the dual-phase steel naturally emerge in the calculations. The effect of the multivariable input space associated with both the 'intended' and 'unintended' microstructural features on the bendability of the dual-phase steel were also quantified using supervised machine learning. The supervised machine learning approach used here utilized an ensemble learning method for classification and regression. For the purpose of comparison and to gain additional insight, the effect of an inclusion on the bendability of a single-phase material with constitutive parameters corresponding to the overall 'homogenized' dual-phase steel under consideration were also analyzed.

The key conclusions are as follows:

1. A sub-surface void nucleation at an inclusion in a single-phase material under 90° V-bending results in plastic strain localization in bands emanating from the sub-surface void that are oriented at $\approx 45^\circ$ with respect to the loading axis. Finally, with continued bending the ligament between the surface and the sub-surface void parallel to the loading axis undergoes ductile fracture post-localized thinning.

2. The micro-mechanism of ductile fracture in a dual-phase steel with a sub-surface inclusion under 90° V-bending not only differs from that in a single-phase material but also strongly depends on the inclusion size and location:

   (a) In a dual-phase steel with a sub-surface inclusion of size sufficiently greater than the

martensite phase and/or located rather close to the free-surface, plastic strain localizes in an inclined band emanating from the free-surface towards the sub-surface void nucleated at the inclusion. Finally, with continued bending ductile fracture occurs along the localization band.

(b) In a dual-phase steel with a sub-surface inclusion of size comparable to (or less than) the martensite phase and/or located sufficiently away from the free-surface, plastic strain localizes in inclined bands emanating from the free-surface that ignore the sub-surface void nucleated at the inclusion. Finally, with continued bending ductile fracture occurs along the localization band while ignoring the sub-surface void nucleated at the inclusion.

3. The supervised machine learning analysis revealed that unlike a single-phase material, the bendability of a dual-phase steel with a sub-surface inclusion is not only affected by the features associated with the inclusion but also by the features associated with the underlying dual-phase microstructure.

4. The results show that there exists a critical size of the inclusion relative to the size of the martensite phase below which the detrimental effect of the inclusion on the bendability of a dual-phase steel vanishes.

6. HIGH FRACTURE TOUGHNESS MICRO-ARCHITECTURED MATERIALS*

6.1 Background

The demand for lower fuel consumption and CO_2 emission while increasing the safety and reliability in the transportation and aerospace industries have driven the development of new lightweight materials with high strength and fracture toughness. Accordingly, the number of materials has increased dramatically: there are now over 120,000 different materials [184]. But is there still room for further improvement? To answer this question, it is insightful to consider material property charts [184], with axes in the form of material properties. For example, a chart of fracture toughness versus density is shown in Fig. 6.1(a), and one of fracture toughness versus compressive strength is shown in Fig. 6.1(b). Metals are clearly the toughest materials, but they are also the heaviest, Fig. 6.1(a). The choice of lightweight materials is limited: only foams, natural materials and a few elastomers and polymers have density less than water (1000kg/m^3). The scarcity of lightweight materials is emphasized in Fig. 6.1(b), where solids with density less than 1000kg/m^3 are highlighted. Among these lightweight materials, wood and bamboo offer the best combination of fracture toughness and strength. This raises an important question: how can the current material space be extended? Here, the possibility of achieving lightweight, high fracture toughness and high strength by the design of micro-architectured materials were explored.

The potential of micro-architectured and lattice materials to combine high stiffness and strength at low densities is well documented, see for example, [5–7, 185–187]. However, less is known about their capacity for high fracture toughness at low density. Experimental, analytical and numerical studies [188–194] have shown that the mode I fracture toughness, K_{IC}, of two-dimensional micro-architectured materials made from an elastic-brittle material of fracture strength, σ_f, can be expressed as:

*Reprinted with permission from "High fracture toughness micro-architectured materials" by **Liu, Y.**, St-Pierre, L., Fleck, N.A., Deshpande, V.S. and Srivastava, A., 2020. *Journal of the Mechanics and Physics of Solids*, *in press*, Copyright 2020 by Elsevier.

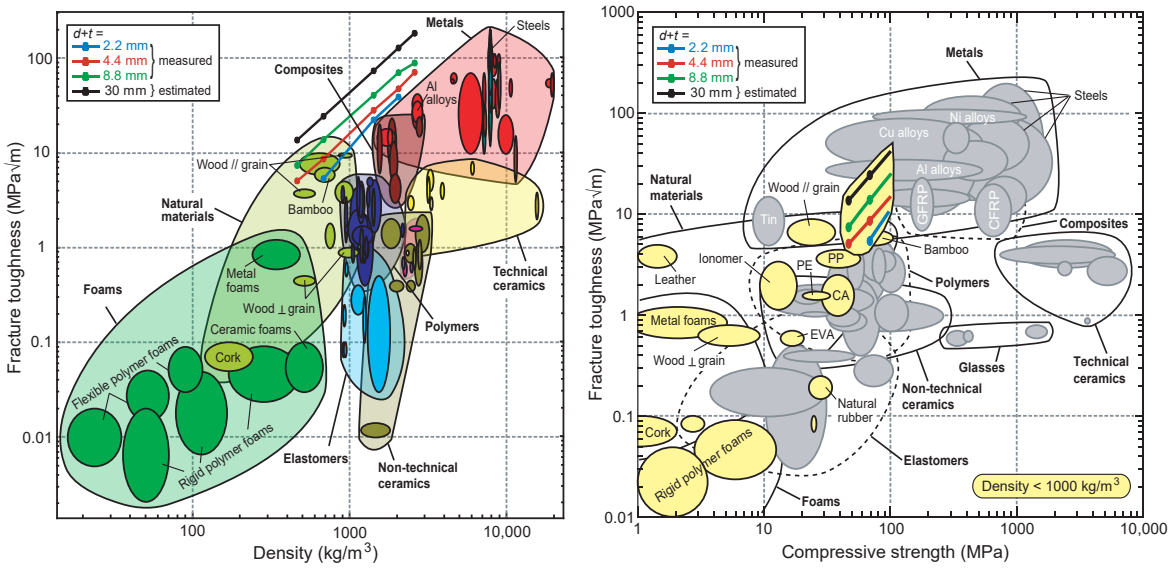

(a) (b)

Figure 6.1: Material property charts of (a) fracture toughness versus density and (b) fracture toughness versus compressive strength. The properties of micro-architectured materials consisting of hexagonal array of holes with hole spacing $d + t$, manufactured and tested in this work and the estimated properties of a micro-architectured material with $d+t = 30$mm are also shown for comparison. The abbreviations are CA: cellulose polymer; EVA: ethylene vinyl acetate; PE: polyethylene; PP: polypropylene; CFRP: carbon fiber reinforced polymer; GFRP: glass fiber reinforced polymer. In (b) materials with density less than 1000kg/m^3 are shaded in yellow.

$$K_{IC} = H\sigma_f \bar{\rho}^h \sqrt{l} \tag{6.1}$$

where $\bar{\rho}$ and l are the relative density and cell size of the micro-architectured material, respectively, and H and h are constants dependent upon the topology of the micro-architectured material. Numerical results of [195] and experimental results of [9] suggest that Eq. (6.1) can also be applied to ductile micro-architectured materials made from an elastic-plastic material. However, these studies only considered micro-architectured materials of low relative density, $\bar{\rho} \lessapprox 0.2$. Here, fracture toughness tests on ductile micro-architectured materials with a wide range of relative densities, $0.17 \leq \bar{\rho} \leq 0.95$ were presented. Micro-architectured materials can achieve a higher fracture toughness than that of the parent solid. Thus, micro-architectured materials can have a

combination of properties that outperform other engineering and natural materials, Fig. 6.1.

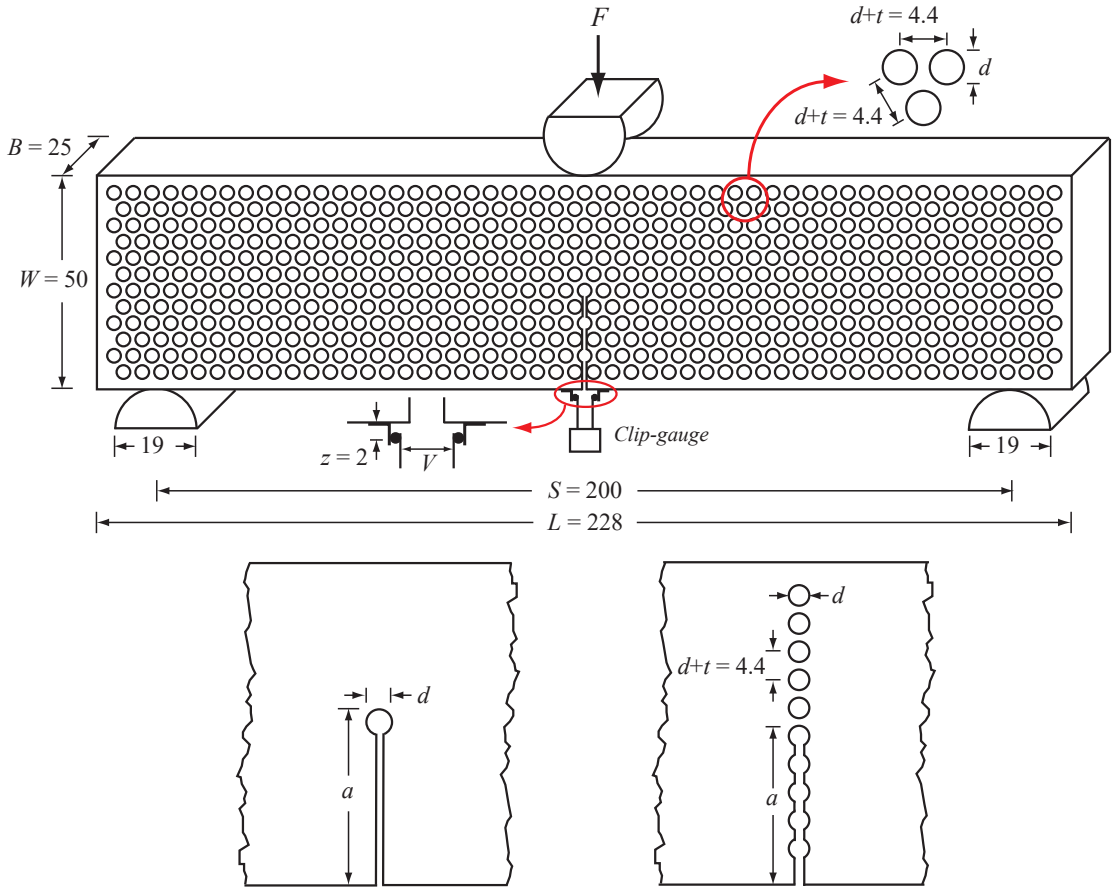

Figure 6.2: Schematic showing a single-edge notch specimen of a micro-architectured material consisting of a hexagonal array of holes drilled in a plate of an aluminum alloy and subjected to the three-point bending fracture test. Two simpler geometries, a single hole (bottom left) and a row of holes (bottom right) ahead of the initial crack were also tested to get more insight into the crack growth mechanisms in the micro-architectured material. For simplicity, only the central portion of the simpler geometries are shown but they had the same dimensions as the micro-architectured material. All dimensions in the figure are in mm.

A schematic of the micro-architectured material considered in this work that comprise a hexagonal array of holes drilled in the plates of an aluminum alloy is shown in Fig. 6.2. The relative density of the micro-architectured material is given by:

$$\bar{\rho} = 1 - \frac{\sqrt{3}\pi d^2}{6(d+t)^2} \tag{6.2}$$

where d is the hole diameter and $d + t$ is the hole spacing. First, varied the hole diameter while keeping the hole spacing fixed at $d + t = 4.4$mm. Five specimens with $d = 4.2,\ 4.0,\ 3.2,\ 2.3$ and 1.0mm corresponding to $\bar{\rho} = 0.17,\ 0.25,\ 0.52,\ 0.75$ and 0.95, respectively were tested. Second, the effect of the hole spacing on the fracture toughness by testing micro-architectured materials that are geometrically similar but half in size ($d + t = 2.2$mm) or double in size ($d + t = 8.8$mm) were investigated.

For the micro-architectured material in Fig. 6.2, it can be hypothesized that the fracture toughness is governed by the two competing mechanisms: crack blunting and hole-hole interaction. *Crack blunting*: the holes will blunt the crack-tip and consequently, expecting the fracture toughness to increase with increasing hole diameter [138, 196, 197]. *Hole-hole interaction*: consider the case of multiple holes with a fixed spacing $d + t$. Increasing the hole diameter d reduces the wall thickness t and as a result, expecting the fracture toughness to decrease with increasing hole diameter. To investigate these two mechanisms independently, tests on two simpler geometries were also conducted. First, the toughening effect of crack blunting was quantified by testing specimens with a single hole at the crack-tip (Fig. 6.2 bottom left). Then, the second mechanism, hole-hole interaction, was introduced by testing specimens with a single row of holes (Fig. 6.2 bottom right). Specimens with a single hole and those with a row of holes had the same overall dimensions as the specimens of the micro-architectured material to allow comparison between the three types of specimens. All tests were done on single-edge notch specimens loaded under three-point bending as shown in Fig. 6.2. The geometry and dimensions of the specimen, and the test procedure utilized are in compliance with the ASTM standard test method for measurement of fracture toughness [14].

Although the fracture tests of micro-architectured materials are carried out in compliance with the ASTM standard [14]. Is a standard test procedure that was initially established for specimens of bulk materials also applicable to micro-architectured materials? To gain additional insight, finite

element calculations of ductile fracture in the specimens of the micro-architectured materials and in specimens with a single and a row of holes using a constitutive framework for progressively cavitating ductile solids were carried out. In the finite element calculations, the fracture toughness of single-edge notch specimens subjected to three-point bending are evaluated using a procedure that mimics the ASTM standard [14] and also via direct computation of the J-integral. The fracture toughness computed from the finite element calculations using both the procedures are found to be consistent with the experimental results. In addition, the finite element calculations of ductile fracture in micro-architectured materials are also carried out for single-edge notch specimens subjected to tensile loading; the same scaling between fracture toughness and relative density of the micro-architectured materials is predicted for the tensile tests and three-point bending tests. Consequently, the fracture toughness of the micro-architectured materials measured here can be treated as a material property.

6.2 Experimental method

All specimens were made from aluminum alloy 6082-T6. The single-edge notch specimens were of length, $L = 228$mm, width, $W = 50$mm and thickness, $B = 25$mm (see Fig. 6.2), in compliance with [14]. The three types of specimens were manufactured following the same procedure. First, rectangular blocks of dimensions $L \times W \times B$ were machined from a plate. Second, the holes were drilled using a Computer-Numerically-Controlled (CNC) machine. Third, the initial crack was cut using Electrical Discharge Machining (EDM) with a wire diameter of 0.3mm.

The specimens were tested in three-point bending with a span $S = 4W = 200$mm, Fig. 6.2. Steel rollers of diameter of 19mm were used to provide simple support and for load introduction at mid-span. The tests were done with a screw-driven test machine at a constant cross-head displacement rate of 0.1mm/min. The force, F, applied at mid-span was measured by the load-cell of the test machine and the crack mouth opening displacement (CMOD) was measured by a clip-gauge. The clip-gauge was held in place by anvils of height $z = 2$mm as shown schematically in Fig. 6.2. Consequently, the extension measured by the clip-gauge, V, is related to CMOD using

the relation [198]:

$$\text{CMOD} = \frac{r_p(W-a)+a}{r_p(W-a)+a+z}V \tag{6.3}$$

where the plastic rotational factor $r_p = 0.44$, the width of the specimen $W = 50$mm and the crack length is a.

The $J-R$ curve was evaluated using the elastic compliance method [14]. This procedure was applied directly for tests done on specimens with a single hole. However, for specimens with a row of holes and hole diameter exceeding 1mm the relation between the elastic compliance and the crack length was inaccurate and alternatively empirical relations were derived as follows. First, the crack length, a, was measured with a vernier. Second, the crack mouth elastic compliance, C, was measured using the same experimental setup as that used for the fracture toughness test, Fig. 6.2. Next, ten measurements of the elastic compliance were taken and the mean was calculated. Finally, the ligament ahead of the crack tip was cut with a hacksaw to extend the crack length by $\Delta a = d + t = 4.4$mm and the procedure was repeated for this new value of crack length to obtain a relation between normalized crack length, a/W, and normalized elastic compliance, $\bar{C} = \left(2\sqrt{BWEC/S}+1\right)^{-1}$, where E is the Young's modulus. Note that the normalized elastic compliance, $\bar{C}$, is the same non-dimensional group as employed in [14]. For specimens of micro-architectured material, there was a load-drop following the fracture of a cell wall and the current crack length was directly inferred (and confirmed by visual inspection).

The stress intensity factor is related to the J-integral by [138]:

$$K_J = \sqrt{E'J} \tag{6.4}$$

where $E' \equiv E/(1-\upsilon^2)$ is the plane strain Young's modulus. For single hole specimens and those with a row of holes, the Young's modulus, $E = 70$GPa, and the Poisson's ratio, $\upsilon = 0.33$, are the material properties of aluminum alloy 6082-T6. In contrast, for micro-architectured materials, E' was taken as the effective plane strain Young's modulus of the micro-architectured material and

was evaluated from the elastic unloading compliance of the single-edge notch bend specimens. Furthermore, to visualize the path and shape of the crack, partially fractured specimens of micro-architectured materials were also analyzed using scanning electron microscope (SEM) and X-ray tomography.

For comparison purposes, the deformation and fracture response of the as-received plates of the solid aluminum alloy 6082-T6 were also characterized using uniaxial tensile tests and standard fracture tests as per [14]. The 0.2% offset tensile yield strength, σ_Y, of the material was found to be $\approx$ 280MPa. Following yield, the material exhibits a moderate degree of strain hardening up to an ultimate tensile strength of $\approx$ 360MPa at a strain of about 11%. The $J-R$ curve of the aluminum alloy 6082-T6 was measured by testing fully-dense specimens with a fatigue pre-crack and overall dimensions (L, W and B) as indicated in Fig. 6.2. The fracture toughness of the as-received material was thereby measured to be, $K^S_{J_{IC}} = 27\text{MPa}\sqrt{m}$.

6.3 Experimental results

The three-point bending response of specimens with a single hole is shown in Fig. 6.3(a), where the force, F, applied at mid-span is plotted as a function of CMOD. The results are given for the hole diameter, $d = 2.3$ and 4.0mm. Both specimens display an elastic-plastic response up to a peak load F_{pk} at a crack mouth opening displacement CMOD$_{pk}$. The peak load is mildly sensitive to the hole diameter, whereas CMOD$_{pk}$ increases significantly with increasing hole diameter. At peak load, a sharp crack initiates from the hole and causes an abrupt load-drop. Subsequently, quasi-static crack growth leads to a softening response in the load versus CMOD curve. The crack growth resistance curves for the two specimens are also shown in Fig. 6.3(a): the stress intensity factor, K_J, normalized by the fracture toughness of the parent material, $K^S_{J_{IC}}$, is plotted as a function of crack extension, Δa. Note that the required stress intensity for the onset of crack growth for both cases exceeds that of the parent material ($K_{J_{IC}}/K^S_{J_{IC}} > 1$). In addition, the $K^S_{J_{IC}}$ increases with increasing hole diameter, d. This toughening effect is due to crack tip blunting.

The effect of the interaction of multiple holes on fracture toughness in Fig. 6.3(b) were presented, where the three-point bending response of specimens with a row of holes is shown for

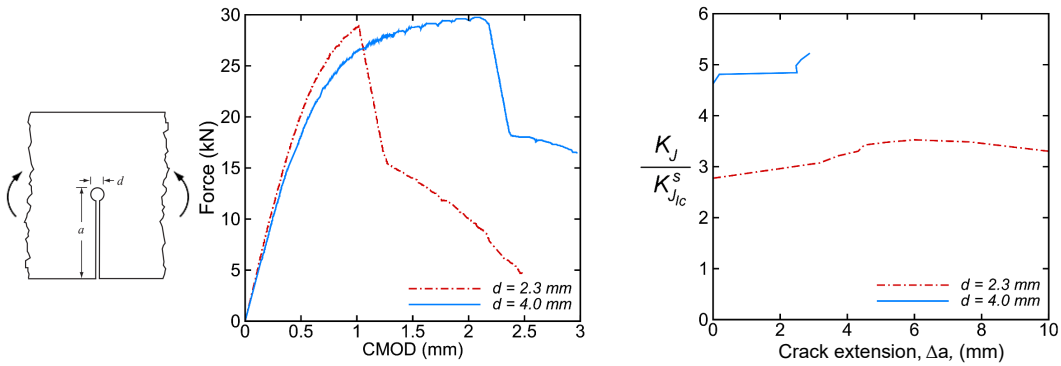

(a)

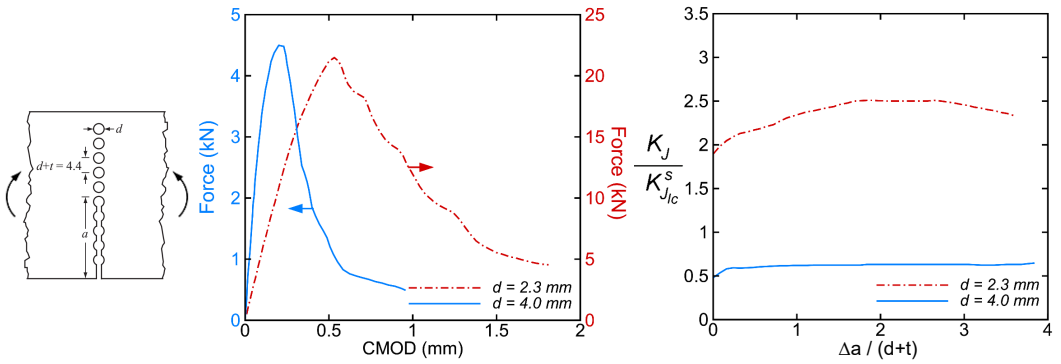

(b)

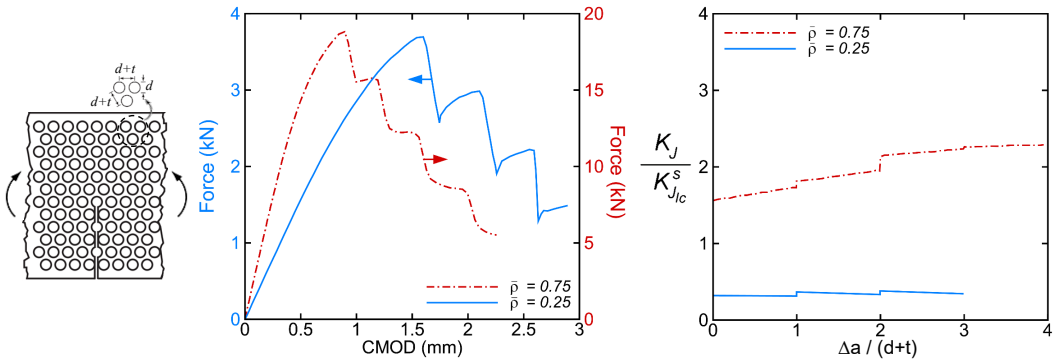

(c)

Figure 6.3: Results of fracture toughness tests on (a) specimens with a single hole, (b) specimens with a row of holes and (c) specimens of micro-architectured materials. For each type of specimen, a sketch of the geometry (left), the three-point bending, force - crack mouth opening displacement (CMOD) response (middle), and the crack growth resistance curves (right) are shown. The hole diameter, $d = 2.3$mm, for micro-architectured material with relative density, $\bar{\rho} = 0.75$, and $d = 4.0$mm for $\bar{\rho} = 0.25$. The hole spacing, $d + t = 4.4$mm, for the specimens with a row of holes and the micro-architectured materials.

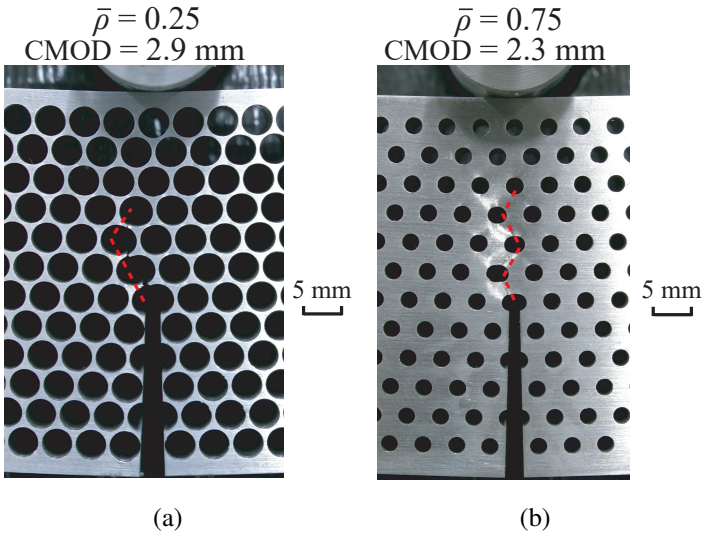

Figure 6.4: Surface images of deformed specimens of micro-architectured materials: (a) with a relative density, $\bar{\rho} = 0.25$, and deformed under three-point bending to a crack mouth opening displacement (CMOD) of 2.9mm; and (b) with $\bar{\rho} = 0.75$ and deformed to CMOD$= 2.3$mm. In both (a) and (b), the crack path is shown by a dashed red line. The hole diameter, $d = 2.3$mm, for micro-architectured material with $\bar{\rho} = 0.75$ and $d = 4.0$mm for $\bar{\rho} = 0.25$. The hole spacing, $d + t = 4.4$mm, for both the specimens.

two selected values of hole diameter, $d = 2.3$ and 4.0mm. Both specimens have an elastic-plastic response up to a peak load F_{pk} at which point crack growth initiates. Subsequently, there is a softening response as the crack extends. The normalized crack growth resistance curves for both specimens with a row of holes are also shown in Fig. 6.3(b). Here, the crack extension Δa has been normalized by the hole spacing, $d + t = 4.4$mm. A comparison of Figs. 6.3(b) and 6.3(a) shows that the fracture toughness of specimens with a row of holes is less than that of the specimens with a single hole. Also, in contrast to the single hole specimens, the toughness of specimens with a row of holes decreases with increasing hole diameter, d. This is due to the fact that the wall thickness, t, decreases with increasing d since the hole spacing is kept fixed at $d + t = 4.4$mm. Despite this knockdown in fracture toughness, a promising result emerges from Fig. 6.3(b): the specimen with $d = 2.3$mm requires a critical stress intensity for crack growth exceeding that of the parent material ($K_{J_{IC}}/K^S_{J_{IC}} > 1$).

Next, whether micro-architectured materials can exhibit a fracture toughness that exceeds the

parent material was investigated. The three-point bending responses of single-edge notch specimens of micro-architectured materials with relative densities, $\bar{\rho} = 0.25$ and 0.75 are shown in Fig. 6.3(c). Both specimens exhibit an elastic-plastic response up to a peak load F_{pk} at which point the cell wall at the crack-tip fails and a sharp load-drop ensues. Additional plastic deformation occurs under increasing load for $\bar{\rho} = 0.25$, and at roughly constant load for $\bar{\rho} = 0.75$, until the next cell wall fractures. The normalized crack growth resistance curves for both micro-architectured materials are included in Fig. 6.3(c). Both curves have a step-like shape because the crack extends suddenly by $\Delta a = d + t = 4.4$mm when a cell wall fails. The shape of the resistance curve is sensitive to relative density: the resistance curve is almost flat for $\bar{\rho} = 0.25$, whereas it rises considerably for $\bar{\rho} = 0.75$. The fracture toughness at the onset of crack growth increases with increasing relative density (decreasing hole diameter) and for $\bar{\rho} = 0.75$, the fracture toughness at the onset of crack growth for the micro-architectured material is above that of the parent material. Thus, the crack blunting effects dominate for $\bar{\rho} = 0.75$ while hole-hole interaction effects dominate for the $\bar{\rho} = 0.25$ micro-architectured material.

Surface images of deformed specimens of micro-architectured materials with relative densities $\bar{\rho} = 0.25$ and 0.75 are shown in Fig. 6.4. The crack path in both specimens is marked by a dashed red line. In both cases, crack growth initiates from the hole at the initial crack tip and the advancing crack tip oscillates from left to right but always stays close to the center line of the specimen. Importantly, the images show that the mode of fracture in both the low and high relative density cases is similar with a crack propagating in the solid between the holes with negligible necking of the ligaments, i.e. the fracture mode of the micro-architectured material is not coalescence of the holes associated with necking of the ligaments but due to ductile fracture of the ligaments. To visualize the shape of the crack in the through-thickness direction, X-ray tomography images of deformed specimens were acquired. The X-ray tomography images for the specimen of a micro-architectured material with $\bar{\rho} = 0.75$ are shown in Fig. 6.5, where each image represents a slice of the specimen through the thickness. The images in Fig. 6.5 clearly show a thumbnail shaped crack; at the free surfaces ($x_3/B = 0$ and 1) only two cell walls appear broken, whereas the images taken

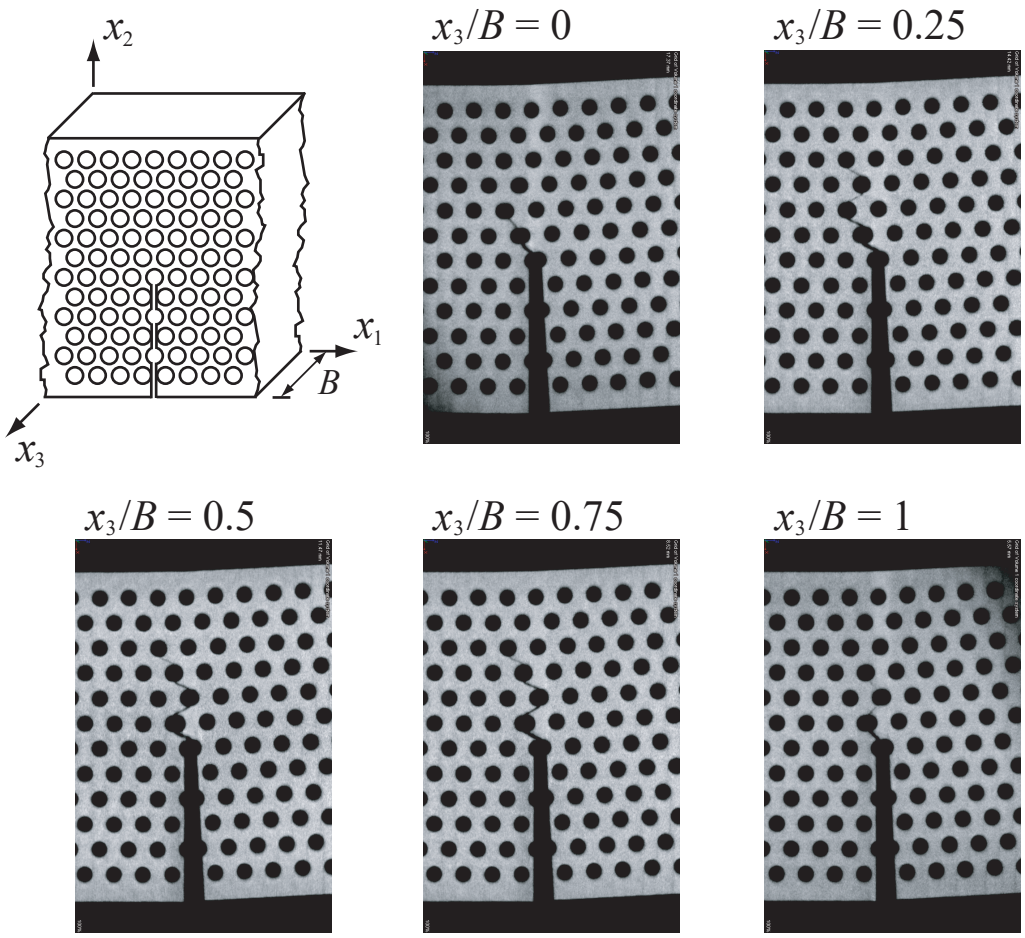

Figure 6.5: X-ray tomography images showing the thumbnail shape of a crack propagating in the single-edge notch bending specimen of a micro-architectured material with a relative density, $\bar{\rho} = 0.75$ and a cell size, $d + t = 2.2$mm. The crack appears shorter at the free surfaces ($x_3/B = 0$ and 1) and longer in the middle of the specimen ($x_3/B = 0.5$).

from within the specimen ($x_3/B = 0.25$, 0.5 and 0.75) reveal that four cell walls are fractured. This suggests that despite the presence of the holes, there is sufficient build-up of hydrostatic stress within the $\bar{\rho} = 0.75$ micro-architectured material for a thumbnail crack front to develop much like in bulk materials.

The measured fracture toughness of all three types of specimens tested are compared in Fig. 6.6, where $K_{J_{IC}}/K^S_{J_{IC}}$ is plotted as a function of the relative density for micro-architectured materials and as a function of the hole diameter for single hole specimens and for those with a row of holes

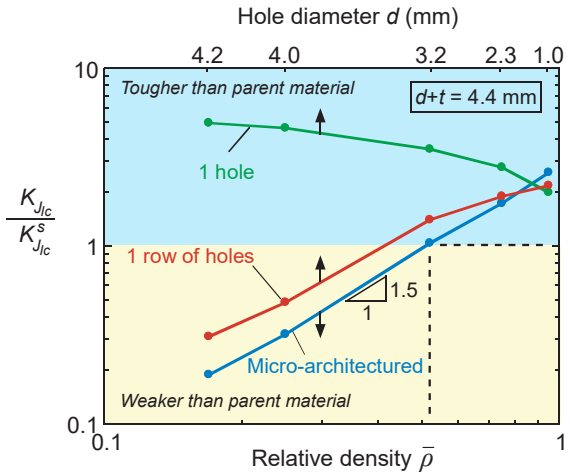

Figure 6.6: The normalized fracture toughness as a function of relative density, $\bar{\rho}$, for micro-architectured materials. Results for specimens with a single hole and for those with a row of holes are also plotted as a function of the hole diameter, d. The hole spacing, $d + t = 4.4$mm, for both the specimens with a row of holes and the micro-architectured materials.

(note the double x-axis). The three types of specimen have a comparable fracture toughness when $d = 1$mm. Note that $d = 1$mm is small compared to the hole spacing, $d + t = 4.4$mm and consequently hole-hole interaction effects are negligible. For $d > 1$mm, hole-hole interaction effects are significant and specimens with a row of holes and micro-architectured materials have a fracture toughness inferior to that of single hole specimens. Furthermore, the fracture toughness of specimens with a row of holes is slightly greater than that of micro-architectured materials. This is due to the orientation of the ligaments; specimens with a row of holes have their cell walls aligned with the direction of maximum tensile stress whereas micro-architectured material have ligaments oriented at 30° from the loading direction, see Fig. 6.2. The most striking result in Fig. 6.6 is that a micro-architectured material with $\bar{\rho} = 0.52$ has the same fracture toughness as that of the parent material, see dashed line in Fig. 6.6. In other words, the micro-architectured material is $\approx 50\%$ lighter than the parent material but possesses the same value of fracture toughness. This remarkable result was obtained here for a micro-architectured material with a hole spacing $d + t = 4.4$mm and next, examine the influence of the parameter, $d + t$, upon the fracture toughness of micro-architectured materials.

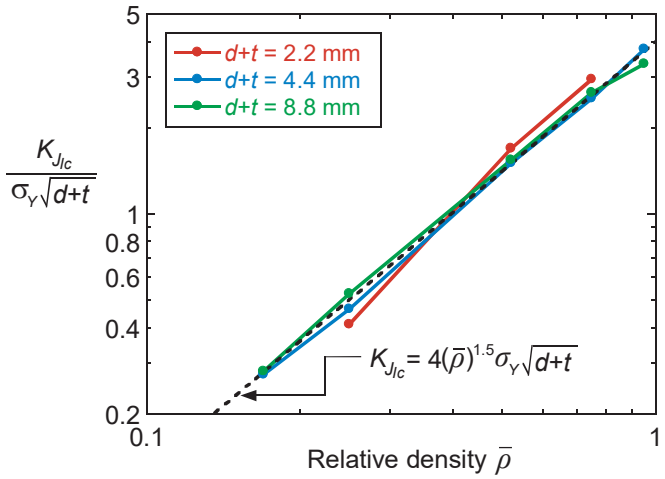

Figure 6.7: The normalized fracture toughness as a function of relative density, $\bar{\rho}$, for micro-architectured materialswith three selected values of hole spacing, $d+t$, obtained using three-point bending fracture test of single-edge notch specimens.

Dimensional analysis suggests that the fracture toughness of micro-architectured materials scales with $\sqrt{l}$, see Eq. (6.1). To investigate this, additional micro-architectured materials were manufactured with the dimensions shown in Fig. 6.2(a) increased by a factor of two. Hence, these five micro-architectured materials had the same values of relative density as those presented in Fig. 6.6, but with a hole spacing $d+t = 8.8$mm instead of 4.4mm. Likewise, smaller micro-architectured materials were also prepared with the dimensions shown in Fig. 6.2(a) reduced by a factor of two. Due to manufacturing limitations, only three small micro-architectured materials with $d+t = 2.2$mm were manufactured: $\bar{\rho} = 0.25$, 0.52 and 0.75. The normalized fracture toughness of micro-architectured materials with $d+t = 2.2$, 4.4 and 8.8mm are plotted in Fig. 6.7 as a function of relative density. Note that here $K_{J_{IC}}$ is normalized by $\sigma_Y\sqrt{d+t}$, where σ_Y is the yield strength of the parent material. Using this normalization, the results for the three different values of $d+t$ collapse onto a single line. This confirms that the fracture toughness scales with the square-root of the cell size. Moreover, a linear fit to the data in Fig. 6.7 suggests that

$$K_{J_{IC}} = 4\,(\bar{\rho})^{1.5}\,\sigma_Y\sqrt{d+t} \tag{6.5}$$

The value of the exponent, 1.5, is the same as that for aluminum metal foams [199, 200]; it is less than the value of 2 obtained for hexagonal micro-architectured materials [191, 192] which are bending-dominated micro-architectured materials but greater than the value of 1 obtained for the stretch-dominated octet trusses [9]. However emphasizing that, a-priori, over the very large relative density range investigated here there is no reason to expect the usual bending/stretching dominated scaling that exists for low relative density micro-architectured and lattice materials. The physical reason behind the existence of such a power-law scaling in Fig. 6.7 needs further investigation.

6.4 Numerical method

The experimental results suggest that the micro-architectured material investigated here has a high fracture toughness (in some cases exceeding that of the solid material). However, from the experiments which have complied with the usual [14] standard developed for solid metals, it remains unclear whether a $J-$field is present within the specimens and thus whether the experiments result in a valid fracture toughness measurement. To interrogate this issue here report finite element calculations of fracture of these micro-architectured materials. The numerical method chosen is motivated by the observation reported above that fracture of the micro-architectured material occurs via the propagation of a ductile crack between the holes of the micro-architectured material, i.e. chosing a constitutive framework for progressively cavitating ductile solid that has been widely employed to model ductile fracture in metals and alloys including Aluminum alloys.

The finite element calculations are carried out using in-house data parallel finite element code, which is based on the dynamic principle of virtual work using a finite deformation Lagrangian convected coordinate formulation [1]. In order to compare predictions with experiments, finite element calculations are carried out for single-edge notch specimens with a single hole, a row of holes and a hexagonal array of holes (micro-architectured material) subjected to three-point bending, Fig. 6.8. The overall in-plane (along x and y axes) dimensions of the single-edge notch specimen analyzed are the same as in experiments. However, the thickness, B, (dimension along z axis) of the specimen in the calculations is taken to be 1mm and overall plane strain conditions are imposed on $z = 0$ and $z = B$ surfaces of the specimen. The y-displacement of the specimen is

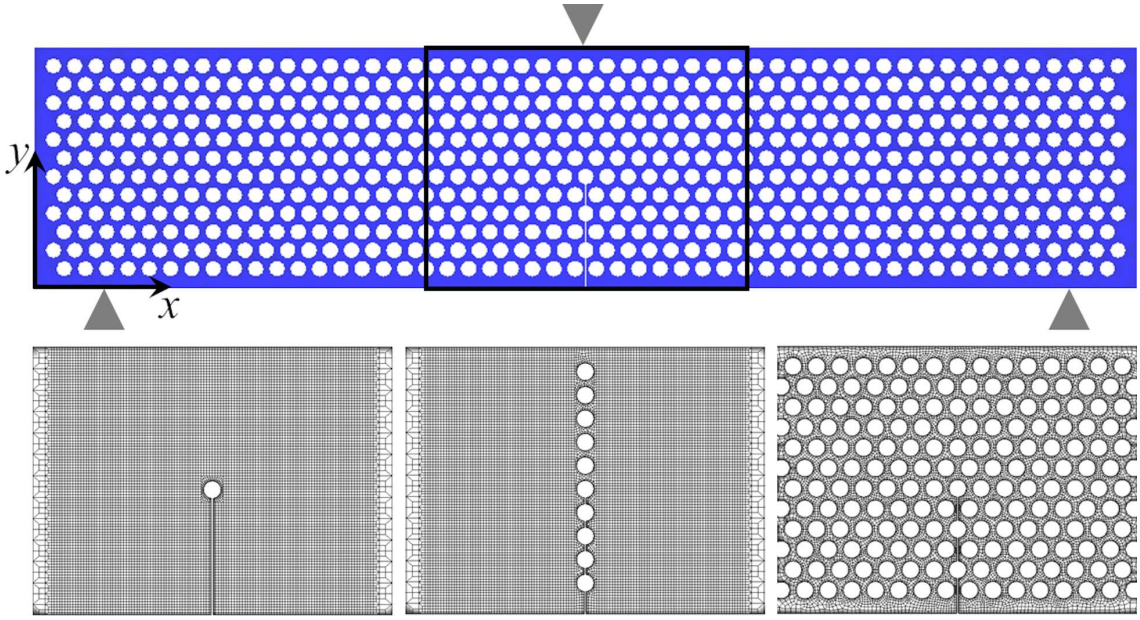

Figure 6.8: Sketch of the single-edge notch specimen of a micro-architectured material with a hexagonal array of holes subjected to three-point bending (top). Zoomed view of the finite element mesh in single-edge notch specimens with a single hole, a row of holes and a hexagonal array of holes (bottom left-right).

constrained at locations, $y = 0$, $x = 14$mm and $y = 0$, $x = 214$mm in the reference configuration to prevent rigid body motion. The finite element calculations are based on the dynamic principle of virtual work for numerical convenience but the focus here is on the quasi-static response, hence to minimize the wave effects a time varying velocity, $V_y(t)$, in the negative y direction is applied at location, $y = 50$mm, $x = 114$mm, that follows the relation:

$$V_y\left(t\right) = \begin{cases} V_y^0 t/t_r & \text{if} \quad t \leq t_r \\ V_y^0 & \text{if} \quad t > t_r \end{cases} \tag{6.6}$$

where, t is the analysis time, t_r is the rise time and V_y^0 is the final velocity of the punch for $t > t_r$. In the calculations, $t_r = 1.0 \times 10^{-3}$s and $V_y^0 = 1.0 \times 10^3$mm/s (along negative y axis) is used.

The constitutive framework described in Section 2.2 for a progressively cavitating ductile solid, contains several constitutive parameters that need to be determined. The constitutive parameters

that characterize the elastic-viscoplastic response of a fully dense 6082-T6 aluminum alloy were considered at first. To this end, first fix upon the values, $E = 70$GPa and $\nu = 0.3$, and obtain the remaining parameters in Eq. (2.7) using the portion of the experimentally obtained uniaxial stress-strain curve before the onset of necking. The values of the constitutive parameters that best describe the overall stress-strain response of the as-received fully dense material are: $\sigma_0 = 280$MPa, $\varepsilon_0 = \sigma_0/E = 0.00429$, $N = 0.64$, $m = 0.002$ and $\dot{\varepsilon}_0 = 0.1\text{s}^{-1}$. Next, the values of $q_1 = 1.5$ and $q_2 = 1.0$ in Eq. (2.2) are taken from [201], and the values of $f_c = 0.05$ and $f_f = 0.1$ in Eq. (2.4) are taken following [202]. Finally, the values of the initial void volume fraction (value of f at $t = 0$), $f_0 = 0.005$, and the values of $\varepsilon_N = 0.05$, $s_N^{\varepsilon} = 0.01$ and $f_N^{\varepsilon} = 0.02$ in Eq. (2.9) are obtained by minimizing the mean squared error between the predicted and experimentally obtained force versus CMOD response of two single-edge notch bending specimens of micro-architectured materialswith relative densities, $\bar{\rho} = 0.25$ and 0.75, using the Nelder-Mead simplex algorithm and following a procedure similar to that of [203].

The finite element calculations use twenty-node brick elements and eight point Gaussian integration in each element for integrating the internal force contributions, and twenty-seven point Gaussian integration for the element mass matrix. Lumped masses are used so that the mass matrix is diagonal. The discretized equations are integrated using the explicit Newmark β-method with $\beta = 0$ [93]. The constitutive updating is based on the rate tangent modulus method [94], while material failure is implemented via the element vanishing technique [90]. Representative finite element meshes for single-edge notch specimens with a single hole, a row of holes and a hexagonal array of holes are shown in Fig. 6.8. The finite element meshes are all generated using a single element in the through-thickness direction (along z axis). A fine in-plane (along x and y axes) mesh is used with a fixed element size of 0.5mm in a 60×50mm^2 region near the center of the specimen.

6.5 Numerical results

The reaction force at the mid-span versus CMOD curves, of single-edge notch specimens with a single hole, a row of holes and a hexagonal array of holes (micro-architectured material) are

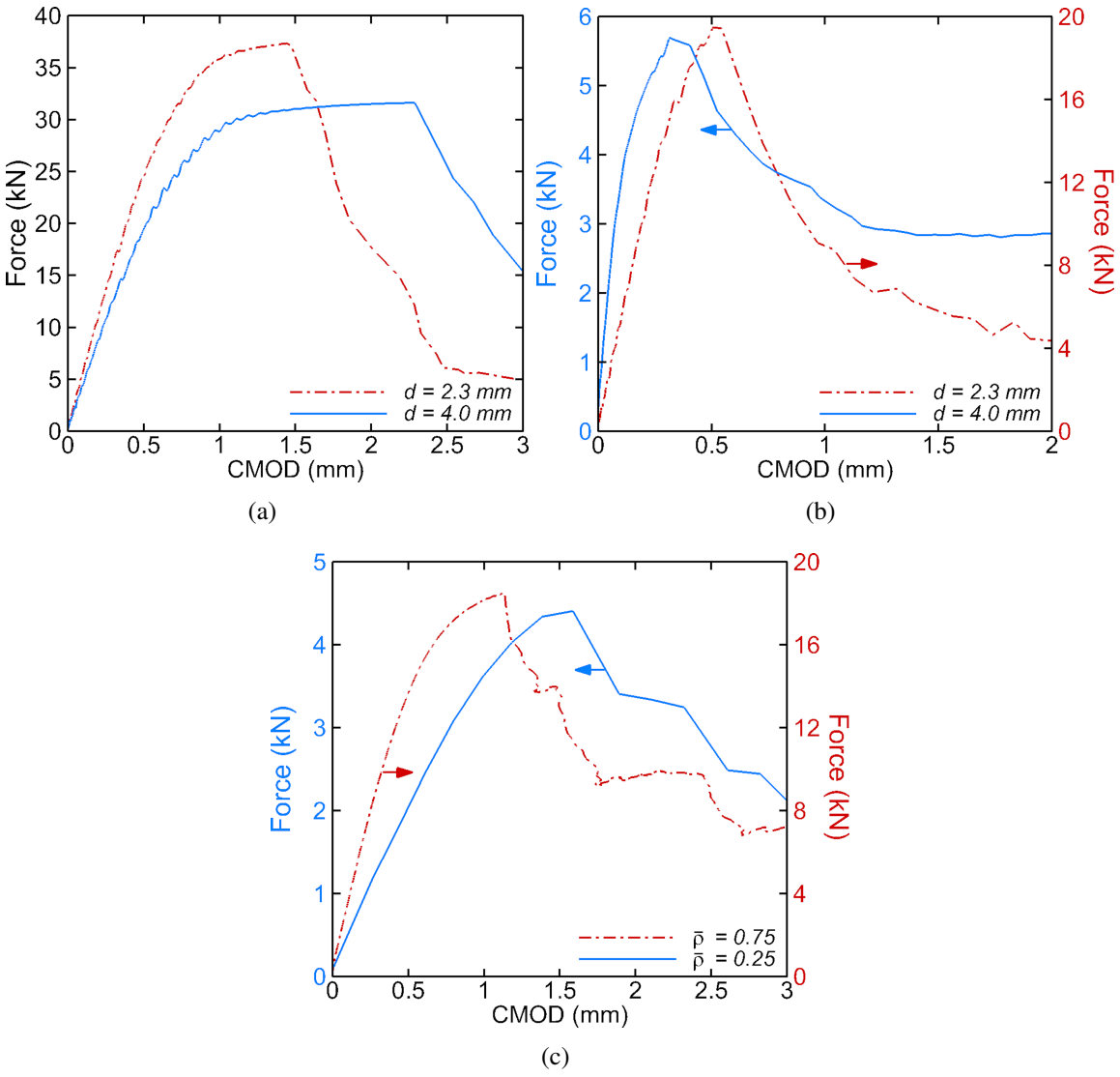

Figure 6.9: Predicted force versus crack mouth opening displacement (CMOD) response of single-edge notch specimens with (a) a single hole, (b) a row of holes and (c) a hexagonal array of holes (micro-architectured material) subjected to three-point bending. The hole diameter, $d = 2.3$mm, for micro-architectured material with relative density, $\bar{\rho} = 0.75$, and $d = 4.0$mm for $\bar{\rho} = 0.25$. The hole spacing, $d + t = 4.4$mm, for the specimens with a row of holes and the micro-architectured materials.

shown in Fig. 6.9. Similar to the experimental results presented in Fig. 6.3, the predicted three-point bending response of all the specimens reported in Fig. 6.9 displays an elastic-plastic response up to peak load, F_{pk}, followed by a softening response due to crack growth initiation. The predicted three-point bending response of the specimens with a row of holes and micro-architectured

materials up to F_{pk} is in close quantitative agreement with the experimentally observed responses for all hole diameters and spacings. However, for the specimens with a single hole the predicted three-point bending response differs somewhat from that of observations for certain hole diameters. For example, for a specimen with a single hole of diameter, $d = 2.3$mm the measured $F_{pk} \approx 29$kN and CMOD at F_{pk} is $\approx$ 1mm while in the finite element calculations $F_{pk} \approx 37$kN and CMOD at F_{pk} is ≈ 1.4mm. On the other hand, for a specimen with a single hole of diameter, $d = 4.0$mm, both experimental and finite element results are in close agreement.

In the experiments, the $J - R$ curves were evaluated using the elastic compliance method as given in [14]. However, the J-integral can also be directly obtained from the finite element results. Recall that, for a two dimensional, planar, nonlinear elastic material, under the assumption of small displacement gradient and with body forces neglected, the J-integral is given by [138]

$$J = -\int_C (\sigma_{ij}\frac{\partial u_i}{\partial x_1} - W\delta_{1j})n_j\, ds \tag{6.7}$$

in terms of the stress σ_{ij}, displacement u_i, the increment of arc length along the path ds, strain energy W and the outward normal to the path n_j. In order to determine the value of the J-integral from the finite element results, it is convenient to re-write the contour integral as an equivalent area integral. The energy release rate, J-integral, can then be calculated using the relation [204]

$$J = \int_A (\sigma_{ij}\frac{\partial u_i}{\partial x_1} - W\delta_{1j})\frac{\partial Q_1}{\partial x_j}\, dA \tag{6.8}$$

where Q_1 is a smooth weighting function defined on the domain.

The dependence of the J-integral as obtained from the finite element results using Eq. (6.8) upon the radius of contours surrounding the initial notch tip of the single-edge notch bend specimens with a single hole, a row of holes and a hexagonal array of holes is shown in Fig. 6.10. As shown in Figs. 6.10(a) and (b), for the specimens with a single hole and a row of holes the value of J-integral is slightly path dependent. Also, the extent of path dependence of J-integral increases with increasing CMOD. However, for contour radius ≥ 12mm the value of J-integral tends to sat-

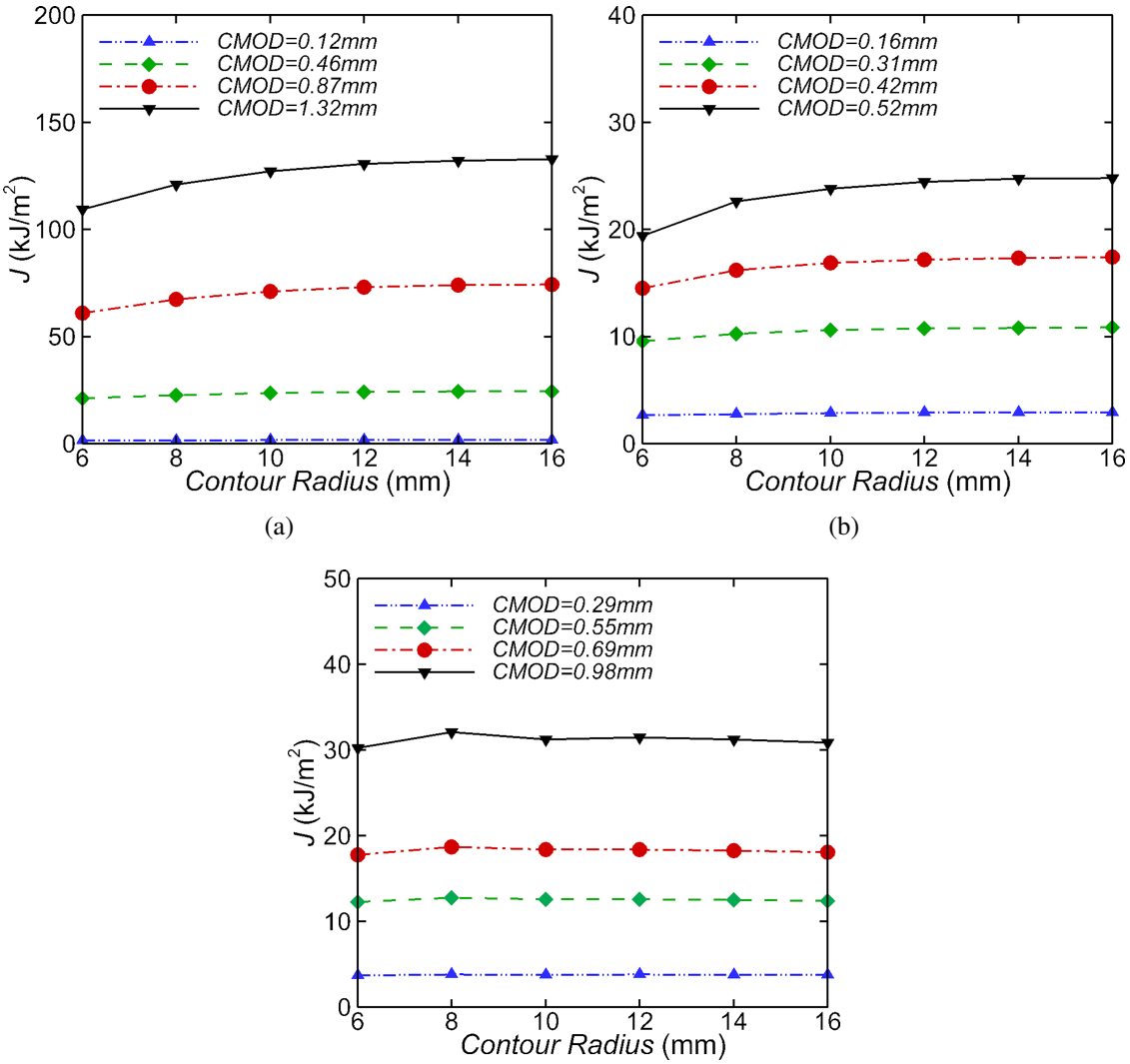

Figure 6.10: Predicted dependence of the value of J-integral on the radii of circular contour surrounding the initial notch tip of the single-edge notch specimens with (a) a single hole, (b) a row of holes and (c) a hexagonal array of holes (micro-architectured material) with relative density, $\bar{\rho} = 0.75$, subjected to three-point bending. The hole diameter, $d = 2.3$mm, for all the specimens and hole spacing, $d+t = 4.4$mm, for the specimens with a row of holes and the micro-architectured material.

urate. The path dependence of J-integral, such that the value of J-integral initially increases with increasing contour radius, under finite deformation where proportional loading is not guaranteed is not entirely unexpected [205]. However, for the micro-architectured material, Fig. 6.10(c), the value of J-integral is almost path independent. Thus, a contour radius of 12mm is selected for

evaluating J-integral for all the specimens. A more detailed discussion on the existence of a J field and the resulting values of J-integral in micro-architectured materials is given in Section 6.6.

The value of J_{IC}, a measure of crack growth initiation toughness, is defined as the value of the contour integral J corresponding to which crack growth initiation is predicted in the finite element calculations. The value of fracture toughness in terms of critical stress intensity factor, $K_{J_{IC}}$, is then obtained using the relation given in Eq. (6.4). Apart from the direct computation of $K_{J_{IC}}$ via the J-integral, the value of $K_{J_{IC}}$ is also obtained by direct application of the [14] standard to the finite element results; however, instead of using the elastic compliance method to obtain crack length, the crack length was known immediately from the finite element results.

A comparison of the normalized fracture toughness, $K_{J_{IC}}/K^s_{J_{IC}}$, (i) as measured from three-point bending experiments, (ii) as predicted by post-processing of the finite element results using the [14] standard and (iii) as predicted by direct computation of J-integral for all three types of single-edge notch specimens are shown in Fig. 6.11. For all three specimens, the results are normalized by, $K^s_{J_{IC}}$, the experimentally obtained fracture toughness of the as-received plate of aluminum alloy 6082-T6. Very good agreement between the predicted fracture toughness from the finite element calculations by both evaluation procedures and the experimental results is noted. The biggest discrepancy between the finite element predictions and the experimental results is observed for specimens with a single hole of small diameter. This is consistent with the differences between the predictions in Fig. 6.9(a) and experimental measurements in Fig. 6.3(a).

6.6 Discussion

The mechanical properties of micro-architectured materials depend upon their topology. The effect of topology of micro-architectured materials upon the stiffness and strength is well documented, but optimizing their fracture toughness is a challenging and intriguing task. Here, the results of fracture toughness tests on micro-architectured materials that comprise a hexagonal array of holes drilled in the plates of an aluminum alloy were presented. The fracture toughness of the micro-architectured materials considered here is governed by two competing mechanisms: crack blunting and hole-hole interaction. The holes act as crack arrestors and blunt the crack-tip

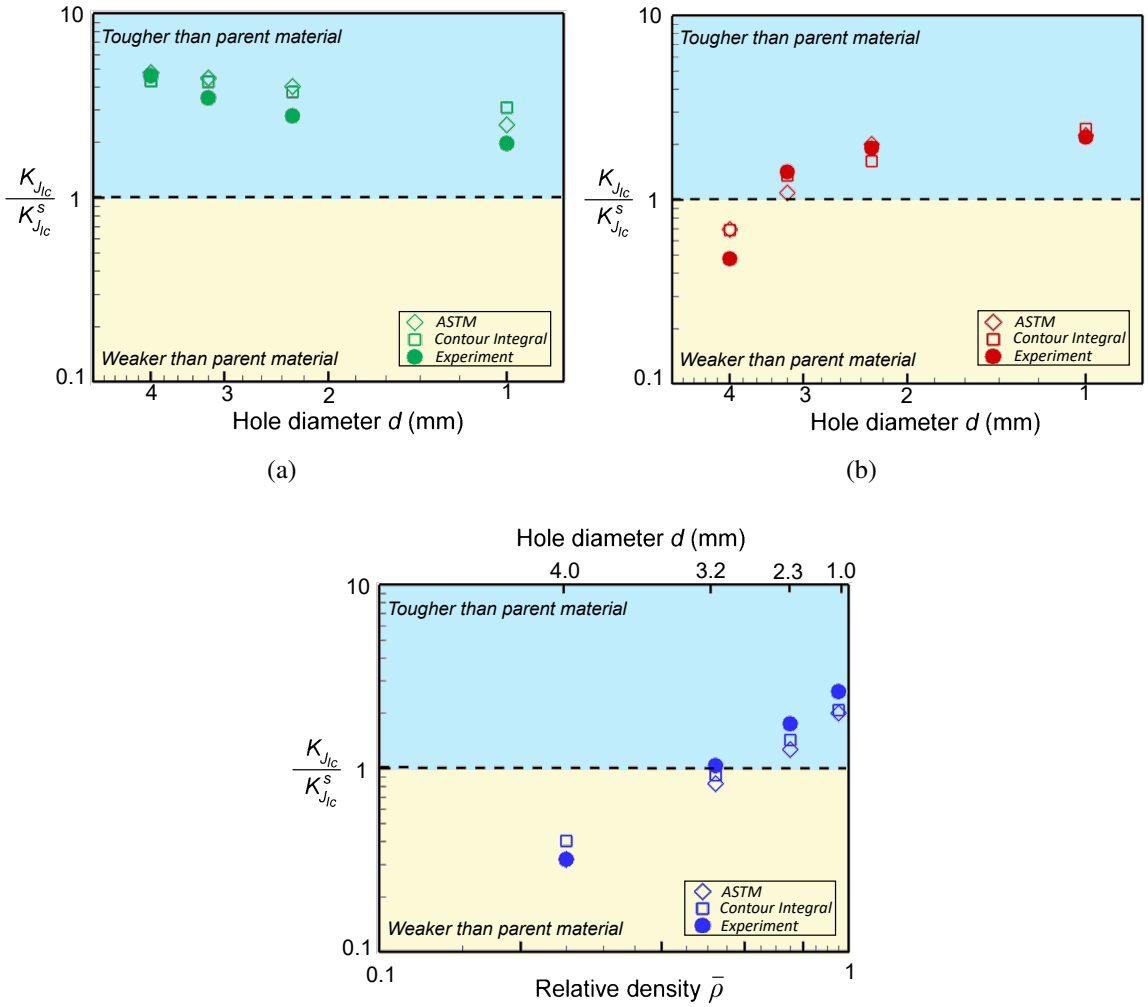

Figure 6.11: Comparison of the normalized fracture toughness measured from the three-point bending experiments (labeled 'Experiment') and computed from the post processing of the finite element results using a procedure that mimics the [14] standard (labeled 'ASTM') and via direct computation of J-integral (labeled 'Contour Integral') for (a) specimens with a single hole of diameter, d, (b) specimens with a row of holes of diameter, d, and hole spacing, $d + t = 4.4$mm, and (c) micro-architectured materials with relative density, $\bar{\rho}$, and $d + t = 4.4$mm.

so that increasing the hole diameter will result in an increase in the fracture toughness whereas for fixed hole spacings, increasing the hole diameter will result in increased hole-hole interactions and decrease the fracture toughness.

The competing effect of crack blunting and hole-hole interaction on the evolution of damage in

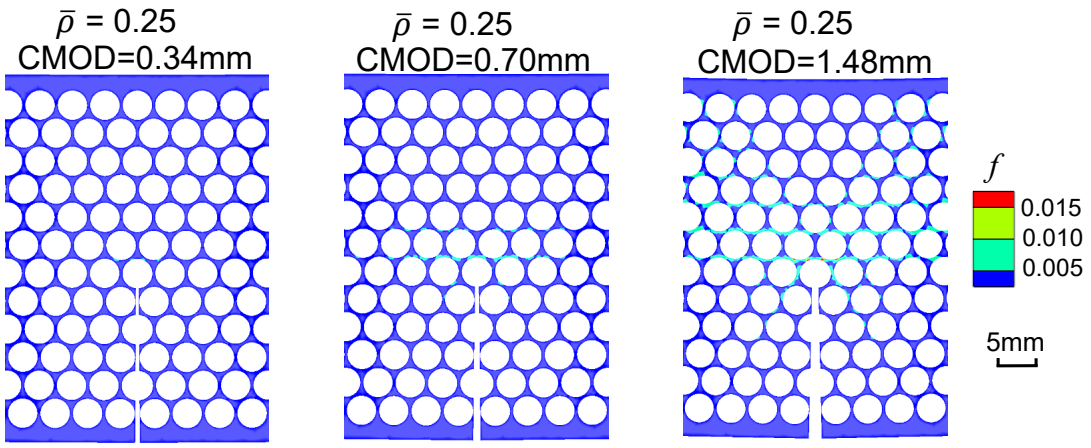

(a)

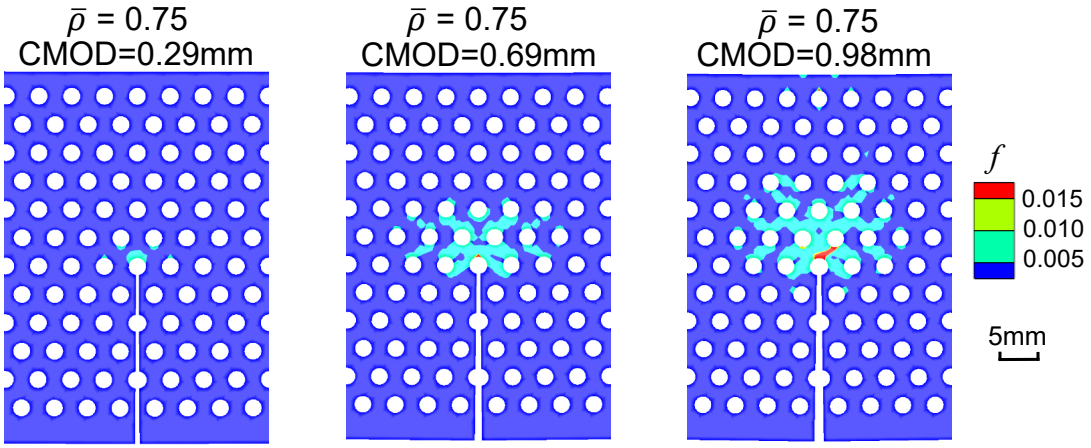

(b)

Figure 6.12: Predicted distribution of porosity, f, near the initial notch of single-edge notch specimens of micro-architectured materials with (a) relative density, $\bar{\rho} = 0.25$, post three-point bending to crack mouth opening displacement (CMOD) values 0.34, 0.70 and 1.48mm, and (b) $\bar{\rho} = 0.75$ post three-point bending to CMOD values 0.29, 0.69 and 0.98mm. The hole diameter, $d = 2.3$mm, for micro-architectured material with $\bar{\rho} = 0.75$ and $d = 4.0$mm for $\bar{\rho} = 0.25$. The hole spacing, $d + t = 4.4$mm, for both the micro-architectured materials.

micro-architectured materials is elucidated in Fig. 6.12. In the figure, the predicted distribution of porosity, f, near the initial notch of single-edge notch specimens of micro-architectured materials with $\bar{\rho} = 0.25$ ($d = 4.0$mm) and $\bar{\rho} = 0.75$ ($d = 2.3$mm) are shown post three-point bending to three values of CMOD. The hole spacing in both micro-architectured materials is fixed at $d+t = 4.4$mm. Prior to crack growth initiation, the increased porosity is spread over a larger area in the micro-

architectured material with $\bar{\rho} = 0.25$ compared to the micro-architectured material with $\bar{\rho} = 0.75$ due to increased hole-hole interaction. Thus, the fracture toughness of the micro-architectured material with $\bar{\rho} = 0.25$ is less than that of the fracture toughness of the as-received plate of the parent material. On the other hand, due to an optimum balance of hole blunting and hole-hole interaction, the fracture toughness of the micro-architectured material with $\bar{\rho} = 0.75$ exceeds that of the fracture toughness of the parent material.

The measured properties of the micro-architectured materials comprising a hexagonal array of holes are included in the material property charts, Fig. 6.1. The density of the micro-architectured materials is $\rho = \bar{\rho}\rho_s$, where the density of the parent material, $\rho_s = 2700$kg/m^3. In Fig. 6.1(b), the compressive strength of the micro-architectured material is the out-of-plane yield strength of magnitude $\bar{\rho}\sigma_Y$, where the yield strength of the parent material is $\sigma_Y = 280$MPa. It is clear from Fig. 6.1(a) that the micro-architectured materials of cell size $d + t = 8.8$mm are positioned at the outer boundary of the currently available material space. They outperform the toughest metals and they compete well with the toughest natural materials. Recall that the measured fracture toughness of these micro-architectured materials scales with the square-root of the cell size $(d + t)$, Eq. (6.5). Consequently a hole spacing of $d + t = 30$mm, would lead to a micro-architectured material that is tougher than any known metals or natural materials as shown in Fig. 6.1. In conclusion, micro-architectured materials offer a combination of high strength and high fracture toughness that outperforms other lightweight materials of density less than 1000kg/m^3.

In the present study, all the fracture tests of single-edge notch specimens under three-point bending were carried out in compliance with the [14] standard. The question arises: to what extent can a standard test procedure that was established for solid materials, be applicable to micro-architectured materials? Consider, for example, the recent study by [206] on an open cell aluminum alloy foam. They found that a zone of randomly failed struts develops ahead of the primary crack tip, and the size of this zone is similar to the plastic zone size. In such cases a crack tip J-field is absent at the initiation of crack growth and the measured J_{IC} value cannot be treated as a material property even though the specimen size meets the usual criteria for J validity. The ability of the

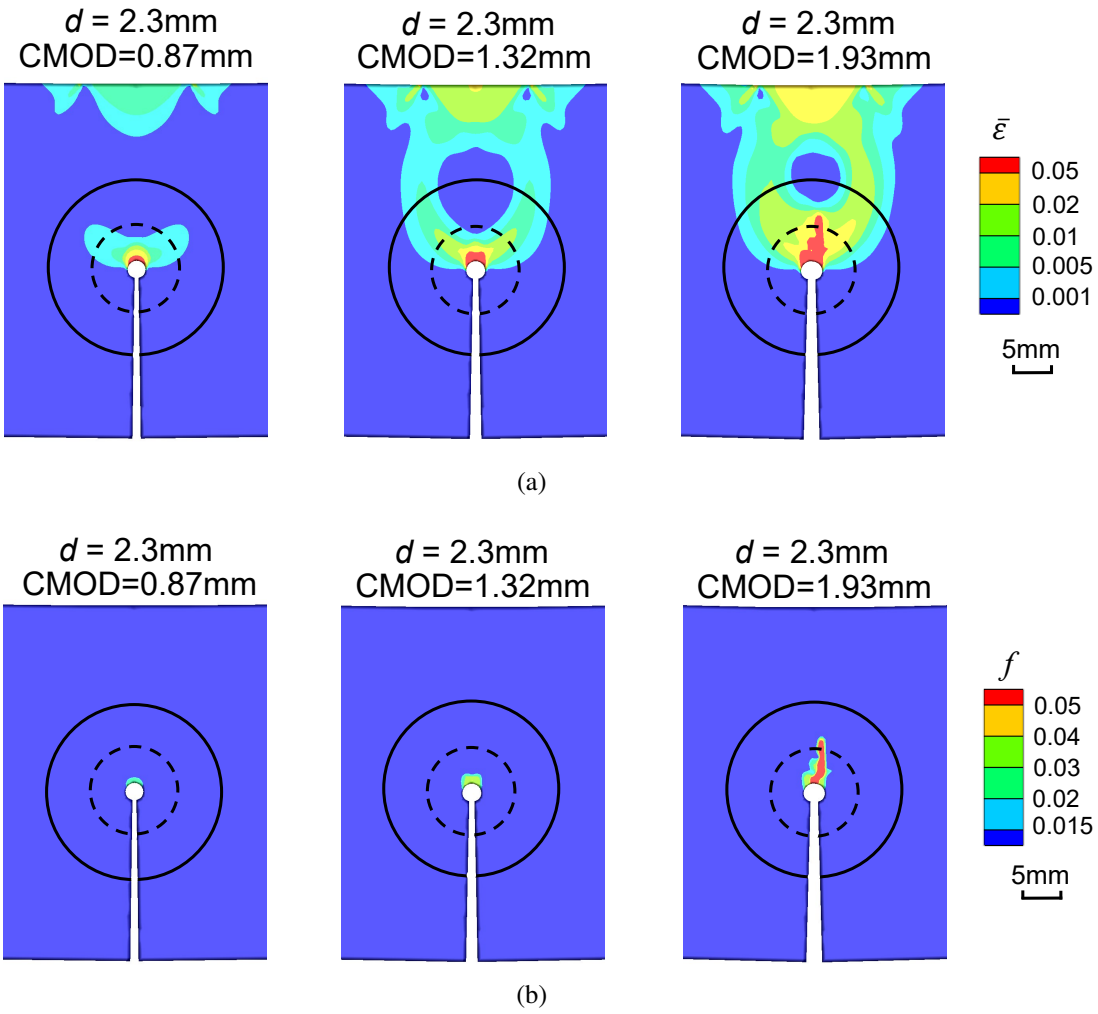

Figure 6.13: Predicted distribution of (a) equivalent plastic strain, $\bar{\varepsilon}$, and (b) porosity, f, near the initial notch in a single-edge notch specimen with a single hole of diameter, $d = 2.3$mm, post three-point bending to crack mouth opening displacement (CMOD) values 0.87, 1.32 and 1.93mm. A contour of radius, $r = 12$mm, is marked as solid black circle while a contour of radius, $r = 6$mm, is marked as dashed black circle.

value of J-integral to characterize the fracture properties is contingent upon the existence of a J-field near the crack tip which depends on whether the plastic zone fully encompasses the fracture process zone or not.

The predicted distribution of equivalent plastic strain, $\bar{\varepsilon}$, and of porosity, f, near the initial notch in a single-edge notch specimen with a single hole of diameter, $d = 2.3$mm, and in a single-edge notch specimen of a micro-architectured material with relative density, $\bar{\rho} = 0.75$ ($d = 2.3$mm),

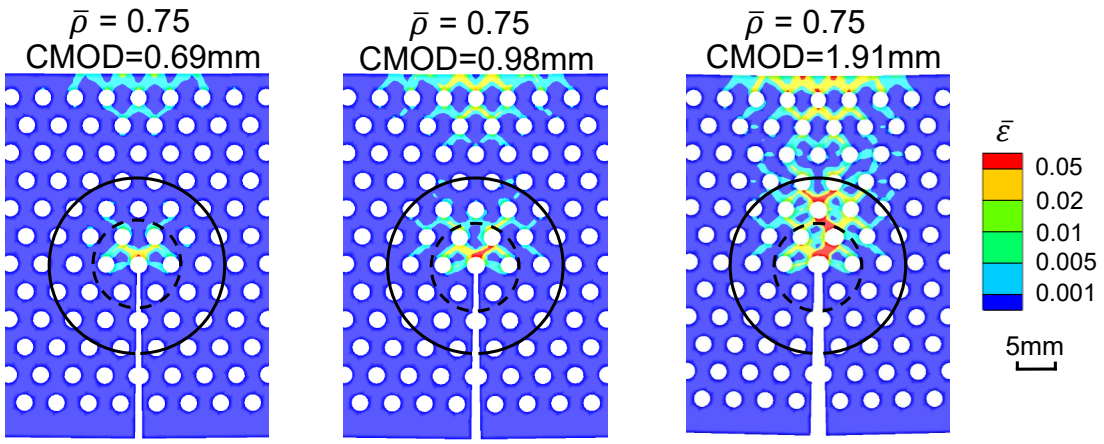

(a)

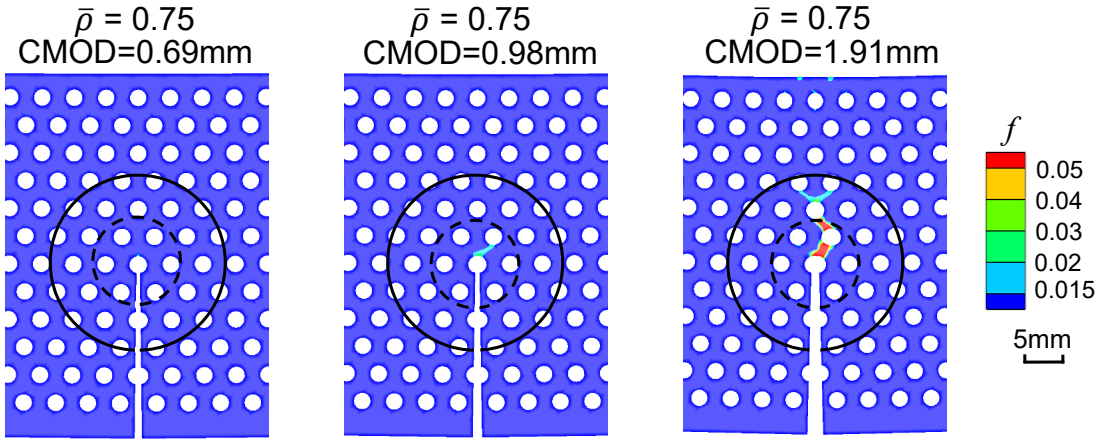

(b)

Figure 6.14: Predicted distribution of (a) equivalent plastic strain, $\bar{\varepsilon}$, and (b) porosity, f, near the initial notch in a single-edge notch specimen of micro-architectured material with relative density, $\bar{\rho} = 0.75$, post three-point bending to crack mouth opening displacement (CMOD) values 0.69, 0.98 and 1.91mm. The hole diameter, $d = 2.3$mm, in the micro-architectured material. A contour of radius, $r = 12$mm, is marked as solid black circle while a contour of radius, $r = 6$mm, is marked as dashed black circle. The contour plot in (b) is for the same case shown in Fig. 6.12(b) but plotted at greater values of CMOD.

are shown in Figs. 6.13 and 6.14, respectively, for three-point bending to three values of CMOD. In Figs. 6.13 and 6.14, the first two values of CMOD are for $J < J_{IC}$ while the greatest value of CMOD corresponds to $J > J_{IC}$. For both the specimens with a single hole and the micro-architectured material, the fracture process zone size (i.e. $f \approx f_c$, where $f_c = 0.05$) is much smaller than the plastic zone size. Furthermore, the plastic zone size in the micro-architectured

material is relatively small compared to that in the specimen with a single hole for comparable values of CMOD. The smaller plastic zone size in the micro-architectured material compared to the specimen with a single hole also rationalizes the observation in Fig. 6.10 that the value of J-integral in the micro-architectured material is less path dependent than the specimen with a single hole. The fact that the fracture process zone size is much smaller than the plastic zone size and the J-integral is almost path-independent in the single-edge notch specimens of micro-architectured material suggests that the measured fracture toughness, J_{IC} or $K_{J_{IC}}$, can be treated as a material property. Furthermore, in the finite element calculations, the fracture toughness of single-edge notch specimens subjected to three-point bending is in agreement for the two procedures, one that mimics the [14] standard and via direct computation of J-integral.

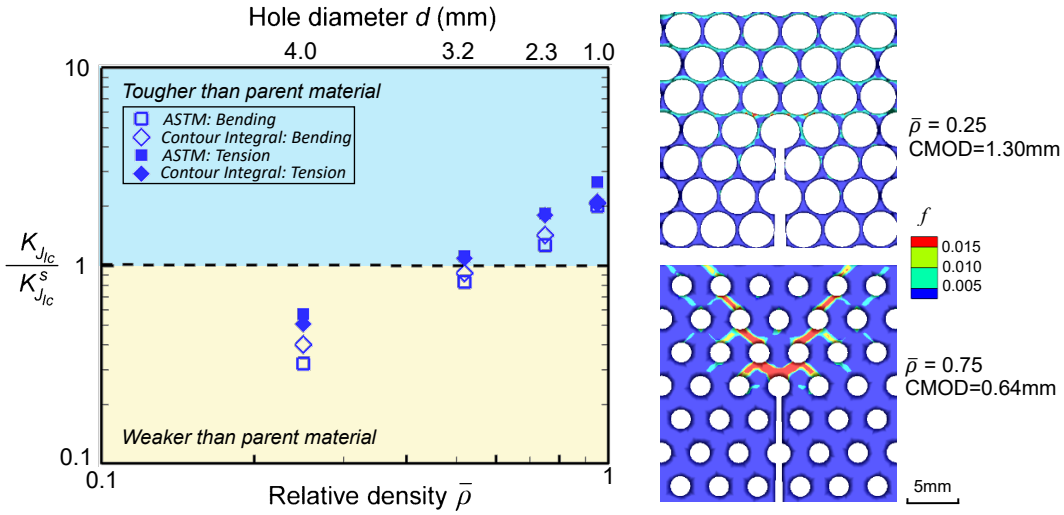

(a) (b)

Figure 6.15: (a) Comparison of the normalized fracture toughness predicted from finite element calculations of single-edge notch specimens of micro-architectured materials with relative density, $\bar{\rho}$, subjected to three-point bending and tension. The values of fracture toughness from finite element calculations are computed using a procedure that mimics the ASTM standard (labeled 'ASTM') and via direct computation of J-integral (labeled 'Contour Integral'). (b) Predicted distribution of porosity, f, near the initial notch of single-edge notch specimens of micro-architectured materials with relative density, $\bar{\rho} = 0.25$, post tensile loading to crack mouth opening displacement (CMOD) value 1.30mm and $\bar{\rho} = 0.75$ post tensile loading to CMOD$= 0.64$mm. The hole spacing, $d + t = 4.4$mm, for all micro-architectured materials.

Finally, to further establish that the fracture toughness of the micro-architectured materials obtained using single-edge notch bending specimens does indeed represent a useful material property which is independent of specimen geometry, finite element calculations of ductile fracture in single-edge notch specimens of micro-architectured material under remote uniaxial tension were carried out as well. To this end, the single-edge notch specimens of micro-architectured material with the same geometry as in Fig. 6.8 are subjected to tensile loading along the x-axis. The fracture toughness is evaluated using the [14] standard and also via direct computation of J-integral. In the evaluation of fracture toughness of single-edge notch specimens subjected to tension following ASTM standard, a modified geometric function for single-edge notch tension specimen [207] is utilized. A comparison of the normalized fracture toughness, $K_{J_{IC}}/K^S_{J_{IC}}$, predicted from finite element calculations of single-edge notch specimens subjected to tension and three-point bending are shown in Fig. 6.15(a). As shown in the figure, the fracture toughness of single-edge notch specimens of micro-architectured materials subjected to tension show the same scaling between fracture toughness and relative density as in three-point bending. The fracture toughness values obtained for single-edge notch tension specimens are slightly greater than that for single-edge notch bending specimens. This is because the crack-tip constraint in single-edge notch tension specimen is less than the single-edge notch bending specimen. However, emphasizing that the effect of this constraint on fracture toughness is relatively small suggesting that $K_{J_{IC}}$ is sufficient to characterize fracture in these micro-architectured materials. Also, similar to single-edge notch bending specimens, here as well, it is the competing effect of crack blunting and hole-hole interaction on the evolution of damage in micro-architectured materials, as elucidated in Fig. 6.15(b), that leads to the same scaling between fracture toughness and relative density.

6.7 Conclusions

The fracture toughness of ductile micro-architectured materials to demonstrate their potential as a lightweight and tough material have been investigated. The micro-architectured materials consisted of a hexagonal array of holes in a ductile material. The key conclusions are as follows:

1. The fracture toughness of the micro-architectured materials with hexagonal array of holes in a ductile material increases with increasing relative density and with increasing cell size.

2. A micro-architectured material with cell size, $d+t = 4.4$mm, and approximately 50% lighter than the parent material has the same fracture toughness as the parent material.

3. The finite element calculations of three-point bending of single-edge notch specimens of micro-architectured materials show that in the micro-architectured materials the plastic zone fully encompasses the fracture process zone and a path independent value of J- integral can be obtained.

4. The fracture toughness of the micro-architectured materials obtained from the finite element calculations of single-edge notch specimens subjected to three-point bending using a procedure similar to the experiments and via direct computation of J-integral are shown to be consistent with the experimental results.

5. The fracture toughness of the micro-architectured materials obtained from the finite element calculations of single-edge notch specimens subjected to tension show the same scaling between fracture toughness and relative density as in three-point bending. This result confirms the validity of the measured fracture toughness as a useful material property.

6. A comparison with other engineering materials show that the micro-architectured materials investigated expand the current material property space: it possesses an excellent combination of high strength and fracture toughness compared to other existing lightweight materials.

7. SUMMARY AND FUTURE WORK

7.1 Summary and concluding remarks

Ductile fracture of advanced structural materials involving nucleation, growth and coalescence of microscale voids is affected by the length-scales arising from the material microstructure, the geometry of deformation and the loading condition. These length-scales in turn interact and evolve during the deformation process, resulting in often unknown and counterintuitive subsequent fracture processes. The aim of this dissertation was to understand how the nucleation and growth of macroscopic cracks in ductile materials depend on these evolving length-scales, and transform the field of classical fracture mechanics from the notion of structure $\rightarrow$ fracture to structure $\rightarrow$ microstructure $\rightarrow$ fracture. This enabled microstructure informed prediction of ductile fracture as well as design of lightweight fracture resistant materials. The key contributions of this dissertation are as follows:

- Microstructure-based finite element calculations of mode I crack growth in ductile material matrix containing three-dimensional distribution of inclusions were carried out to identify the micromechanisms of ductile crack advance, and isolate the key microstructural features and material parameters that affect these micromechanisms and fracture toughness of the material. Several features of crack growth behavior and dependence of fracture toughness on microstructural and material parameters observed in experiments, naturally emerged in these calculations. The extent to which the microstructural and material parameters affect the micromechanisms of ductile crack advance and, hence, the macroscopic fracture toughness of the material were discussed. In particular, the results show that there is an increase in the propensity of plastic strain localization with increasing inclusion volume fraction and/or inclusion size. The results also provide guidelines for microstructural engineering to increase ductile fracture toughness, for example, for a material with small inclusions, increasing the mean inclusion spacing has a greater effect on fracture toughness than for a material with

large inclusions.

- Microstructure-based finite element calculations were carried out to model the effect of length-scales induced by the geometry of deformation, in particular bending, and the material microstructure on ductile fracture of dual-phase advanced high strength steel sheets. The results show that the interlacing of length-scales induced by bending and dual-phase microstructure results in extremely complex and heterogeneous deformation patterns. In line with the experimental observations, the calculations predict that despite similar strength and strain hardenability, volume fraction of the phases, and fracture response under uniaxial tension along rolling and transverse directions, the bendability of the sheet steel along rolling direction is less than the bendability along the transverse direction. The results of these calculations also show that efforts to improve the bendability of advanced dual-phase steel sheets must focus on improving the mechanical properties of the relative softer ferrite phase.

- The effect of size, shape, location and properties of the unintended inclusions on the bendability of advanced dual-phase steel sheets were also quantified through microstructure-based finite element calculations. The results show that the presence of a subsurface inclusion in the sheet specimens results in a subsurface crack nucleation under bending that accelerates the localization of plastic strain in the material. In line with the experimental observations, strong inclusion size effects on the bendability of dual-phase steel sheets naturally emerged in the calculations. Furthermore, supervised machine learning was used to mathematically represent the relationship between the 'intended' and 'unintended' microstructural features and the bendability of the dual-phase steel sheets. This mathematical representation was then used to identify the contribution of each parameter and isolate critical features that control the bendability of the advanced dual-phase steel sheets.

- Natural materials such as wood and bamboo possess high fracture toughness at a density below that of water. Here, the potential of metallic micro-architectured materials to out-

perform these natural materials was investigated. The micro-architectured materials were manufactured by drilling a hexagonal array of holes in plates of an aluminum alloy, and the fracture toughness was evaluated using three-point bending tests of single-edge notch specimens. The results show that the fracture toughness of micro-architectured materials increases with increasing relative density and remarkably, a micro-architectured material can be 50% lighter than the parent material but maintain the same fracture toughness. The experiments were complemented by finite element calculations of ductile fracture. In the calculations, the fracture toughness of single-edge notch specimens subjected to three-point bending were evaluated using both, a procedure similar to the experiments and direct computation of the J-contour integral. The fracture toughness as calculated by both methods were consistent with the experimental results. In addition, the calculations were also carried out for single-edge notch specimens subjected to tensile loading, confirming the validity of the measured fracture toughness as a useful material property.

7.2 Future directions

In light of the work carried out and the results presented in this dissertation, several fundamental and technological questions can be investigated in future research works:

- Simple guidelines for microstructural engineering to increase ductile fracture toughness have been identified in this dissertation. However, several recent studies have also explored the possibility of engineering the crack path by designing material microstructures, including the distribution of non-metallic inclusion, and thereby increasing the material's fracture resistance [47]. In this study [47], the fracture resistance of controlled sinusoidal distributions of inclusions were found to be significantly greater than that of a random distribution with the same specified mean inclusion spacing. Interestingly, the study also suggests that adding more inclusions to engineer the crack path can, in certain circumstances, have a beneficial effect on crack growth resistance, a rather counter-intuitive observation. Designing inclusion distribution, potentially 3D distributions, to improve the fracture toughness remains a

challenging task.

- The microstructure-based finite element calculations to quantify the effect of length-scales induced by the geometry of deformation and the material microstructure on ductile fracture of dual-phase advanced high strength steel sheets were carried out for 2D microstructures. Recently, there has been some progress on statistical reconstruction of realistic 3D microstructures from 2D SEM images collected on oblique sections [208]. These reconstructed 3D microstructures can in theory be implemented in the microstructure-based finite element methodology utilized in this work. This will enable a more realistic microstructure-based prediction of the manufacturability of advanced high strength steels.

- The microstructure-based finite element calculations to quantify the effect of length-scales induced by bending and material microstructure on ductile fracture of dual-phase steel sheets were carried out for a fixed sheet thickness and the microstructural length-scales. Some experimental observation suggest that refining and homogenizing the dual-phase microstructure can improve the ductility of the material [177, 209–213]. Thus, a natural next step is to explore the influence of the interlacing of structural and microstructural length-scales on the bendability of advanced dual-phase steel sheets.

- Experimental observations suggest that surface decarburization improves the bendability of advanced high strength dual-phase steels. However, the presence of a softer decarburized surface layer may have an adverse effect on the fatigue properties of the material. The microstructure-based finite element methodology established in this work can be used to get further insight in to the effect of surface decarburization on the bendability and the fatigue properties of the material.

- Recently, many efforts have been directed towards utilizing artificial intelligence (AI) to understand microstructure-fracture correlation in engineering materials [214–217]. For example, in a recent work, the small fatigue crack driving force in polycrystalline materials were identify by machine learning approach [216], while a methodology is presented to

leverage microstructural and micromechanical data to predict fatigue crack path [217]. The microstructure-based finite element methodology utilized to model fracture in multiphase materials in this dissertation can be deployed in conjunction with AI to enable better and more robust microstructure-based prediction of fracture.

REFERENCES

[1] A. Srivastava, L. Ponson, S. Osovski, E. Bouchaud, V. Tvergaard, and A. Needleman, "Effect of inclusion density on ductile fracture toughness and roughness," *Journal of the Mechanics and Physics of Solids*, vol. 63, pp. 62–79, 2014.

[2] P. Chen, H. Ghassemi-Armaki, S. Kumar, A. Bower, S. Bhat, and S. Sadagopan, "Microscale-calibrated modeling of the deformation response of dual-phase steels," *Acta Materialia*, vol. 65, pp. 133–149, 2014.

[3] D.-K. Leu, "A simplified approach for evaluating bendability and springback in plastic bending of anisotropic sheet metals," *Journal of Materials Processing Technology*, vol. 66, no. 1-3, pp. 9–17, 1997.

[4] D. Fan, P. Kaushik, and H. Pielet, "Bend failure mechanism of zinc coated advanced high strength steel," *ISIJ International*, vol. 58, no. 8, pp. 1538–1544, 2018.

[5] L. Dong, V. Deshpande, and H. Wadley, "Mechanical response of ti–6al–4v octet-truss lattice structures," *International Journal of Solids and Structures*, vol. 60, pp. 107–124, 2015.

[6] X. W. Gu and J. R. Greer, "Ultra-strong architected cu meso-lattices," *Extreme Mechanics Letters*, vol. 2, pp. 7–14, 2015.

[7] S. N. Khaderi, M. Scherer, C. Hall, U. Steiner, U. Ramamurty, N. A. Fleck, and V. S. Deshpande, "The indentation response of nickel nano double gyroid lattices," *Extreme Mechanics Letters*, vol. 10, pp. 15–23, 2017.

[8] J. Bauer, S. Hengsbach, I. Tesari, R. Schwaiger, and O. Kraft, "High-strength cellular ceramic composites with 3d microarchitecture," *Proceedings of the National Academy of Sciences*, vol. 111, no. 7, pp. 2453–2458, 2014.

[9] M. O'Masta, L. Dong, L. St-Pierre, H. Wadley, and V. Deshpande, "The fracture toughness of octet-truss lattices," *Journal of the Mechanics and Physics of Solids*, vol. 98, pp. 271–289,

2017.

[10] A. Benzerga, J. Besson, and A. Pineau, "Anisotropic ductile fracture: Part i: experiments," *Acta Materialia*, vol. 52, no. 15, pp. 4623–4638, 2004.

[11] F. Bron and J. Besson, "Simulation of the ductile tearing for two grades of 2024 aluminum alloy thin sheets," *Engineering Fracture Mechanics*, vol. 73, no. 11, pp. 1531–1552, 2006.

[12] R. M. McMeeking, "Finite deformation analysis of crack-tip opening in elastic-plastic materials and implications for fracture," *Journal of the Mechanics and Physics of Solids*, vol. 25, no. 5, pp. 357–381, 1977.

[13] C. F. Shih, "Relationships between the j-integral and the crack opening displacement for stationary and extending cracks," *Journal of the Mechanics and Physics of Solids*, vol. 29, no. 4, pp. 305–326, 1981.

[14] ASTM:E1820-11, *Standard test method for measurement of fracture toughness*. ASTM International, 2011.

[15] W. J. Joost, "Reducing vehicle weight and improving us energy efficiency using integrated computational materials engineering," *JOM*, vol. 64, no. 9, pp. 1032–1038, 2012.

[16] G. Cole and A. Sherman, "Light weight materials for automotive applications," *Materials characterization*, vol. 35, no. 1, pp. 3–9, 1995.

[17] D. F. Braga, S. Tavares, L. F. da Silva, P. Moreira, and P. M. de Castro, "Advanced design for lightweight structures: Review and prospects," *Progress in Aerospace Sciences*, vol. 69, pp. 29–39, 2014.

[18] H. Liimatainen, P. Stenholm, P. Tapio, and A. McKinnon, "Energy efficiency practices among road freight hauliers," *Energy policy*, vol. 50, pp. 833–842, 2012.

[19] J. R. Davis *et al.*, "Asm specialty handbook," *Aluminum and aluminum alloys*, pp. 207–216, 1993.

[20] N. A. Langerak and S. P. Kragtwijk, "The application of steel and aluminum in a new lightweight car body design," tech. rep., SAE Technical Paper, 1998.

[21] M. M. Avedesian, H. Baker, *et al.*, *ASM specialty handbook: magnesium and magnesium alloys*. ASM international, 1999.

[22] W. Miller, L. Zhuang, J. Bottema, A. Wittebrood, P. De Smet, A. Haszler, and A. Vieregge, "Recent development in aluminium alloys for the automotive industry," *Materials Science and Engineering: A*, vol. 280, no. 1, pp. 37–49, 2000.

[23] R. Kuziak, R. Kawalla, and S. Waengler, "Advanced high strength steels for automotive industry," *Archives of Civil and Mechanical Engineering*, vol. 8, no. 2, pp. 103 – 117, 2008.

[24] T. M. Pollock, "Weight loss with magnesium alloys," *Science*, vol. 328, no. 5981, pp. 986–987, 2010.

[25] G. Davies, *Materials for automobile bodies*. Butterworth-Heinemann, 2012.

[26] A. Devaraj, V. V. Joshi, A. Srivastava, S. Manandhar, V. Moxson, V. A. Duz, and C. Lavender, "A low-cost hierarchical nanostructured beta-titanium alloy with high strength," *Nature communications*, vol. 7, p. 11176, 2016.

[27] D. Bhattacharya, "Metallurgical perspectives on advanced sheet steels for automotive applications," in *Advanced steels*, pp. 163–175, Springer, 2011.

[28] E. Billur and T. Altan, "Challenges in forming advanced high strength steels," *Proceedings of New Developments in Sheet Metal Forming*, pp. 285–304, 2012.

[29] S. Osovski, A. Srivastava, J. C. Williams, and A. Needleman, "Grain boundary crack growth in metastable titanium β alloys," *Acta Materialia*, vol. 82, pp. 167–178, 2015.

[30] E. A. Starke Jr and J. T. Staley, "Application of modern aluminum alloys to aircraft," *Progress in aerospace sciences*, vol. 32, no. 2-3, pp. 131–172, 1996.

[31] F.-K. Chen and T.-B. Huang, "Formability of stamping magnesium-alloy az31 sheets," *Journal of Materials Processing Technology*, vol. 142, no. 3, pp. 643–647, 2003.

[32] G. B. Olson, "Computational design of hierarchically structured materials," *Science*, vol. 277, no. 5330, pp. 1237–1242, 1997.

[33] G. B. Olson, "Designing a new material world," *Science*, vol. 288, no. 5468, pp. 993–998, 2000.

[34] D. L. McDowell, "Simulation-assisted materials design for the concurrent design of materials and products," *JOM*, vol. 59, no. 9, pp. 21–25, 2007.

[35] D. L. McDowell and G. B. Olson, "Concurrent design of hierarchical materials and structures," in *Scientific Modeling and Simulations*, pp. 207–240, Springer, 2008.

[36] D. T. Fullwood, S. R. Niezgoda, B. L. Adams, and S. R. Kalidindi, "Microstructure sensitive design for performance optimization," *Progress in Materials Science*, vol. 55, no. 6, pp. 477–562, 2010.

[37] C. C. Seepersad, R. S. Kumar, J. K. Allen, F. Mistree, and D. L. McDowell, "Multifunctional design of prismatic cellular materials," *Journal of Computer-Aided Materials Design*, vol. 11, no. 2-3, pp. 163–181, 2004.

[38] G. Taguchi, "Introduction to quality engineering: designing quality into products and processes," tech. rep., 1986.

[39] C. A. Coello Coello and R. L. Becerra, "Evolutionary multiobjective optimization in materials science and engineering," *Materials and manufacturing processes*, vol. 24, no. 2, pp. 119–129, 2009.

[40] N. Chakraborti, "Genetic algorithms in materials design and processing," *International Materials Reviews*, vol. 49, no. 3-4, pp. 246–260, 2004.

[41] W. Xu, P. Rivera-Díaz-del Castillo, and S. Van Der Zwaag, "Genetic alloy design based on thermodynamics and kinetics," *Philosophical Magazine*, vol. 88, no. 12, pp. 1825–1833, 2008.

[42] W. Xu, P. Rivera-Díaz-del Castillo, and S. Van der Zwaag, "Designing nanoprecipitation strengthened uhs stainless steels combining genetic algorithms and thermodynamics," *Computational Materials Science*, vol. 44, no. 2, pp. 678–689, 2008.

[43] W. Xu, P. Rivera-Díaz-del Castillo, W. Wang, K. Yang, V. Bliznuk, L. Kestens, and S. Van der Zwaag, "Genetic design and characterization of novel ultra-high-strength stainless steels strengthened by ni3ti intermetallic nanoprecipitates," *Acta Materialia*, vol. 58, no. 10, pp. 3582–3593, 2010.

[44] S. Datta, F. Pettersson, S. Ganguly, H. Saxén, and N. Chakraborti, "Designing high strength multi-phase steel for improved strength–ductility balance using neural networks and multi-objective genetic algorithms," *ISIJ international*, vol. 47, no. 8, pp. 1195–1203, 2007.

[45] S. Ganguly, S. Datta, and N. Chakraborti, "Genetic algorithms in optimization of strength and ductility of low-carbon steels," *Materials and Manufacturing Processes*, vol. 22, no. 5, pp. 650–658, 2007.

[46] T. Fast, M. Knezevic, and S. R. Kalidindi, "Application of microstructure sensitive design to structural components produced from hexagonal polycrystalline metals," *Computational Materials Science*, vol. 43, no. 2, pp. 374–383, 2008.

[47] A. Srivastava, S. Osovski, and A. Needleman, "Engineering the crack path by controlling the microstructure," *Journal of the Mechanics and Physics of Solids*, vol. 100, pp. 1–20, 2017.

[48] D. Gerbig, A. Srivastava, S. Osovski, L. G. Hector, and A. Bower, "Analysis and design of dual-phase steel microstructure for enhanced ductile fracture resistance," *International Journal of Fracture*, vol. 209, no. 1-2, pp. 3–26, 2018.

[49] S. Osovski, A. Needleman, and A. Srivastava, "Intergranular fracture prediction and microstructure design," *International Journal of Fracture*, vol. 216, no. 2, pp. 135–148, 2019.

[50] A. Molkeri, A. Srivastava, S. Osovski, and A. Needleman, "Influence of grain size distribution on ductile intergranular crack growth resistance," *Journal of Applied Mechanics*, pp. 1–11, 2019.

[51] S. Hao, B. Moran, W. K. Liu, and G. B. Olson, "A hierarchical multi-physics model for design of high toughness steels," *Journal of Computer-Aided Materials Design*, vol. 10, no. 2, pp. 99–142, 2003.

[52] S. Hao, W. K. Liu, B. Moran, F. Vernerey, and G. B. Olson, "Multi-scale constitutive model and computational framework for the design of ultra-high strength, high toughness steels," *Computer Methods in Applied Mechanics and Engineering*, vol. 193, no. 17-20, pp. 1865–1908, 2004.

[53] A. Pineau, A. A. Benzerga, and T. Pardoen, "Failure of metals i: Brittle and ductile fracture," *Acta Materialia*, vol. 107, pp. 424–483, 2016.

[54] P. Kanouté, D. Boso, J. Chaboche, and B. Schrefler, "Multiscale methods for composites: a review," *Archives of Computational Methods in Engineering*, vol. 16, no. 1, pp. 31–75, 2009.

[55] M. G. Geers, V. G. Kouznetsova, and W. Brekelmans, "Multi-scale computational homogenization: Trends and challenges," *Journal of computational and applied mathematics*, vol. 234, no. 7, pp. 2175–2182, 2010.

[56] C. Caceres and J. Griffiths, "Damage by the cracking of silicon particles in an al-7si-0.4 mg casting alloy," *Acta materialia*, vol. 44, no. 1, pp. 25–33, 1996.

[57] G. Guiglionda and W. Poole, "The role of damage on the deformation and fracture of al–si eutectic alloys," *Materials Science and Engineering: A*, vol. 336, no. 1-2, pp. 159–169, 2002.

[58] M. Gagne and E. Thibault, "Behaviour of inclusions during rolling of continuously cast billets," *CIM bulletin*, vol. 91, no. 1021, pp. 98–103, 1998.

[59] S. Hosseini, C. Temmel, B. Karlsson, and N.-G. Ingesten, "An in-situ scanning electron microscopy study of the bonding between mns inclusions and the matrix during tensile deformation of hot-rolled steels," *Metallurgical and Materials Transactions A*, vol. 38, no. 5, pp. 982–989, 2007.

[60] M. Shabrov, C. Briant, A. Needleman, S. Kim, E. Sylven, D. Sherman, and L. Chuzhoy, "Void nucleation by inclusion cracking," *Metallurgical and Materials Transactions A*, vol. 35, no. 6, pp. 1745–1755, 2004.

[61] Y. Bao and T. Wierzbicki, "On fracture locus in the equivalent strain and stress triaxiality space," *International Journal of Mechanical Sciences*, vol. 46, no. 1, pp. 81–98, 2004.

[62] M. Luo and T. Wierzbicki, "Numerical failure analysis of a stretch-bending test on dual-phase steel sheets using a phenomenological fracture model," *International Journal of Solids and Structures*, vol. 47, no. 22-23, pp. 3084–3102, 2010.

[63] C. C. Roth and D. Mohr, "Effect of strain rate on ductile fracture initiation in advanced high strength steel sheets: Experiments and modeling," *International Journal of Plasticity*, vol. 56, pp. 19–44, 2014.

[64] S. J. Marcadet and D. Mohr, "Effect of compression–tension loading reversal on the strain to fracture of dual phase steel sheets," *International Journal of Plasticity*, vol. 72, pp. 21–43, 2015.

[65] F. Andrade, M. Feucht, A. Haufe, and F. Neukamm, "An incremental stress state dependent damage model for ductile failure prediction," *International Journal of Fracture*, vol. 200, no. 1-2, pp. 127–150, 2016.

[66] X. Sun, K. S. Choi, W. N. Liu, and M. A. Khaleel, "Predicting failure modes and ductility of dual phase steels using plastic strain localization," *International Journal of Plasticity*, vol. 25, no. 10, pp. 1888–1909, 2009.

[67] X. Sun, K. S. Choi, A. Soulami, W. N. Liu, and M. A. Khaleel, "On key factors influencing ductile fractures of dual phase (dp) steels," *Materials Science and Engineering: A*, vol. 526, no. 1-2, pp. 140–149, 2009.

[68] K. S. Choi, W. N. Liu, X. Sun, and M. A. Khaleel, "Influence of martensite mechanical properties on failure mode and ductility of dual-phase steels," *Metallurgical and Materials Transactions A*, vol. 40, no. 4, pp. 796–809, 2009.

[69] V. Uthaisangsuk, U. Prahl, and W. Bleck, "Failure modeling of multiphase steels using representative volume elements based on real microstructures," *Procedia Engineering*, vol. 1, no. 1, pp. 171–176, 2009.

[70] V. Uthaisangsuk, U. Prahl, and W. Bleck, "Modelling of damage and failure in multiphase high strength dp and trip steels," *Engineering Fracture Mechanics*, vol. 78, no. 3, pp. 469–486, 2011.

[71] J. Kadkhodapour, A. Butz, S. Ziaei-Rad, and S. Schmauder, "A micro mechanical study on failure initiation of dual phase steels under tension using single crystal plasticity model," *International Journal of Plasticity*, vol. 27, no. 7, pp. 1103–1125, 2011.

[72] S. K. Paul, "Micromechanics based modeling of dual phase steels: Prediction of ductility and failure modes," *Computational Materials Science*, vol. 56, pp. 34–42, 2012.

[73] N. Vajragupta, V. Uthaisangsuk, B. Schmaling, S. Münstermann, A. Hartmaier, and W. Bleck, "A micromechanical damage simulation of dual phase steels using xfem," *Computational Materials Science*, vol. 54, pp. 271–279, 2012.

[74] K. Perzyński, Ł. Madej, J. Wang, R. Kuziak, and P. D. Hodgson, "Numerical investigation of influence of the martensite volume fraction on dp steels fracture behavior on the basis of digital material representation model," *Metallurgical and materials transactions A*, vol. 45, no. 13, pp. 5852–5865, 2014.

[75] T. Matsuno, C. Teodosiu, D. Maeda, and A. Uenishi, "Mesoscale simulation of the early evolution of ductile fracture in dual-phase steels," *International Journal of Plasticity*, vol. 74, pp. 17–34, 2015.

[76] T. De Geus, R. Peerlings, and M. Geers, "Microstructural topology effects on the onset of ductile failure in multi-phase materials–a systematic computational approach," *International Journal of Solids and Structures*, vol. 67, pp. 326–339, 2015.

[77] T. De Geus, J. van Duuren, R. Peerlings, and M. Geers, "Fracture initiation in multi-phase materials: A statistical characterization of microstructural damage sites," *Materials Science and Engineering: A*, vol. 673, pp. 551–556, 2016.

[78] T. De Geus, R. Peerlings, and M. Geers, "Fracture in multi-phase materials: Why some microstructures are more critical than others," *Engineering Fracture Mechanics*, vol. 169, pp. 354–370, 2017.

[79] M. Ayatollahi, A. C. Darabi, H. Chamani, and J. Kadkhodapour, "3d micromechanical modeling of failure and damage evolution in dual phase steel based on a real 2d microstructure," *Acta Mechanica Solida Sinica*, vol. 29, no. 1, pp. 95–110, 2016.

[80] G. Avramovic-Cingara, Y. Ososkov, M. Jain, and D. Wilkinson, "Effect of martensite distribution on damage behaviour in dp600 dual phase steels," *Materials Science and Engineering: A*, vol. 516, no. 1-2, pp. 7–16, 2009.

[81] F. A. McClintock, "A criterion for ductile fracture by the growth of holes," 1968.

[82] J. R. Rice and D. M. Tracey, "On the ductile enlargement of voids in triaxial stress fields," *Journal of the Mechanics and Physics of Solids*, vol. 17, no. 3, pp. 201–217, 1969.

[83] A. L. Gurson, "Plastic flow and fracture behavior of ductile materials incorporating void nucleation, growth and coalescence," *PhD Diss, Brown University*, 1975.

[84] V. Tvergaard and A. Needleman, "Analysis of the cup-cone fracture in a round tensile bar," *Acta metallurgica*, vol. 32, no. 1, pp. 157–169, 1984.

[85] M. Gologanu, J.-B. Leblond, and J. Devaux, "Approximate models for ductile metals containing non-spherical voids-case of axisymmetric prolate ellipsoidal cavities," *Journal of the Mechanics and Physics of Solids*, vol. 41, no. 11, pp. 1723–1754, 1993.

[86] M. Gologanu, J.-B. Leblond, and J. Devaux, "Approximate models for ductile metals containing nonspherical voids-case of axisymmetric oblate ellipsoidal cavities," 1994.

[87] C. Chu and A. Needleman, "Void nucleation effects in biaxially stretched sheets," *Journal of engineering materials and technology*, vol. 102, no. 3, pp. 249–256, 1980.

[88] V. Tvergaard, "Influence of voids on shear band instabilities under plane strain conditions," *International Journal of fracture*, vol. 17, no. 4, pp. 389–407, 1981.

[89] V. Tvergaard, "On localization in ductile materials containing spherical voids," *International Journal of fracture*, vol. 18, no. 4, pp. 237–252, 1982.

[90] V. Tvergaard, "Influence of void nucleation on ductile shear fracture at a free surface," *Journal of the Mechanics and Physics of Solids*, vol. 30, no. 6, pp. 399–425, 1982.

[91] S. Osovski, A. Srivastava, L. Ponson, E. Bouchaud, V. Tvergaard, K. Ravi-Chandar, and A. Needleman, "The effect of loading rate on ductile fracture toughness and fracture surface roughness," *Journal of the Mechanics and Physics of Solids*, vol. 76, pp. 20–46, 2015.

[92] J. Pan, M. Saje, and A. Needleman, "Localization of deformation in rate sensitive porous plastic solids," *International Journal of Fracture*, vol. 21, no. 4, pp. 261–278, 1983.

[93] T. Belytschko, R. L. Chiapetta, and H. D. Bartel, "Efficient large scale non-linear transient analysis by finite elements," *International Journal for Numerical Methods in Engineering*, vol. 10, no. 3, pp. 579–596, 1976.

[94] D. Peirce, C. F. Shih, and A. Needleman, "A tangent modulus method for rate dependent solids," *Computers & Structures*, vol. 18, no. 5, pp. 875–887, 1984.

[95] C. F. Tipper, "The fracture of metals," *Metallurgia*, vol. 39, no. 231, pp. 133–137, 1949.

[96] S. H. Goods and L. M. Brown, "Overview no. 1: The nucleation of cavities by plastic deformation," *Acta metallurgica*, vol. 27, no. 1, pp. 1–15, 1979.

[97] V. Tvergaard, "Material failure by void growth to coalescence," in *Advances in applied Mechanics*, vol. 27, pp. 83–151, Elsevier, 1989.

[98] A. A. Benzerga and J.-B. Leblond, "Ductile fracture by void growth to coalescence," in *Advances in applied mechanics*, vol. 44, pp. 169–305, Elsevier, 2010.

[99] A. A. Benzerga, J.-B. Leblond, A. Needleman, and V. Tvergaard, "Ductile failure modeling," *International Journal of Fracture*, vol. 201, no. 1, pp. 29–80, 2016.

[100] J. W. Martin, *Precipitation hardening: theory and applications*. Butterworth-Heinemann, 2012.

[101] J.-P. Birat, "Steel cleanliness and environmental metallurgy," *Metallurgical Research & Technology*, vol. 113, no. 2, p. 201, 2016.

[102] J. R. Rice and M. A. Johnson, "The role of large crack tip geometry changes in plane strain fracture," in *Inelastic behaviour of solids*, pp. 641–672, McGraw-Hill, 1970.

[103] J. R. Rice, "The localization of plastic deformation," in *In: Koiter W (ed) 14th International congress theoretical and applied mechanics*, pp. 207–220, North-Holland, 1976.

[104] N. Aravas and R. M. McMeeking, "Finite element analysis of void growth near a blunting crack tip," *Journal of the Mechanics and Physics of Solids*, vol. 33, no. 1, pp. 25–49, 1985.

[105] A. Needleman and V. Tvergaard, "An analysis of ductile rupture modes at a crack tip," *Journal of the Mechanics and Physics of Solids*, vol. 35, no. 2, pp. 151–183, 1987.

[106] X. Gao, J. Faleskog, C. F. Shih, and R. H. Dodds Jr, "Ductile tearing in part-through cracks: experiments and cell-model predictions," *Engineering fracture mechanics*, vol. 59, no. 6, pp. 761–777, 1998.

[107] S. Tang, A. M. Kopacz, S. Chan, G. B. Olson, W. K. Liu, *et al.*, "Three-dimensional ductile fracture analysis with a hybrid multiresolution approach and microtomography," *Journal of the Mechanics and Physics of Solids*, vol. 61, no. 11, pp. 2108–2124, 2013.

[108] B. I. Edelson and W. M. Baldwin Jr, "The effect of second phases on the mechanical properties of alloys," tech. rep., DTIC Document, 1959.

[109] J. M. Krafft, "Correlation of plane strain crack toughness with strain hardening characteristics of a low, a medium, and a high strength steel," *Applied Materials Research*, vol. 3, no. 2, pp. 83–96, 1964.

[110] A. J. Birkle, R. P. Wei, and G. E. Pellissier, "Analysis of plane-strain fracture in a series of 0. 45 c-ni-cr-mo steels with different sulfur contents," *ASM Trans Quart*, vol. 59, no. 4, pp. 981–990, 1966.

[111] W. Spitzig, "Correlations between fractographic features and plane-strain fracture toughness in an ultrahigh-strength steel," in *Electron Microfractography*, ASTM International, 1969.

[112] G. T. Hahn, M. F. Kanninen, and A. R. Rosenfield, "Fracture toughness of materials," *Annual Review of Materials Science*, vol. 2, no. 1, pp. 381–404, 1972.

[113] D. E. Passoja and D. C. Hill, "On the distribution of energy in the ductile fracture of high strength steels," *Metallurgical Transactions*, vol. 5, no. 8, pp. 1851–1854, 1974.

[114] G. Green and J. F. Knott, "The initiation and propagation of ductile fracture in low strength steels," *Journal of Engineering Materials and Technology*, vol. 98, no. 1, pp. 37–46, 1976.

[115] J. C. Lautridou and A. Pineau, "Crack initiation and stable crack growth resistance in a508 steels in relation to inclusion distribution," *Engineering Fracture Mechanics*, vol. 15, no. 1-2, pp. 55–71, 1981.

[116] W. M. Garrison and N. R. Moody, "The influence of inclusion spacing and microstructure on the fracture toughness of the secondary hardening steel af1410," *Metallurgical Transactions A*, vol. 18, no. 7, pp. 1257–1263, 1987.

[117] E. M. Dubensky and D. A. Koss, "Void/pore distributions and ductile fracture," *Metallurgical Transactions A*, vol. 18, no. 11, pp. 1887–1895, 1987.

[118] R. Becker, "The effect of porosity distribution on ductile failure," *Journal of the Mechanics and Physics of Solids*, vol. 35, no. 5, pp. 577–599, 1987.

[119] W. M. Garrison, A. L. Wojcieszynski, and L. E. Iorio, "Effects of inclusion distributions on the fracture toughness of structural steels," *Recent advances in Fracture*, pp. 361–372, 1997.

[120] A. A. Benzerga, J. Besson, and A. Pineau, "Coalescence-controlled anisotropic ductile fracture," *Journal of Engineering Materials and Technology*, vol. 121, no. 2, pp. 221–229, 1999.

[121] L. Jie, G. Feng, L. Zhi, J.-L. Wang, and M.-G. Yan, "Influence of sizes of inclusions and voids on fracture toughness of ultra-high strength steel aermet100," *Journal of Iron and Steel Research, International*, vol. 14, no. 5, pp. 254–258, 2007.

[122] W. M. Garrison Jr and A. L. Wojcieszynski, "A discussion of the spacing of inclusions in the volume and of the spacing of inclusion nucleated voids on fracture surfaces of steels," *Materials Science and Engineering: A*, vol. 505, no. 1-2, pp. 52–61, 2009.

[123] G. T. Hahn and A. R. Rosenfield, "Metallurgical factors affecting fracture toughness of aluminum alloys," *Metallurgical Transactions A*, vol. 6, no. 4, pp. 653–668, 1975.

[124] E. Amar and A. Pineau, "Interpretation of ductile fracture toughness temperature dependence of a low strength steel in terms of a local approach," *Engineering Fracture Mechanics*, vol. 22, no. 6, pp. 1061–1071, 1985.

[125] R. H. Van Stone and J. A. Psioda, "Discussion of "metallurgical factors affecting fracture toughness of aluminum alloys"," *Metallurgical Transactions A*, vol. 6, pp. 668–670, 1975.

[126] M. N. Shabrov and A. Needleman, "An analysis of inclusion morphology effects on void nucleation," *Modelling and Simulation in Materials Science and Engineering*, vol. 10, no. 2, p. 163, 2002.

[127] V. Tvergaard and J. W. Hutchinson, "Two mechanisms of ductile fracture: void by void growth versus multiple void interaction," *International Journal of Solids and Structures*, vol. 39, no. 13-14, pp. 3581–3597, 2002.

[128] J. Kim, X. Gao, and T. S. Srivatsan, "Modeling of crack growth in ductile solids: a three-dimensional analysis," *International journal of solids and structures*, vol. 40, no. 26, pp. 7357–7374, 2003.

[129] T. Pardoen and J. W. Hutchinson, "Micromechanics-based model for trends in toughness of ductile metals," *Acta Materialia*, vol. 51, no. 1, pp. 133–148, 2003.

[130] X. Gao, T. Wang, and J. Kim, "On ductile fracture initiation toughness: effects of void volume fraction, void shape and void distribution," *International Journal of Solids and Structures*, vol. 42, no. 18-19, pp. 5097–5117, 2005.

[131] J. Kim, G. Zhang, and X. Gao, "Modeling of ductile fracture: application of the mechanism-based concepts," *International journal of solids and structures*, vol. 44, no. 6, pp. 1844–1862, 2007.

[132] V. Tvergaard, "Discrete modelling of ductile crack growth by void growth to coalescence," *International Journal of Fracture*, vol. 148, no. 1, pp. 1–12, 2007.

[133] C. Tekoğlu, J. W. Hutchinson, and T. Pardoen, "On localization and void coalescence as a precursor to ductile fracture," *Phil. Trans. R. Soc. A*, vol. 373, no. 2038, p. 20140121, 2015.

[134] K. E. Puttick, "Ductile fracture in metals," *Philosophical magazine*, vol. 4, no. 44, pp. 964–969, 1959.

[135] H. C. Rogers, "The tensile fracture of ductile metals," *Trans Metal. Soc. AIME*, vol. 218, pp. 498–506, 1960.

[136] J. Gurland and J. Plateau, "The mechanism of ductile rupture of metals containing particles," *Trans. ASM*, vol. 56, pp. 442–454, 1963.

[137] H. Tinet, H. Klöcker, and J. Le Coze, "Damage analysis during hot deformation of a resulfurised stainless steel," *Acta materialia*, vol. 52, no. 13, pp. 3825–3842, 2004.

[138] J. R. Rice, "A path independent integral and the approximate analysis of strain concentration by notches and cracks," *Journal of applied mechanics*, vol. 35, no. 2, pp. 379–386, 1968.

[139] N. Aravas and R. M. McMeeking, "Microvoid growth and failure in the ligament between a hole and a blunt crack tip," *International Journal of Fracture*, vol. 29, no. 1, pp. 21–38, 1985.

[140] C. L. Hom and R. M. McMeeking, "Three-dimensional void growth before a blunting crack tip," *Journal of the Mechanics and Physics of Solids*, vol. 37, no. 3, pp. 395–415, 1989.

[141] T. B. Cox and J. R. Low, "An investigation of the plastic fracture of aisi 4340 and 18 nickel-200 grade maraging steels," *Metallurgical Transactions*, vol. 5, no. 6, pp. 1457–1470, 1974.

[142] A. Ghahremaninezhad and K. Ravi-Chandar, "Deformation and failure in nodular cast iron," *Acta Materialia*, vol. 60, no. 5, pp. 2359–2368, 2012.

[143] A. Ghahremaninezhad and K. Ravi-Chandar, "Ductile failure behavior of polycrystalline al 6061-t6," *International journal of fracture*, vol. 174, no. 2, pp. 177–202, 2012.

[144] R. H. V. Stone, T. B. Cox, J. R. Low, and J. A. Psioda, "Microstructural aspects of fracture by dimpled rupture," *International Metals Reviews*, vol. 30, no. 1, pp. 157–180, 1985.

[145] R. J. Bourcier, D. A. Koss, R. E. Smelser, and O. Richmond, "The influence of porosity on the deformation and fracture of alloys," *Acta Metallurgica*, vol. 34, no. 12, pp. 2443–2453, 1986.

[146] K. Gall, M. Horstemeyer, D. L. McDowell, and J. Fan, "Finite element analysis of the stress distributions near damaged si particle clusters in cast al–si alloys," *Mechanics of Materials*, vol. 32, no. 5, pp. 277–301, 2000.

[147] F. Hannard, A. Simar, E. Maire, and T. Pardoen, "Quantitative assessment of the impact of second phase particle arrangement on damage and fracture anisotropy," *Acta Materialia*, vol. 148, pp. 456–466, 2018.

[148] M. S. Rashid, "Dual phase steels," *Annual Review of Materials Science*, vol. 11, no. 1, pp. 245–266, 1981.

[149] R. Davies, "Influence of martensite composition and content on the properties of dual phase steels," *Metallurgical Transactions A*, vol. 9, no. 5, pp. 671–679, 1978.

[150] L. F. Ramos, D. K. Matlock, and G. Krauss, "On the deformation behavior of dual-phase steels," *Metallurgical and Materials Transactions A*, vol. 10, no. 2, pp. 259–261, 1979.

[151] D. L. Steinbrunner, D. Matlock, and G. Krauss, "Void formation during tensile testing of dual phase steels," *Metallurgical Transactions A*, vol. 19, no. 3, pp. 579–589, 1988.

[152] S.-H. Choi, E.-Y. Kim, W. Woo, S. Han, and J. Kwak, "The effect of crystallographic orientation on the micromechanical deformation and failure behaviors of dp980 steel during uniaxial tension," *International Journal of Plasticity*, vol. 45, pp. 85–102, 2013.

[153] G. Avramovic-Cingara, C. A. Saleh, M. Jain, and D. Wilkinson, "Void nucleation and growth in dual-phase steel 600 during uniaxial tensile testing," *Metallurgical and materials transactions A*, vol. 40, no. 13, p. 3117, 2009.

[154] S. Sodjit and V. Uthaisangsuk, "Microstructure based prediction of strain hardening behavior of dual phase steels," *Materials & Design*, vol. 41, pp. 370–379, 2012.

[155] S. Yerra, G. Martin, M. Veron, Y. Brechet, J. Mithieux, L. Delannay, and T. Pardoen, "Ductile fracture initiated by interface nucleation in two-phase elastoplastic systems," *Engineering Fracture Mechanics*, vol. 102, pp. 77–100, 2013.

[156] C. C. Tasan, J. P. Hoefnagels, M. Diehl, D. Yan, F. Roters, and D. Raabe, "Strain localization and damage in dual phase steels investigated by coupled in-situ deformation experiments and crystal plasticity simulations," *International Journal of Plasticity*, vol. 63, pp. 198–210, 2014.

[157] C. C. Tasan, M. Diehl, D. Yan, M. Bechtold, F. Roters, L. Schemmann, C. Zheng, N. Peranio, D. Ponge, M. Koyama, *et al.*, "An overview of dual-phase steels: advances in microstructure-oriented processing and micromechanically guided design," *Annual Review of Materials Research*, vol. 45, pp. 391–431, 2015.

[158] Q. Lai, O. Bouaziz, M. Gouné, L. Brassart, M. Verdier, G. Parry, A. Perlade, Y. Bréchet, and T. Pardoen, "Damage and fracture of dual-phase steels: Influence of martensite volume fraction," *Materials Science and Engineering: A*, vol. 646, pp. 322–331, 2015.

[159] A. Alaie, J. Kadkhodapour, S. Z. Rad, M. A. Asadabad, and S. Schmauder, "Formation and coalescence of strain localized regions in ferrite phase of dp600 steels under uniaxial tensile deformation," *Materials Science and Engineering: A*, vol. 623, pp. 133–144, 2015.

[160] J. Zhou, A. M. Gokhale, A. Gurumurthy, and S. P. Bhat, "Realistic microstructural rve-based simulations of stress–strain behavior of a dual-phase steel having high martensite volume fraction," *Materials Science and Engineering: A*, vol. 630, pp. 107–115, 2015.

[161] Q. Lai, L. Brassart, O. Bouaziz, M. Gouné, M. Verdier, G. Parry, A. Perlade, Y. Bréchet, and T. Pardoen, "Influence of martensite volume fraction and hardness on the plastic behavior of dual-phase steels: Experiments and micromechanical modeling," *International Journal of Plasticity*, vol. 80, pp. 187–203, 2016.

[162] J. D. Embury and J. L. Duncan, "Formability of dual-phase steels," *JOM*, vol. 34, pp. 24–29, Mar 1982.

[163] K. Hasegawa, K. Kawamura, T. Urabe, and Y. Hosoya, "Effects of microstructure on stretch-flange-formability of 980 mpa grade cold-rolled ultra high strength steel sheets," *ISIJ international*, vol. 44, no. 3, pp. 603–609, 2004.

[164] V. Uthaisangsuk, U. Prahl, and W. Bleck, "Characterisation of formability behaviour of multiphase steels by micromechanical modelling," *International Journal of Fracture*, vol. 157, no. 1-2, p. 55, 2009.

[165] A. Srivastava, A. Bower, L. Hector Jr, J. Carsley, L. Zhang, and F. Abu-Farha, "A multi-scale approach to modeling formability of dual-phase steels," *Modelling and Simulation in Materials Science and Engineering*, vol. 24, no. 2, p. 025011, 2016.

[166] S. Huang, C. He, and Y. Zhao, "Microstructure-based rve approach for stretch-bending of dual-phase steels," *Journal of Materials Engineering and Performance*, vol. 25, no. 3, pp. 966–976, 2016.

[167] S. Sriram, C. Wong, M. Huang, and B. Yan, "Stretch bendability of advanced high strength steels," tech. rep., SAE Technical Paper, 2003.

[168] K. E. N'souglo, A. Srivastava, S. Osovski, and J. A. Rodríguez-Martínez, "Random distributions of initial porosity trigger regular necking patterns at high strain rates," *Proceedings of the Royal Society A: Mathematical, Physical and Engineering Sciences*, vol. 474, no. 2211, p. 20170575, 2018.

[169] MATLAB, *Image Processing Toolbox*. The MathWorks Inc., Natick, MA, USA, R2017b.

[170] S. F. Ghoreishi, A. Molkeri, A. Srivastava, R. Arroyave, and D. Allaire, "Multi-information source fusion and optimization to realize icme: Application to dual-phase materials," *Journal of Mechanical Design*, vol. 140, no. 11, p. 111409, 2018.

[171] A. Srivastava, H. Ghassemi-Armaki, H. Sung, P. Chen, S. Kumar, and A. F. Bower, "Micromechanics of plastic deformation and phase transformation in a three-phase trip-assisted advanced high strength steel: Experiments and modeling," *Journal of the Mechanics and Physics of Solids*, vol. 78, pp. 46–69, 2015.

[172] A. Needleman, "Material rate dependence and mesh sensitivity in localization problems," *Computer methods in applied mechanics and engineering*, vol. 67, no. 1, pp. 69–85, 1988.

[173] P. Thornton, "The influence of nonmetallic inclusions on the mechanical properties of steel: A review," *Journal of Materials Science*, vol. 6, no. 4, pp. 347–356, 1971.

[174] Q. Han, Y. Kang, P. D. Hodgson, and N. Stanford, "Quantitative measurement of strain partitioning and slip systems in a dual-phase steel," *Scripta Materialia*, vol. 69, no. 1, pp. 13–16, 2013.

[175] X. Zheng, H. Ghassemi-Armaki, and A. Srivastava, "Structural and microstructural influence on deformation and fracture of dual-phase steels," *Materials Science and Engineering: A*, p. 138924, 2020.

[176] J. Kadkhodapour, A. Butz, and S. Z. Rad, "Mechanisms of void formation during tensile testing in a commercial, dual-phase steel," *Acta Materialia*, vol. 59, no. 7, pp. 2575–2588, 2011.

[177] J. Samei, L. Zhou, J. Kang, and D. S. Wilkinson, "Microstructural analysis of ductility and fracture in fine-grained and ultrafine-grained vanadium-added dp1300 steels," *International Journal of Plasticity*, vol. 117, pp. 58–70, 2019.

[178] R. J. Freund, W. J. Wilson, and P. Sa, *Regression analysis*. Elsevier, 2006.

[179] J. Carrete, W. Li, N. Mingo, S. Wang, and S. Curtarolo, "Finding unprecedentedly low-thermal-conductivity half-heusler semiconductors via high-throughput materials modeling," *Physical Review X*, vol. 4, no. 1, p. 011019, 2014.

[180] A. Vinci, L. Zoli, D. Sciti, C. Melandri, and S. Guicciardi, "Understanding the mechanical properties of novel uhtcmcs through random forest and regression tree analysis," *Materials & Design*, vol. 145, pp. 97–107, 2018.

[181] J. Zhang, G. Ma, Y. Huang, F. Aslani, B. Nener, *et al.*, "Modelling uniaxial compressive strength of lightweight self-compacting concrete using random forest regression," *Construction and Building Materials*, vol. 210, pp. 713–719, 2019.

[182] Y. Wang, Y. Tian, T. Kirk, O. Laris, J. H. Ross Jr, R. D. Noebe, V. Keylin, and R. Arróyave, "Accelerated design of fe-based soft magnetic materials using machine learning and stochastic optimization," *Acta Materialia*, 2020.

[183] J. H. Friedman, "Greedy function approximation: a gradient boosting machine," *Annals of statistics*, pp. 1189–1232, 2001.

[184] M. F. Ashby, "Materials selection in mechanical design," *MRS Bull*, vol. 30, no. 12, p. 995, 2005.

[185] N. Fleck, V. Deshpande, and M. Ashby, "Micro-architectured materials: past, present and future," *Proceedings of the Royal Society A: Mathematical, Physical and Engineering Sciences*, vol. 466, no. 2121, pp. 2495–2516, 2010.

[186] M. Ashby, "Hybrid materials to expand the boundaries of material-property space," *Journal of the American Ceramic Society*, vol. 94, pp. s3–s14, 2011.

[187] S. Khaderi, V. Deshpande, and N. Fleck, "The stiffness and strength of the gyroid lattice," *International Journal of Solids and Structures*, vol. 51, no. 23-24, pp. 3866–3877, 2014.

[188] S. Maiti, M. Ashby, and L. Gibson, "Fracture toughness of brittle cellular solids," *Scripta Metallurgica*, vol. 18, no. 3, pp. 213–217, 1984.

[189] J. Huang and L. Gibson, "Fracture toughness of brittle honeycombs," *Acta metallurgica et materialia*, vol. 39, no. 7, pp. 1617–1626, 1991.

[190] J. Huang and L. Gibson, "Fracture toughness of brittle foams," *Acta metallurgica et materialia*, vol. 39, no. 7, pp. 1627–1636, 1991.

[191] L. J. Gibson and M. F. Ashby, *Cellular solids: structure and properties*. Cambridge university press, 1999.

[192] N. A. Fleck and X. Qiu, "The damage tolerance of elastic–brittle, two-dimensional isotropic lattices," *Journal of the Mechanics and Physics of Solids*, vol. 55, no. 3, pp. 562–588, 2007.

[193] N. E. Romijn and N. A. Fleck, "The fracture toughness of planar lattices: imperfection sensitivity," *Journal of the Mechanics and Physics of Solids*, vol. 55, no. 12, pp. 2538–2564, 2007.

[194] I. Quintana-Alonso, S. Mai, N. Fleck, D. Oakes, and M. Twigg, "The fracture toughness of a cordierite square lattice," *Acta Materialia*, vol. 58, no. 1, pp. 201–207, 2010.

[195] I. Schmidt and N. Fleck, "Ductile fracture of two-dimensional cellular structures – dedicated to prof. dr.-ing. d. gross on the occasion of his 60th birthday," *International Journal of Fracture*, vol. 111, pp. 327–342, Oct 2001.

[196] J. Begley, W. Logsdon, and J. Landes, "Ductile rupture blunt-notch fracture criterion," in *Flaw Growth and Fracture*, ASTM International, 1977.

[197] M. Yoda, "The effect of the notch root radius on the j-integral fracture toughness under modes i, ii and iii loadings," *Engineering fracture mechanics*, vol. 26, no. 3, pp. 425–431, 1987.

[198] T. L. Anderson, *Fracture mechanics: fundamentals and applications*. CRC press, 2017.

[199] K. Y. McCullough, N. A. Fleck, and M. F. Ashby, "Toughness of aluminium alloy foams," *Acta materialia*, vol. 47, no. 8, pp. 2331–2343, 1999.

[200] O. Olurin, N. A. Fleck, and M. F. Ashby, "Deformation and fracture of aluminium foams," *Materials Science and Engineering: A*, vol. 291, no. 1-2, pp. 136–146, 2000.

[201] J. Faleskog, X. Gao, and C. F. Shih, "Cell model for nonlinear fracture analysis–i. micromechanics calibration," *International Journal of Fracture*, vol. 89, no. 4, pp. 355–373, 1998.

[202] S. Hosseini and S. Hadidi-Moud, "Application of the gtn model in ductile fracture prediction of 7075-t651 aluminum alloy," *Journal of Solid Mechanics*, vol. 8, no. 2, pp. 326–333, 2016.

[203] D. Gerbig, A. Srivastava, S. Osovski, L. G. Hector, and A. Bower, "Analysis and design of dual-phase steel microstructure for enhanced ductile fracture resistance," *International Journal of Fracture*, pp. 1–24, 2017.

[204] F. Z. Li, C. F. Shih, and A. Needleman, "A comparison of methods for calculating energy release rates," *Engineering Fracture Mechanics*, vol. 21, no. 2, pp. 405–421, 1985.

[205] D. Carka and C. M. Landis, "On the path-dependence of the j-integral near a stationary crack in an elastic-plastic material," *Journal of Applied Mechanics*, vol. 78, no. 1, p. 011006, 2011.

[206] H. Tankasala, T. Li, P. Seiler, V. Deshpande, and N. Fleck, "An assessment of the j-integral test for a metallic foam," *Journal of the Mechanics and Physics of Solids*, p. 103958, 2020.

[207] X.-K. Zhu, "Advances in fracture toughness test methods for ductile materials in low-constraint conditions," *Procedia Engineering*, vol. 130, pp. 784–802, 2015.

[208] D. M. Turner and S. R. Kalidindi, "Statistical construction of 3-d microstructures from 2-d exemplars collected on oblique sections," *Acta Materialia*, vol. 102, pp. 136–148, 2016.

[209] K. Yamazaki, M. Oka, H. Yasuda, Y. Mizuyama, and H. Tsuchiya, "Recent advances in ultrahigh-strength sheet steels for automotive structural use," *Nippon Steel technical report*, 1995.

[210] K.-i. Sugimoto, B. Yu, Y.-i. Mukai, and S. Ikeda, "Microstructure and formability of aluminum bearing trip-aided steels with annealed martensite matrix," *ISIJ international*, vol. 45, no. 8, pp. 1194–1200, 2005.

[211] D. Reche, T. Sturel, O. Bouaziz, A. Col, and A.-F. Gourgues-Lorenzon, "Damage development in low alloy trip-aided steels during air-bending," *Materials Science and Engineering: A*, vol. 528, no. 15, pp. 5241–5250, 2011.

[212] L. Shi, Z. Yan, Y. Liu, C. Zhang, Z. Qiao, B. Ning, and H. Li, "Improved toughness and ductility in ferrite/acicular ferrite dual-phase steel through intercritical heat treatment," *Materials Science and Engineering: A*, vol. 590, pp. 7–15, 2014.

[213] C. Suppan, T. Hebesberger, A. Pichler, J. Rehrl, and O. Kolednik, "On the microstructure control of the bendability of advanced high strength steels," *Materials Science and Engineering: A*, vol. 735, pp. 89–98, 2018.

[214] S. Nasiri, M. R. Khosravani, and K. Weinberg, "Fracture mechanics and mechanical fault detection by artificial intelligence methods: A review," *Engineering Failure Analysis*, vol. 81, pp. 270–293, 2017.

[215] N. Lubbers, T. Lookman, and K. Barros, "Inferring low-dimensional microstructure representations using convolutional neural networks," *Physical Review E*, vol. 96, no. 5, p. 052111, 2017.

[216] A. Rovinelli, M. D. Sangid, H. Proudhon, and W. Ludwig, "Using machine learning and a data-driven approach to identify the small fatigue crack driving force in polycrystalline materials," *npj Computational Materials*, vol. 4, no. 1, pp. 1–10, 2018.

[217] K. Pierson, A. Rahman, and A. D. Spear, "Predicting microstructure-sensitive fatigue-crack path in 3d using a machine learning framework," *JOM*, vol. 71, no. 8, pp. 2680–2694, 2019.